

**COMPUTER-AIDED DIAGNOSIS AND GRADING SYSTEM OF
DIABETIC RETINOPATHY BASED ON COTTON WOOL SPOT
DETECTION**

SYNA SRENG

**A THESIS SUBMITTED IN PARTIAL FULFILLMENT
OF THE REQUIREMENTS FOR THE DEGREE OF
DOCTOR OF ENGINEERING IN ELECTRICAL ENGINEERING
FACULTY OF ENGINEERING
KING MONGKUT'S INSTITUTE OF TECHNOLOGY LADKRABANG
2019
KMITL-2019-EN-D-018-013**

**COMPUTER-AIDED DIAGNOSIS AND GRADING SYSTEM OF
DIABETIC RETINOPATHY BASED ON COTTON WOOL SPOT
DETECTION**

SYNA SRENG



**A THESIS SUBMITTED IN PARTIAL FULFILLMENT
OF THE REQUIREMENTS FOR THE DEGREE OF
DOCTOR OF ENGINEERING IN ELECTRICAL ENGINEERING
FACULTY OF ENGINEERING
KING MONGKUT'S INSTITUTE OF TECHNOLOGY LADKRABANG
2019**

KMITL-2019-EN-D-018-013

This material is reserved for educational use only, not allowed for commercial use.

Forbidden to modify the content, and cite the document when use.



COPYRIGHT 2019
FACULTY OF ENGINEERING
KING MONGKUT'S INSTITUTE OF TECHNOLOGY LADKRABANG

This material is reserved for educational use only, not allowed for commercial use.

Forbidden to modify the content, and cite the document when use.

| | |
|---------------------|---|
| Thesis Title | Computer-Aided Diagnosis and Grading System of Diabetic Retinopathy Based on Cotton Wool Spot Detection |
| Student | Mr. Syna Sreng |
| Student ID | 57601475 |
| Degree | Doctor of Engineering |
| Program | Electrical Engineering |
| Year | 2019 |
| Advisor | Asst. Prof. Dr. Noppadol Maneerat |
| Co-Advisor | Prof. Dr. Kazuhiko Hamamoto |

ABSTRACT

Diabetic Retinopathy (DR) is the leading cause of blindness in working-age adults globally. Primary screening of DR is essential, and it is recommended that diabetes patients undergo this procedure at least once per year to prevent vision loss. However, in addition to the insufficient number of ophthalmologists available, the eye examination itself is labor-intensive and time-consuming. Thus, Computer-Aided Diagnosis (CAD) of DR using fundus images is proposed in this thesis to reduce the workload of ophthalmologists in the screening process and so that ophthalmologists may make effective treatment plans promptly to help prevent patient blindness. To complete the goal, this doctoral thesis presented the detail of the proposed methods into three tasks.

The first task is to develop an automatic system for screening the retinal image into DR or non-DR using hybrid simulated annealing and ensemble classification. The algorithm stands for the extraction of information-features from pathological signs of DR using morphological features, intensity features, color features, and texture features. The most significant features were selected based on the comparison of four famous feature selection methods namely genetic algorithm, particle swarm

optimization, hybrid ant colony optimization, and hybrid simulated annealing. The optimal feature set was used as the input into classifier to differentiate healthy retinal images and DR images. The evaluation results of the proposed method on a local dataset containing 1200 retinal images indicate that it performs better than previous methods, with accuracy 97.08%, sensitivity 90.90%, specificity 98.92%, precision 96.15%, F-measure 93.45% and the area under ROC curve 98.34%.

For further analysis, we also study on each DR pathologies detection using image segmentation level for red lesions detections, and classification level for the bright lesions detection. The evaluation results of the proposed methods on red lesions detection using local dataset containing 579 images indicate that they perform well for the time complexity with the average processing time 9.53s and 6.23s per image respectively for microaneurysms and hemorrhages detection. However, they got the limitation of accuracy 90%. It is showed that the use of only image segmentation level does not apply well with the poor-quality images.

For bright lesions detection, the classification level using machine learning approaches was adapted for detection of Cotton Wool Spots (CWSs) using adaptive thresholding and Ant Colony Optimization (ACO) coupling Support Vector Machine (SVM). It is the novelty of this thesis which stands for the proposed algorithm to segment the CWSs areas. Global thresholding can extract some bright objects in the retinal image (exudates and optic disc). However, global thresholding methods fail to detect CWSs areas because they use only one optimal value for all pixels in the image, even though CWSs appears very close to the background and is not clearly visible. In contrast, as adaptive thresholding works with sub-images locally and depends on the intensity values and changes dynamically over the image, it can solve this problem. Thus, adaptive thresholding is applied in this thesis to segment all appeared CWSs areas

on the retinal image and it is the novel idea of the detection of CWSs in the literature. The evaluation results of the proposed methods on local, DIARETDB1 and HRF datasets containing 319 images indicate that ACO coupling Cubic SVM performs better than previous methods with sensitivity 90.16%, specificity 97.92%, accuracy 96.96%, and area under receiver operating characteristic curve 97.19%.

The third task ends up with grading the severity of DR using deep learning approaches to make a complete computer-aided diagnosis system for DR. Despite recent advances of deep Convolutional Neural Networks (CNNs) in various medical image analysis tasks, their potential for DR detection has not been thoroughly explored. In particular, the applications of deep CNNs using fundus images for grading the severity of DR. In this thesis, the severity of DR has been graded into the healthy retina, non-proliferative DR and proliferative DR using five well-known deep learning models namely AlexNet, GoogleNet, InceptionV3, ResNet50, and ResNet101. Residual networks (i.e., ResNet50 and ResNet101) achieved the best performance compared to the rest with the accuracy of 90.57%. It is reasonable to conclude that deep learning models are suitable for grading of DR.

In summary, computer-aided diagnosis of DR is developed in this research work based on the analysis of fundus images using the combination of image processing techniques and machine learning approaches. It is a hope that our proposed system in this thesis will assist the eye specialists to diagnose diabetic retinopathy at an early stage so that the ophthalmologists can make effective treatment plans promptly to help prevent patient blindness.

ACKNOWLEDGEMENT

My acknowledgement goes to many people, who kindly contributed and helped during my doctoral degree.

Firstly, I would like to express my special appreciation and acknowledge to my advisors, Asst. Prof. Dr. Noppadol Maneerat and Prof. Dr. Kazuhiko Hamamoto for all advices, guidance, and suggestion during my doctoral study.

I would also like to thank my lab-mate, Ms. Khin Yadanar Win, who always share with me a lot of good ideas and time for discussion during revising my papers and learning new methods.

I wish to express my sincere thanks to Asst. Dr. Don Isarakorn, and Dr. Ronakorn Panjaphongse (M.D) for helping me to collect the retinal images from Bhumibol Adulyadej Hospital.

Special thanks to ASEAN University Network/Southeast Asia Engineering Education Development Network (AUN/SEED-Net) and King Mongkut's Institute of Technology Ladkrabang (KMITL) for financial support. In addition, I also would like to express my thoughtful gratitude to all professors, lecturers and supporting staffs in both Instrument and Control Engineering Department and Graduation Office, who always help and give me a guideline to process all the required documents.

I also wish to recognize all friends for the enjoyable and stimulating atmosphere that they provide with their companion and friendship.

Finally, I would like to express my greatest gratitude to my family members for unfailing supports and continuous encouragement throughout the years of my study.

Syna Sreng

TABLE OF CONTENTS

| | Page |
|---|-------------|
| ABSTRACT..... | I |
| ACKNOWLEDGEMENT | IV |
| TABLE OF CONTENTS..... | V |
| LIST OF TABLES | VIII |
| LIST OF FIGURES | X |
| LIST OF ABBREVIATIONS..... | XII |
| CHAPTER 1 INTRODUCTION | 1 |
| 1.1. Problem Statement and Objective..... | 1 |
| 1.2. Medical Background..... | 2 |
| 1.2.1 The Retinal Image..... | 2 |
| 1.2.2 Diabetic Retinopathy | 4 |
| 1.2.3 Screening of Diabetic Retinopathy | 6 |
| 1.3. Statement of Originality..... | 7 |
| 1.4. Thesis Structure | 8 |
| CHAPTER 2 PRIMARY SCREENING OF DIABETIC RETINOPATHY | 10 |
| 2.1 Introduction..... | 10 |
| 2.2 Methodology | 14 |
| 2.2.1 Image preprocessing | 16 |
| 2.2.2 Image Segmentation..... | 17 |
| 2.2.3 Feature Extraction..... | 18 |
| 2.2.4 Feature Selection..... | 19 |

This material is reserved for educational use only, not allowed for commercial use.

Forbidden to modify the content, and cite the document when use.

| | | |
|---|--|----|
| 2.2.5 | Classification..... | 21 |
| 2.3 | Experimental Results | 23 |
| 2.4 | Discussion..... | 29 |
| 2.5 | Summary | 30 |
| | | |
| CHAPTER 3 RED LESIONS DETECTION IN DIABETIC RETINOPATHY USING IMAGE SEGMENTATION | | 31 |
| 3.1 | Microaneurysms Detection Using Image Segmentation..... | 31 |
| 3.1.1 | Image Preprocessing | 32 |
| 3.1.2 | Microaneurysms Extraction | 34 |
| 3.1.3 | Small Bright Features Filtering..... | 36 |
| 3.1.4 | Microaneurysms Detection | 37 |
| 3.1.5 | Experimental Result..... | 39 |
| 3.2 | Automatic Hemorrhages Detection Based on Fundus Images | 39 |
| 3.2.1 | Image preprocessing | 42 |
| 3.2.2 | Red Feature Detection..... | 42 |
| 3.2.3 | Fovea Detection | 44 |
| 3.2.4 | Blood Vessels Detection..... | 45 |
| 3.2.5 | Hemorrhage Detection | 47 |
| 3.2.6 | Experimental Result..... | 48 |
| 3.3 | Summary | 49 |
| | | |
| CHAPTER 4 COTTON WOOL SPOTS DETECTION IN DIABETIC RETINOPATHY..... | | 50 |
| 4.1 | Introduction..... | 50 |
| 4.2 | Materials and Methods..... | 56 |
| 4.2.1 | Datasets and Ground Truth | 56 |

This material is reserved for educational use only, not allowed for commercial use.

Forbidden to modify the content, and cite the document when use.

| | | |
|---|---|------------|
| 4.2.2 | Image Preprocessing | 58 |
| 4.2.3 | Image Segmentation..... | 60 |
| 4.2.4 | Feature Extraction..... | 62 |
| 4.2.5 | Feature Selection..... | 64 |
| 4.2.6 | Classification..... | 65 |
| 4.3 | Experimental Results and Discussion | 66 |
| 4.4 | Summary | 72 |
| CHAPTER 5 GRADING OF DIABETIC RETINOPATHY USING DEEP | | |
| LEARNING | | |
| 5.1 | Introduction..... | 77 |
| 5.2 | Methods..... | 77 |
| 5.3 | Results and Discussion | 82 |
| 5.4 | Summary..... | 85 |
| CHAPTER 6 CONCLUSIONS AND FUTURE WORKS..... | | |
| 6.1 | Summary of the research works..... | 86 |
| 6.2 | Future works | 88 |
| Bibliography | | 89 |
| Appendix..... | | 120 |
| Presentations and Publications..... | | 114 |
| AUTHOR BIOGRAPHY..... | | 122 |

LIST OF TABLES

| Table | Page |
|---|-------------|
| Table 2.1 Features extraction and its description..... | 19 |
| Table 2.2 Feature selection methods | 23 |
| Table 2.3 Classification methods | 23 |
| Table 2.4 Number of each pathological signs of retinal images. | 23 |
| Table 2.5 Classification results based on HSA coupling with different classifiers. ... | 25 |
| Table 2.6 Classification results based on GA coupling with different classifiers..... | 25 |
| Table 2.7 Classification results based on PSO coupling with different classifiers | 26 |
| Table 2.8 Classification results based on HACO coupling with different classifiers. | 26 |
| Table 2.9 AUROC for different pairs of feature selection and classifiers. | 27 |
| Table 2.10 Comparison of the proposed method with previous works..... | 28 |
| Table 4.1 Specifications of datasets used in this study. | 57 |
| Table 4.2 Extracted features..... | 63 |
| Table 4.3 Feature selection methods | 63 |
| Table 4.4 Classification results using GA paring with four SVM classifiers | 68 |
| Table 4.5 Classification results using PSO pairing with four SVM classifiers..... | 68 |
| Table 4.6 Classification results using ACO pairing with four SVM classifiers | 68 |
| Table 4.7 Classification results using stepwise method pairing with four SVM classifiers..... | 69 |
| Table 4.8 AUROC of different pairs of feature selection and SVM classifiers | 69 |
| Table 4.9 The performance of the previous works and our proposed method..... | 71 |
| Table 5.1 Traditional machine learning and deep learning | 75 |
| Table 5.2 Datasets descriptions | 83 |
| Table 5.3 Performance evaluation of deep learning methods for original data | 83 |

Table 5.4 Performance evaluation of deep learning methods with image enhancement

.....83



LIST OF FIGURES

| Figure | Page |
|--|-------------|
| Figure 1.1 Anatomy of human retina (images credits [7-8]) | 3 |
| Figure 1.2 Fundus image of normal retina | 4 |
| Figure 1.3 Diagrams of retina with diabetic retinopathy lesions (image credits [7-8]) | 5 |
| Figure 1.4 Vision affected by DR (image credits [12]) | 5 |
| Figure 1.5 Normal anatomical structures and pathological signs of diabetic retinopathy | 6 |
| Figure 1.6 Pathological signs and severity of diabetic retinopathy | 6 |
| Figure 1.7 Diagnosis of diabetic retinopathy | 7 |
| Figure 1.8 Scope of the thesis | 8 |
| Figure 2.1 Healthy fundus image and pathological signs of DR. | 11 |
| Figure 2.2 Representative pathological signs of DR | 15 |
| Figure 2.3 Flowchart of the proposed system | 15 |
| Figure 2.4 Image quality assessment metrics..... | 16 |
| Figure 2.5 The processing steps of image segmentation | 18 |
| Figure 2.6 Pseudo code for hybrid simulated annealing | 20 |
| Figure 2.7 Flowchart of ensemble bagging classifier | 22 |
| Figure 2.8 ROC curves of each classifiers | 27 |
| Figure 3.1 Block diagram for microaneurysms detection. | 32 |
| Figure 3.2 The visual results of preprocessing step | 33 |
| Figure 3.3 Microaneurysms extraction processes | 35 |
| Figure 3.4 Small bright features extraction..... | 37 |
| Figure 3.5 Microaneurysms detection..... | 38 |

| | |
|--|----|
| Figure 3.6 Block diagram for hemorrhages detection..... | 41 |
| Figure 3.7 Preprocessing step for hemorrhages detection | 42 |
| Figure 3.8 Red features detection | 43 |
| Figure 3.9 The processes of fovea detection..... | 45 |
| Figure 3.10 The processes of fovea elimination | 45 |
| Figure 3.11 Blood vessels detection | 45 |
| Figure 3.12 Hemorrhages detection | 48 |
| Figure 4.1 Ground truth image for CWSs from DIARETDB1..... | 56 |
| Figure 4.2 Block diagram depicting the proposed system | 58 |
| Figure 4.3 IQMM for the image quality improvement | 59 |
| Figure 4.4 Performance of different window sizes of adaptive thresholding | 61 |
| Figure 4.5 Image segmentation results | 62 |
| Figure 4.6 Pseudo code for ACO | 64 |
| Figure 4.7 ROC curves..... | 70 |
| Figure 4.8 The visual results of detected cotton wool spots from images with the presence of CWSs in different degree | 71 |
| Figure 5.1 Traditional machine learning frame work | 74 |
| Figure 5.2 Deep learning frame work | 74 |
| Figure 5.3 The Overview of convolutional neural networks (LeNet5)..... | 78 |
| Figure 5.4 Different deep CNN architecture..... | 81 |
| Figure 5.5 Proposed framework for grading the severity of DR | 82 |
| Figure 5.6 The concept of transfer learning for grading the severity of DR..... | 83 |
| Figure 5.7 The confusion matrix of ResNet50 for original data..... | 85 |
| Figure 5.8 The confusion matrix of ResNet101 with enhanced images | 86 |

LIST OF ABBREVIATIONS

| | |
|--------------|--|
| ACO | Ant Colony Optimization |
| ANN | Artificial Neural Network |
| AUROC | Area Under Receiver Operator Characteristics |
| BV | Blood Vessels |
| CII | Contrast Improvement Index |
| CNN | Convolutional Neural Network |
| CWSs | Cotton Wool Spots |
| DR | Diabetic Retinopathy |
| DT | Decision Tree |
| EB | Ensemble Bagging |
| EXs | Exudates |
| GA | Genetic Algorithm |
| GLCM | Gray Level Co-occurrence Matrix |
| GLRLM | Gray Level Run Length Matrix |
| HMs | Hemorrhages |
| HACO | Hybrid Ant Colony Optimization |
| HSA | Hybrid Simulated Annealing |
| KNN | K Nearest Neighbor |
| LDA | Linear Discriminant Analysis |
| LR | Logistic Regression |
| MAs | Microaneurysms |
| NPDR | Non-Proliferative Diabetic Retinopathy |
| OD | Optic Disc |
| PCA | Principal Component Analysis |
| PDR | Proliferative Diabetic Retinopathy |
| PSO | Particles Swarm Optimization |
| PSNR | Peak Signal-to-Noise Ratio |
| SA | Simulated Annealing |
| SVM | Support Vector Machine |

This material is reserved for educational use only, not allowed for commercial use.

Forbidden to modify the content, and cite the document when use.

CHAPTER 1

INTRODUCTION

This chapter presents an overview of the research works in this thesis, mainly, its problem statement and objective, the background of medical image related to diabetic retinopathy, statement of originality, and finally, the thesis structure. All experiments in this thesis are done in MATLAB.

1.1 Problem Statement and Objective

As reported in the International Diabetes Federation Diabetes Atlas 2017 [1], an estimated 425 million adults were living with diabetes as of 2017, and approximately one-third of diabetes patients had some degree of diabetic retinopathy. Consequently, it is recommended that people with diabetes undergo eye-screening at regular yearly intervals to help prevent vision loss. This eye screening can be performed by a retina specialist either directly or by first using a fundus camera to capture the retinal image, followed by a screening process [2]. However, the process is currently labor-intensive, time-consuming and subjective. In addition, the number of ophthalmologists available is insufficient in many countries, especially in developing countries and rural areas where eye specialists are rarely available. In response to the problem, primary screening and classification of DR are essential to reduce the time and cost of treatment, identify DR more objectively, and enable ophthalmologists to make effective treatment plans in order to help prevent patient blindness.

The main objective of this thesis is to develop an accurate computer-aided diagnosis system of DR which can be implemented using fundus images. The main

focuses are on the accurate of an automatic screening and classification of DR pathologies using the capabilities of computer vision method in the segmentation level and machine learning for the classification task as well as deep learning approaches for grading the severity of DR.

To achieved the goal, the proposed methods are divided into three tasks:

1. The first task is to develop an automatic system for screening the retinal image into DR or non-DR. It is currently the primary need at hospital since about one in third people living with diabetes have affected by DR.
2. For further analysis, we also study on each lesions detection using image segmentation level for red lesions detections and classification level for bright lesions detection.
3. Finally, the severity of DR is graded using deep learning approaches to make a complete computer-aided diagnosis system for DR.

1.2 Medical Background

The necessary technical terms of the medical background used in this thesis will be briefly introduced with the start of the retinal image in subsection 1.2.1, followed by diabetic retinopathy in subsection 1.2.2 and finally end up with the screening process of diabetic retinopathy in subsection 1.2.3.

1.2.1 The Retinal Image

In the visual system, the eye is an organ composed of three layers: the outermost layer, the middle layer, and the innermost layer. Retina is the innermost and thin layer known as the light-sensitive layer. It contains photosensitive cells which convert

incident light into signals which are then carried to the brain by the optic nerve. The brain then processes the signal which finally allows us to see and interpret the object in front of our eyes. It means that our eyes can see any objects by the light that reflect from those objects go inside the eyes. The incoming light first passes through the cornea, the clear dome that refracts the light to the lens. The light then refracts at the second times while passing through the lens and next, retinal it works like the film in a camera by recording that light. Macula is the central area of the retina, temporal to the optic disk. It is responsible to have fine central vision and color vision. The center of macula is called fovea. This region of the retina is the most sensitive region. Finally, the light is transmitted to the brain through the optic nerve or it can be called Optic Disk (OD). OD is the bright yellowish disk, from which, blood vessels and optic nerve fibers emerge. The blood vessels are originated from the central retinal artery and vein that lie in the OD. These blood vessels nourish the internal parts of retina and radiate out from the optic disk [3-5]. Figure 1.1 depicts the anatomy and structures of the human eye. The retinal image, as shown in Figure 1.2 is captured by a fundus camera, contains three important components; optic disc, macula, and blood vessel.

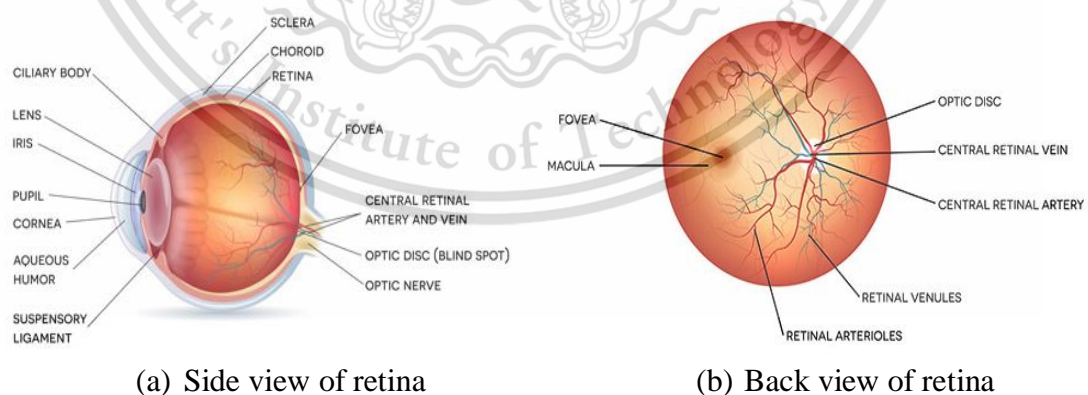


Figure 1.1 Anatomy of human retina (images credits [6-7]).

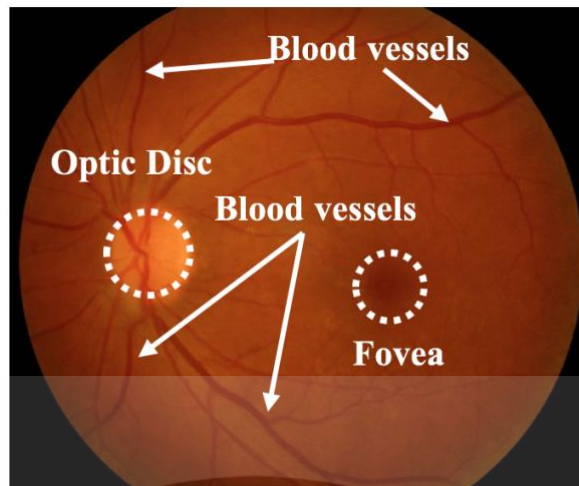


Figure 1.2 Fundus image of normal retina.

1.2.2 Diabetic Retinopathy

Diabetes is a lifelong disease which has been identified as one of the leading causes of many health problems including renal failure, heart attacks, strokes, and eye complications. It occurs when sugar in the blood is not digested properly, either because the pancreas is unable to produce sufficient insulin, or because the body is not using the insulin it produces correctly [8]. When diabetes affects the eye, it is called Diabetic Retinopathy. It is the main cause of blindness in working-age adults globally and categorized into two stages. Microaneurysms (MAs), Exudates (EXs), and Hemorrhages (HMs) are the early signs of DR known as Non-Proliferative Diabetic Retinopathy (NPDR), while neovascularization, vitreous hemorrhages, and fibrous proliferation occur during the advanced stage of DR, known as Proliferative Diabetic Retinopathy (PDR). MAs are the first visible sign of DR and defined as dark red fundus spots. HMs are also dark red lesions, which appear as dots, blot or flame-shaped in the fundus image. They are the results of blood vessels bleeding either from superficial or deep capillary plexus. EXs are MAs exuded combined with the leakage of lipids in the

retina. They appear as pale white or fluffy patches (soft EXs) or bright yellowish dots (hard EXs) in the inner retina. Neovascularization is the development of immature blood vessels which usually occur as a result of generalized retinal ischemia. Vitreous hemorrhage is the result of hemorrhage or blood bleeding into the vitreous humor, and fibrous proliferation is fibrous tissue opaque enough to be seen at the OD area or somewhere around the OD margin with or without accompanying new blood vessels [9-11]. The pathologies of DR are depicted in Figure 1.3. Figure 1.4 shows the vision affected by DR. The pathologies and severity of DR on fundus images are shown in Figure 1.5 and Figure 1.6 respectively.

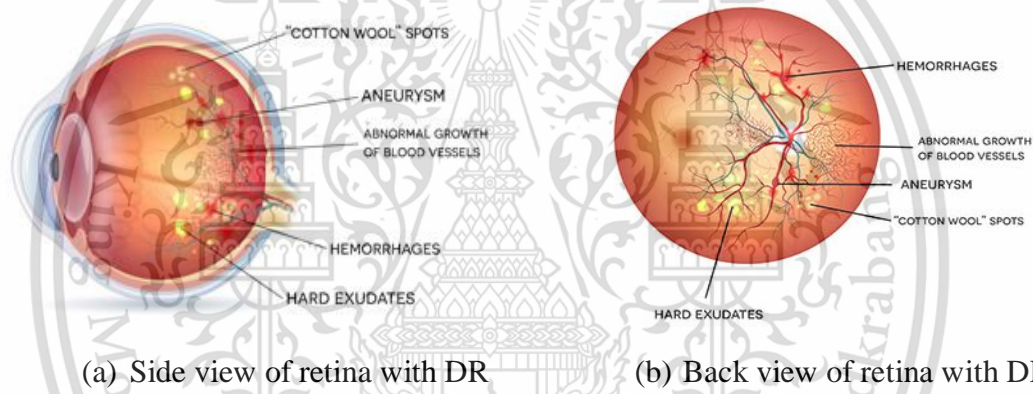


Figure 1.3 Diagrams of retina with diabetic retinopathy lesions (image credits [6-7]).



Figure 1.4 Vision affected by DR (image credits [12]).

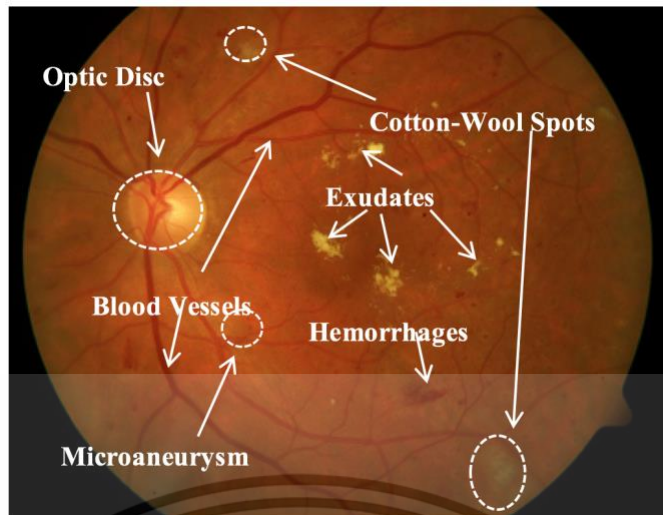


Figure 1.5 Normal anatomical structures and pathological signs of diabetic retinopathy.

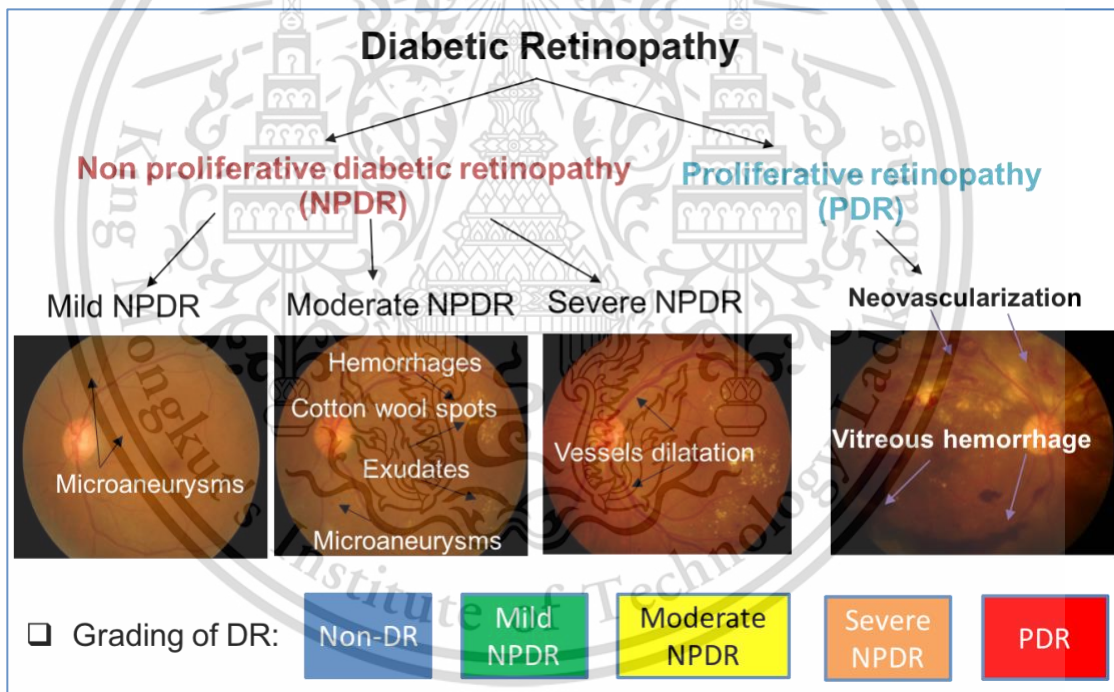


Figure 1.6 Pathological signs and severity of diabetic retinopathy.

1.2.3 Screening of Diabetic Retinopathy

The DR screening is currently subjective and performed by the retina specialists either directly or first using a fundus camera to capture the retinal image, followed by

the screening process [13-14] as illustrated in Figure 1.7. In Figure 1.7 (a), the eye examination is performed by an expert using the ophthalmoscope to check the patient whether the eye is affected by DR or not. The eye fundus photography, Figure 1.7 (b), is taken from a fundus camera so the images data can be stored, which makes disease monitoring easier. It can be transmitted over short distances throughout a clinic or over large distances via electronic transfer. In addition, with the fundus images, the diagnosis can be performed automatically by using computer vision techniques.

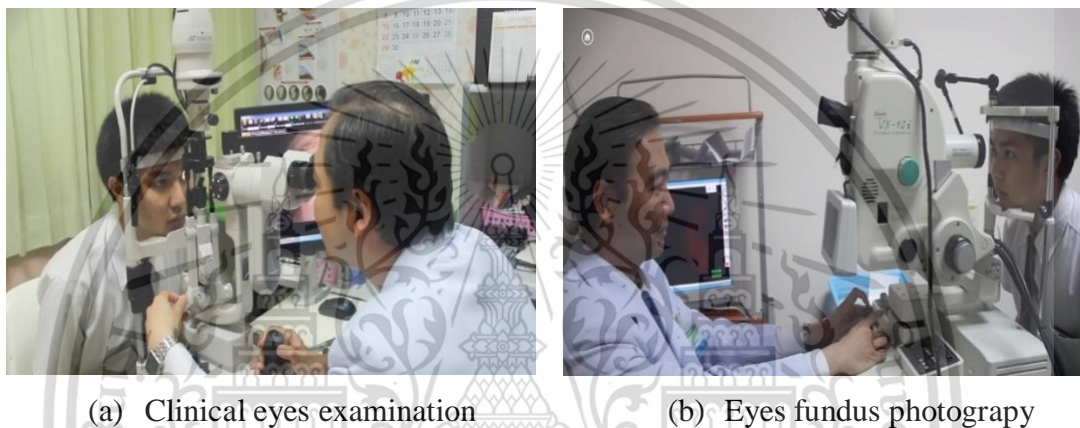


Figure 1.7 Diagnosis of diabetic retinopathy.

1.3 Statement of Originality

The scope of this thesis is to develop computer-aided diagnosis and grading system of diabetic retinopathy as presented in Figure 1.8. It consists of three main steps; screening the retinal images into DR and healthy images, detection of each DR lesions, and finally grading the severity of DR.

The major contributions of this thesis are listed below:

- Development of an algorithm for primary screening of diabetic retinopathy using hybrid simulated annealing and ensemble bagging classifier.
- Development of the automated detection of microaneurysms and

hemorrhages respectively using fundus image based on morphological operation and image segmentation methods.

➤ Development of a new framework for detection of cotton wool spots in diabetic retinopathy based on adaptive thresholding and ant colony optimization coupling support vector machine.

➤ Development of a novel grading system of DR using deep learning approaches.

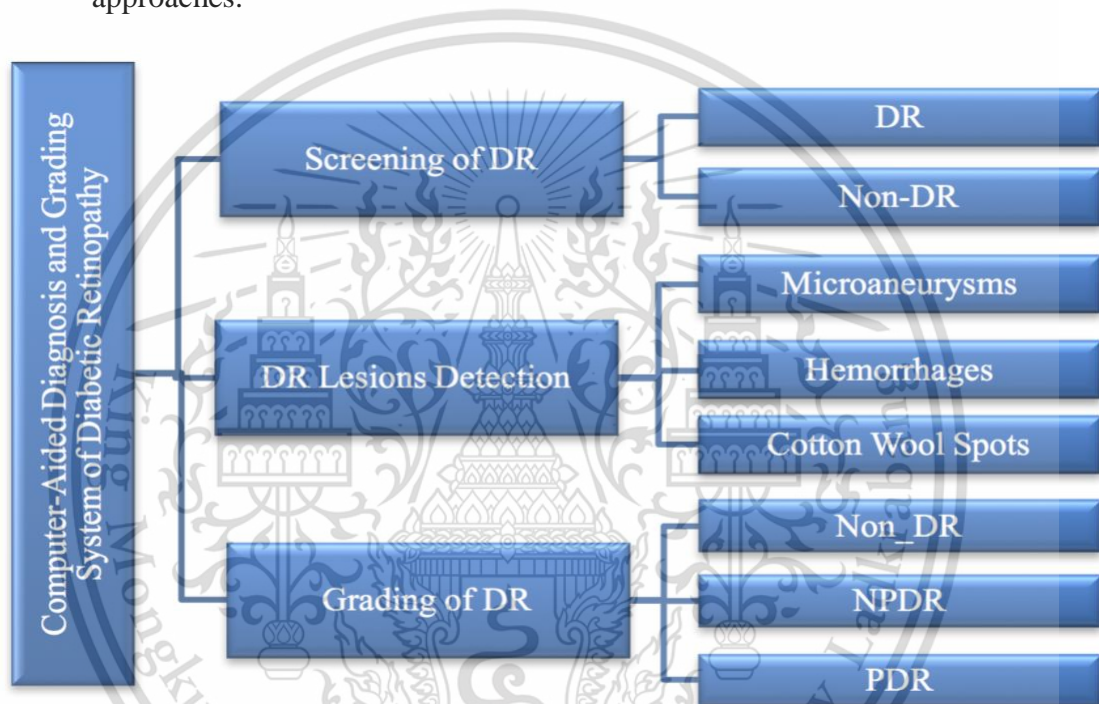


Figure 1.8. Scope of the thesis.

1.4 Thesis Structure

The organization of this thesis is managed as follow:

Chapter 1 presents the main purpose of this thesis writing including problem statement and objective, medical background, the statement of originality and the organizing of the thesis structure. This chapter works as a guideline to understand the main objective of this research work as well as a useful medical background

information related to diabetic retinopathy and its screening process.

Chapter 2 investigates the use of hybrid simulated annealing and ensemble classification for the primary screening of DR. The algorithm stands for extraction of information-features from the segmented region of interests. Then the most significant features were selected as the input into classifier to differentiate healthy retinal images and DR images.

Chapter 3 devotes the detail on describing the proposed framework and the methods that are applied and combined for red lesions detection (MAs and HEs) using images segmentation. This chapter presents the different segmentation methods to detect MAs and HEs and how the noise is removed to prevent interference from the final results.

Chapter 4 provides the result of Cotton Wool Spots (CWSs) detection based on adaptive thresholding and ant colony optimization coupling support vector machine. Initially, all possible bright lesions are segmented and then three types of noise are removed to avoid interference in the final results. Then, the combination of computer vision technique and machine learning approaches is used to differentiate CWSs from other bright objects.

Chapter 5 presents the grading system of the DR severity using deep learning approaches. The severity of DR is graded into healthy, NPDR and PDR based on five CNN models namely AlexNet, GoogLeNet, ResNet50, Inception V3 and ResNet101.

Chapter 6 end up with the conclusion and future work direction.

CHAPTER 2

PRIMARY SCREENING OF DIABETIC RETINOPATHY

As presented in chapter 1, the screening of DR is essential to help diabetes patients for the eye examine since about two in third people living with diabetes have no affected by DR. In this chapter, we will present the processing steps proposed to screen the health retinal images from DR images using hybrid simulated annealing and ensemble bagging classifier.

2.1 Introduction

Diabetic Retinopathy is the leading cause of blindness in working-age adults globally. Primary screening of DR is essential, and it is recommended that diabetes patients undergo this procedure at least once per year to prevent vision loss. However, in addition to the insufficient number of ophthalmologists available, the eye examination itself is labor-intensive and time-consuming. Thus, an automated DR screening method using retinal images is proposed in this chapter to reduce workload of ophthalmologists in the primary screening process and so that ophthalmologists may make effective treatment plans promptly to help prevent patient blindness. The anatomy of a healthy retinal image and pathological signs of DR image are shown in Figure 2.1 and Figure 2.2. In our review of previous works, we found that several papers aimed to detect each pathological sign of DR: EXs, MAs, and HMs. However, only a few papers were devoted to differentiating between healthy and unhealthy retinal images.

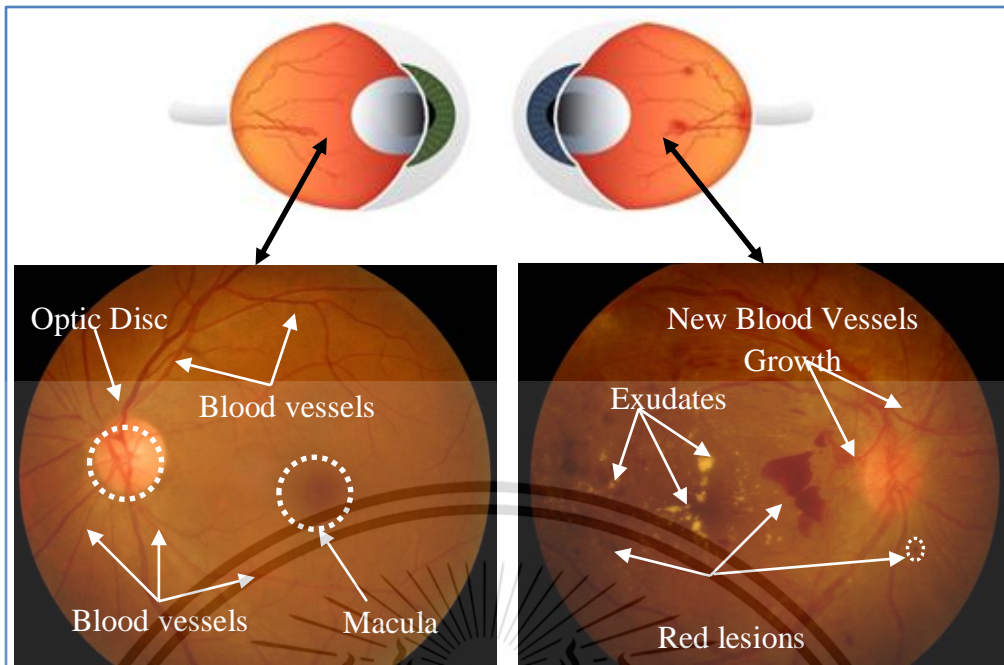


Figure 2.1 Healthy fundus image and pathological signs of DR.

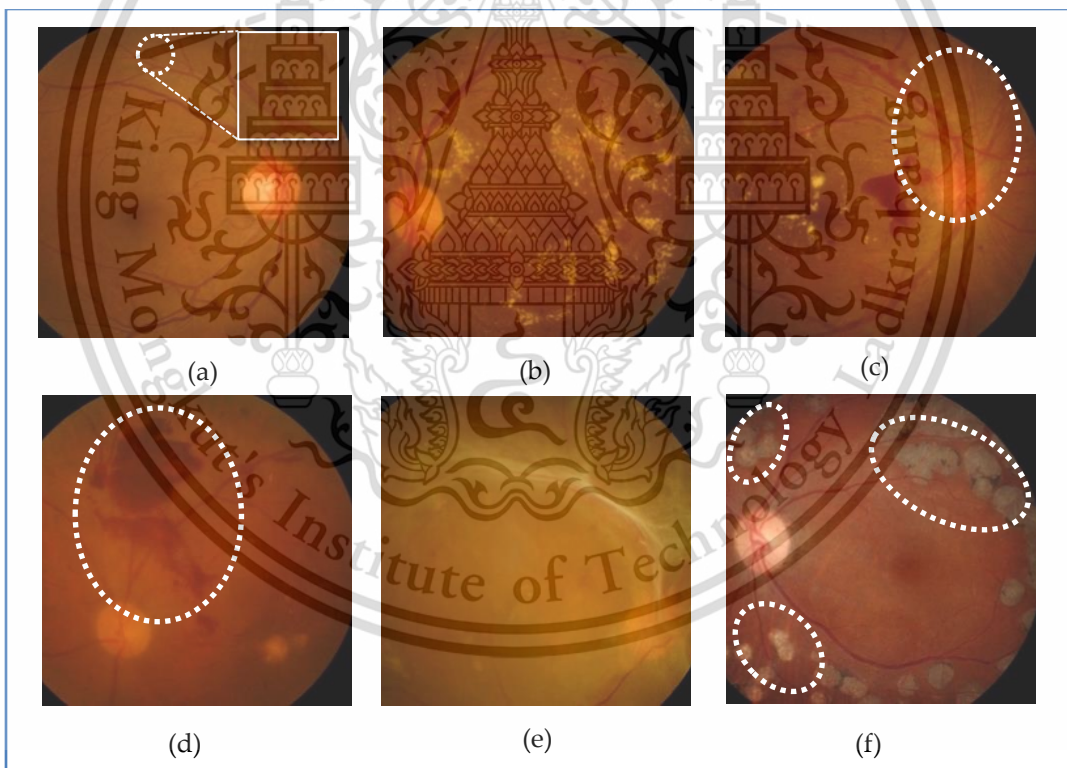


Figure 2.2 Representative pathological signs of DR: (a) Mild NPDR; (b) Severe NPDR; (c) Neovascularization; (d) Vitreous hemorrhages; (e) Fibrous proliferations and (f) Laser scars after treatment.

Acharya et al. [15] proposed an automated screening system to discriminate healthy retinal images using a support vector machine for three different eye diseases namely DR, glaucoma and age-related macular degeneration. First, an image was preprocessed using adaptive-histogram equalization, and then a bi-dimensional empirical mode decomposition technique was applied to decompose the image due to pixel variations. Texture features were later extracted from 2D intrinsic mode functions and ranked as inputs for feeding the support vector machine. The paper reported an accuracy of 88.63 %, a sensitivity of 86.25% and a specificity of 91%. The improved version of this paper was published in [16]. A 2D-continuous wavelet transform was used first to decompose the fundus images, and then 15 features from entropies and energy features were extracted. These significant features were ranked and selected using particle swarm optimization. Finally, an adaptive synthetic sampling approach was applied to balance the input data which was then differentiated into 2 data classes using a random forest classifier. The updated results showed an accuracy of 92.48%, a sensitivity of 89.37% and a specificity of 95.58%.

Kumar et al. [17] classified DR or healthy retinal images using the aggregate of the extracted lesions. The OD and BV were first detected. Then the white lesions and red lesions were detected through modification of their previous work presented in [18] and [19] respectively. Finally, the detected lesions were classified based on a waterfall model based classification. Rates of 80% and 50% for sensitivity and specificity were reported respectively.

Imani et al. [20] presented a DR screening system based on morphological component analysis. Without using any segmentation methods, the structural information was exploited to evaluate performance. The blood vessels and lesions were

then separated using morphological component analysis. Finally, a support vector machine was employed to distinguish healthy retinal images from abnormal ones. It achieved the accuracy 92.82%, sensitivity 92.01% and specificity 95.45%.

Goh et al. [21] filtered the retinal healthy images from DR based on the result of exudates detection using the features of the sub-images locally as the input to multiple classifiers. The paper obtained sensitivity 92% and specificity 91%.

A grading system for DR was presented by Akram et al. [22] which uses the number of each detected DR lesion as determined through morphological operation. Aliahmad et al. [23] presented the automatic analysis of fundus images for modeling early changes in retinal blood vessels resulting from diabetes based on the total number of branching angles and average acute branching angles in addition to patient demographic information. Linear regression was applied in this study. Similarly, Raja et al. [24] proposed a method to detect BV for the diagnosis of DR.

Taking into account the works mentioned above, the methods in [21], the author's attempt to detect only the EXs while other DR lesions including MAs, HMs, and CWSs were ignored. When ignoring other associated lesions, the detection system is not robust. The papers in [17] and [20] filtered any abnormal signs of DR using all extracted features whether significant differences existed or not. The use of all features without the use of feature selection may lead to heavy computation time, redundancy, and poor predictive performance. The paper in [15] and [16] applied a feature selection to select the optimal feature set to feed to the classifiers. However, more feature selection methods should be studied and the results compared.

In this chapter, we propose an automated DR screening system based on five processing steps: (i) preprocessing, (ii) lesion detection, (iii) feature extraction, (iv)

feature selection and (v) classification. Image preprocessing is completed first so as to standardize image size and improve retinal image quality. Then, bright and dark lesions are segmented using a combination of morphological-top-hat and Kirsch edge-detection methods using a Boolean operation. Post-processing is further applied to filter out only DR lesions. After the DR lesions are segmented, 8 feature sets with a total of 208 features are extracted, and hybrid simulated annealing is utilized to select the optimal feature set for input to the ensemble bagging classifier. The rest of this chapter is organized into four sections. Section 2.2 outlines the materials and methods used in the study. The experimental results are described in Section 2.3. Section 2.4 and Section 2.5 present the discussions and conclusions, respectively.

2.2 Methodology

The flowchart of the proposed method is depicted in Figure 2.3. It composes of five processing steps: 2.2.1. Image Processing, 2.2.2. Image Segmentation, 2.2.3. Feature Extraction, 2.2.4. Feature Selection and 2.2.5. Classification.

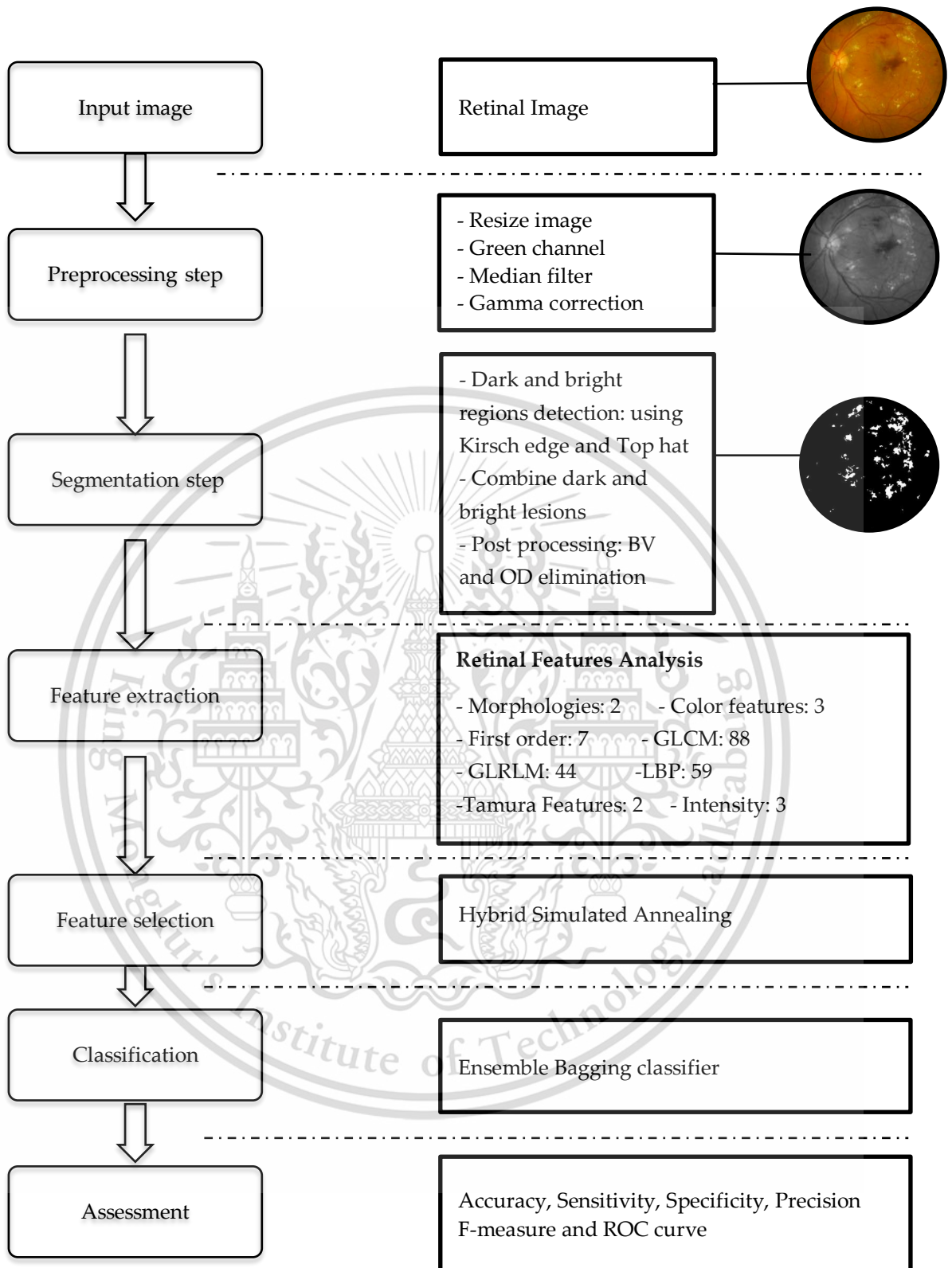


Figure 2.3 Flowchart of the proposed system.

2.2.1 Image preprocessing

The uneven illumination inside the retinal images usually causes by the process of image acquisition and the main focus of retinal image analysis (nasal view and macula view) [3]. In our dataset, most images were captured for the purpose of macular view in which the illumination is highly focused on the macular area and image pixels at the outer ring of pixels saturation [25]. Thus, image preprocessing is done first to standardize the image size and improve the retinal image quality. The following procedures are used to preprocess the retinal images based on the image quality assessment metrics [26], as shown in Figure 2.4.

1. Image resizing to 576×720 pixels to standardize the image size and reduce the computation time.
2. RGB color image conversion to the green channel, followed by removal of small noise using a median filter.
3. Gamma correction to improve the intensity values for image binarization.

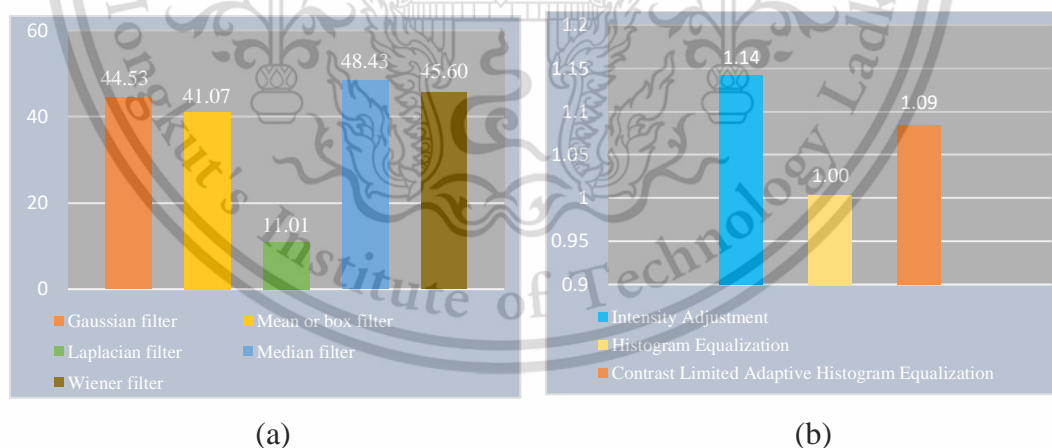


Figure 2.4 Image quality assessment metrics: (a) peak signal to noise ratio (PSNR) comparison for filtering methods, and (b) contrast improvement index (CII) comparison for contrast enhancement methods.

2.2.2 Image Segmentation

Image segmentation can be considered as the main processing steps in many application of image processing [27]. Numerous applications have been presented the segmentation methods based on image intensity, color, edges, and texture. In this section, the lesions of DR are segmented based on Kirsch edges detection and morphological top hat which is presented as following:

1. Detect bright lesions by using Kirsch edge detection. Kirsch operator is first proposed by R.A. Kirsch [28], and it was applied in [29] to detect the blood vessels of the retinal images.
2. Detect red lesions by complementing the preprocessed image first to reverse the intensity values for the further process in the detection of red lesions. Then, the background of the image is detected by using morphological opening. The radius of 10 of the disk- shaped structuring element is used to detect the background by applying “strel” function in MATLAB. Finally, the red objects can be detected after subtraction the background from the complemented image.
3. Combine all bright and dark objects.
4. Since the resulted image contains blood vessels and some noises near the vicinity of the optic disc area, morphological operation is applied. The main BV is first eroded by a disk-shaped structuring element with the radius equal to one. Then the remained parts of BV are further removed using the ratio between the major axis length and minor axis length. Finally, we remove the artifacts in the vicinity of the OD by first localizing the OD using our method proposed in [30], and then build a rectangular mask from the center of the detected OD area. By combining the rectangular mask with the result after eliminating BV, we can remove all noise attached to the rectangular mask.

The processing steps of image segmentation are presented in Figure 2.5.

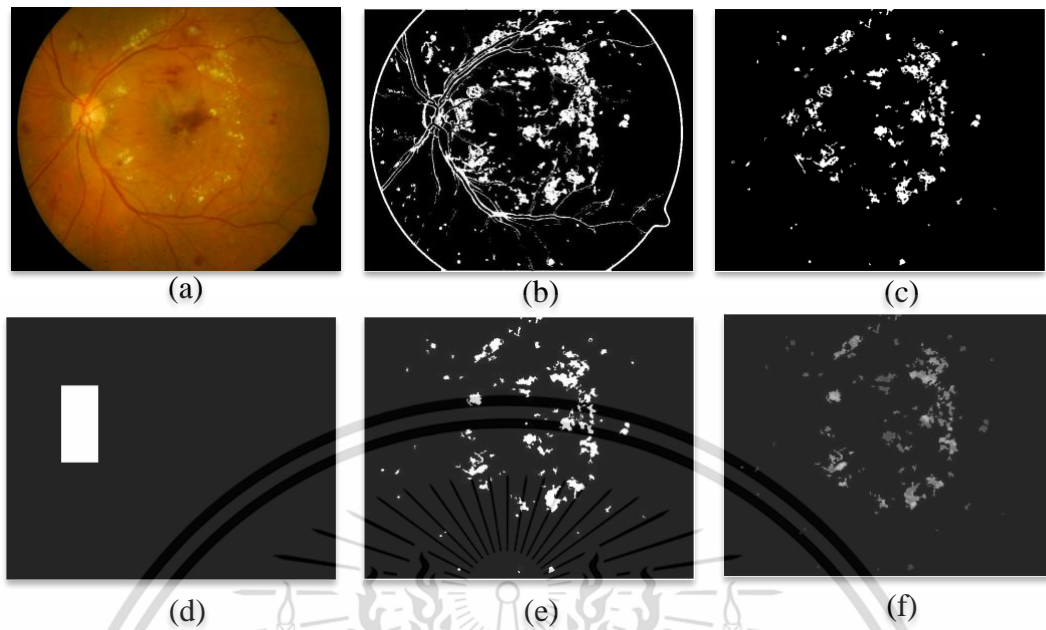


Figure 2.5 The processing steps of image segmentation: (a) Retinal image; (b) DR lesions detection; (c) Blood vessels elimination; (d) Rectangular mask (e) Resulted image after post processing step and (f) segmented result in grayscale image.

2.2.3 Feature Extraction

After image segmentation, we reconstruct the binary image into a grayscale image using morphological reconstruction, and then we differentiate the retinal health and DR images based on the pixel density in binary image (see in Figure 2.5(e)) and the information of texture, color, and intensity of the detected regions (see in Figure 2.5(f)). 208 features from eight feature extractors namely morphological features, intensity features, color features, first order statistical features, GLCM features, GLRLM features, local binary pattern features and Tamura's texture features are extracted as illustrated in Table 2.1 and detail in Appendix A.

Table 2.1 Features extraction and its description

| Features | | Description |
|----------------------------------|-----------|--|
| Morphological features | F1 | Total area of detected regions |
| | F2 | Total length of boundary of detected regions |
| Intensity features | F3-F5 | The mean values of maximum intensity, mean intensity and minimum intensity of the segmented image. |
| Color features | F6-F8 | The mean intensity in hue, saturation and value in HSV color space of the segmented image. |
| First order statistical features | F9-F15 | The mean, standard deviation, smoothness, variance, skewness, kurtosis and energy of intensity of the segmented image. |
| GLCM features | F16-F103 | Four orientations of 22 features in GLCM matrix of the segmented image [31] |
| GLRLM features | F104-F147 | Four orientations of 11 features in GLRLM matrix of the segmented image [32] |
| Local Binary Pattern Features | F148-F206 | 59 features from local binary pattern features [33] |
| Tamura's Texture Features | F207-F208 | Coarseness value and Contrast value from Tamura's texture features of the segmented image [34] |

2.2.4 Feature Selection

The process of feature selection is to choose the optimal feature set as the input for classification. Directly using all features may include the irrelevant features which can cause heavy computation time, redundancy, and even reduce the predictive performance. To remedy the aforementioned problems, the initial feature set of 208 features from feature extraction is filtered by Hybrid Simulated Annealing (HSA) optimization. Simulated Annealing (SA), introduced by Kirkpatrick et al., is one of the metaheuristic algorithms inspired by the process of annealing in metallurgy [35]. The main advantage of SA over other methods is its ability to avoid being trapped at

local optima. However, the use of a single method sometimes fails to optimize the problems when a huge number of features are applied or there is a high degree of epistasis between features [36]. For this reason, many researchers have proposed the hybrid approaches to combine complementary strengths and to overcome the drawbacks of single methods by embedding in them one or more steps involving alternative techniques [37]. In this study, we implement the HSA similar to Yarpiz in [38] by embedding a multi-layer perceptron neural network in SA as presented in Figure 2.6.

```

Initialize: - Input data  $X$ 
              - Initial temperature  $T_0$ 
              - Temperature reduction rate  $\alpha$ 
              - Maximum number of iteration  $It_{max}$ 
 $X_0 \leftarrow GenerateInitialSolution X$ 
 $f(X_0) \leftarrow CostFunction\_ANN(X_0)$ 
 $X_{best} \leftarrow X_0$ 
 $T \leftarrow T_0$ 
while( $\neg Stopcondition$ )
  for ( $i = 1 : It_{max}$ )
     $X_{new} \leftarrow ConstructNeighbourSolution(X_0)$ 
     $f(X_{new}) \leftarrow CostFunction\_ANN(X_{new})$ 
    if  $f(X_{new}) \leq f(X_n)$ 
       $X_n \leftarrow X_{new}$ 
    if  $f(X_{new}) \leq f(X_{best})$ 
       $X_{best} \leftarrow X_{new}$ 
    end
    elseif  $\exp\left(\frac{f(X_n) - f(X_{new})}{T}\right) > rand()$ 
       $X_n \leftarrow X_{new}$ 
    end
  end
   $T = T * \alpha$ 
end
Return ( $X_{best}$ )

```

Figure 2.6 Pseudo code for hybrid simulated annealing.

To show the efficiency of the proposed feature selection method, we also examined three robust feature selection methods as shown in Table 2.2, which are the population-based nature-inspired optimization methods.

Table 2.2 Features selection methods

| Nature-inspired optimization methods | |
|---|--|
| Genetic Algorithm (GA) | <ul style="list-style-type: none"> - Introduced by John Holland (1960) - Officially in Holland's book (1975) - A search method that emulates the principles of genetic reproduction operations: crossover and mutation. |
| Particle Swarm Optimization (PSO) | <ul style="list-style-type: none"> - Developed by Eberhart and Kennedy (1995) - Inspired by social behavior of bird flocking |
| Hybrid Ant Colony Optimization (HACO) | <ul style="list-style-type: none"> - ACO is inspired by the behavior of natural ants looking for the food. - HACO is implemented similar to Yarpiz in [6] by embedding a multi-layer perceptron neural network in ACO. |

2.2.5 Classification

Once the features are selected, they are fit as input to the ensemble bagging classifier. It is one of the best classifiers for unbalance data classification and first introduced by Leo Breiman [39]. The basic concept of bagging is illustrated in Figure 2.7. Firstly, bootstrap samples are drawn from the original training data to form an ensemble then each bootstrap sample is trained by a decision tree classifier separately, and finally the classifier outputs are combined and selected using majority vote. To compare the results, we also examined other five classifier methods as shown in Table 2.3

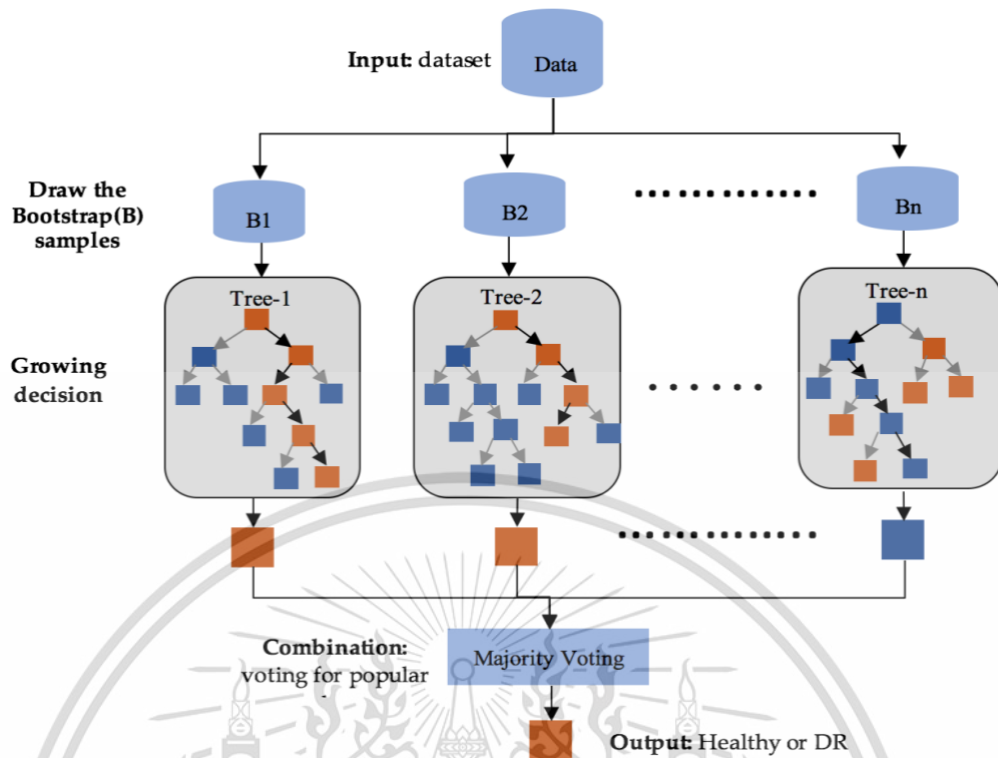


Figure 2.7 Flowchart of ensemble bagging classifier.

Table 2.3 Classification methods

| Classifiers | |
|------------------------------------|---|
| Support Vector Machine (SVM) | - A classifier performed the test by finding the hyperplane that maximizes the margin of different classes. |
| Decision Tree (DT) | - A classifier that uses a tree-like model of decisions to perform the classification. A test is represented by each node, an outcome of the test is represented each branch, and a class label is represented by each leaf node. |
| Logistic Regression (LR) | - A regression model used in predictive analysis when the output y is either zero or one (binary classes). |
| Linear Discriminant Analysis (LDA) | - Performs a classification based on reducing dimensional problems, and it is commonly used as preprocessing step in machine learning and pattern classification. |
| K-Nearest Neighbors (KNN) | - Performs a classification by grouping the objects in training set into k numbers bases the assignment of a label on the majority of a particular class in its neighborhood. |

2.3 Experimental Results

A total of 1200 retinal images with the resolution of 3872 x 2592 pixels in 24-bit JPEG format from Bhumibol Adulyadej Hospital have been used to evaluate our proposed method in which 70% of images are used for training and the remaining images are used for testing. The images are separated into 7 groups by the ophthalmologists as illustrated in Table 2.4. In this chapter, the proposed method is tested using MATLAB R2016b on a laptop with i3 processor and 2 GB RAM.

Table 2.4 Number of each pathological signs of retinal images

| Pathological signs of retinal images | Number of images |
|--------------------------------------|------------------|
| Healthy retinal images | 218 |
| Mild and Moderate NPDR | 318 |
| Severe NPDR | 312 |
| New blood vessels growing | 36 |
| Neovascularization | 115 |
| Fibrous proliferations | 160 |
| Scar | 41 |
| Total | 1200 |

The experiment is conducted as outlined in the following procedure:

1. All appeared lesions is segmented by improving our previous method in [40].
2. Eight feature sets namely morphological features, intensity features, color features, first order statistical features, GLCM features, GLRLM features, local binary pattern features and Tamura's texture features are extracted.

3. The highlights comparative studies on Genetic Algorithm(GA) [41], Particle Swarm Optimization(PSO) [42], Hybrid Ant Colony Optimization (HACO) [38] and HSA optimization are performed to get the best optimal feature set.
4. The optimal feature set is used as input to classifiers. Support Vector Machine (SVM), Decision Tree (DT), Logistic Regression (LR), Linear Discriminant Analysis (LDA), K-Nearest Neighbors (KNN), Ensemble Bagging(EB) based classifiers are employed.
5. The performance of each classifiers coupling GA, PSO, HACO, and HSA are respectively evaluated using six performance measures: sensitivity, specificity, accuracy, F-measure, precision and ROC curve.

To make the quantitative evaluation of the classification performance of the proposed method, we compared the classification results with five performance measures: sensitivity, specificity accuracy, F-measure, and precision. The performance measures are obtained based on the combination of different classifiers and feature selections as tabulated in Table 2.5, Table 2.6, Table 2.7, and Table 2.8 respectively. The performance measures also evaluated using ROC curves as illustrated in Figure 2.8 (a), (b), (c), and (d) respectively for the combination of each classifiers coupling GA, PSO, HACO, and HAS. The Area Under ROC curve (AUROC) is presented in Table 2.9. The experimental results in Table.2.5-Table 2.8 show that HSA coupling with EB achieved the best accuracy compared to other coupling pairs in this study as well as compared to the related works in the literature as given in Table 2.10.

Table 2.5 Classification results based on HSA coupling with different classifiers.

| Classifiers | Sensitivity | Specificity | Accuracy | Precision | F-measure |
|--------------------|--------------------|--------------------|-----------------|------------------|------------------|
| SVM | 89.09 % | 96.75 % | 95.00 % | 89.09 % | 89.09 % |
| DT | 87.27 % | 94.05 % | 92.50 % | 81.35 % | 84.21 % |
| LR | 72.72 % | 94.59 % | 89.58 % | 80.00 % | 76.19 % |
| LDA | 90.90 % | 68.64 % | 73.75 % | 46.29 % | 61.35 % |
| KNN | 85.45 % | 95.13 % | 92.91 % | 83.92 % | 84.68 % |
| EB | 90.90 % | 98.92 % | 97.08 % | 96.15 % | 93.45 % |

Table 2.6 Classification results based on GA coupling with different classifiers.

| Classifiers | Sensitivity | Specificity | Accuracy | Precision | F-measure |
|--------------------|--------------------|--------------------|-----------------|------------------|------------------|
| SVM | 72.72 % | 96.21 % | 90.83 % | 85.10 % | 78.43 % |
| DT | 81.81 % | 97.29 % | 93.75 % | 90.00 % | 85.71 % |
| LR | 47.27 % | 94.05 % | 83.33 % | 70.72 % | 56.52 % |
| LDA | 94.54 % | 65.40 % | 72.08 % | 44.82 % | 60.82 % |
| KNN | 83.63 % | 91.89 % | 90.00 % | 75.41 % | 79.31 % |
| EB | 85.45 % | 97.83 % | 95.00 % | 92.16 % | 88.68 % |

Table 2.7 Classification results based on PSO coupling with different classifiers.

| Classifiers | Sensitivity | Specificity | Accuracy | Precision | F-measure |
|--------------------|--------------------|--------------------|-----------------|------------------|------------------|
| SVM | 90.90 % | 95.13 % | 94.16 % | 84.75 % | 87.72 % |
| DT | 89.09 % | 95.67 % | 94.16 % | 85.96 % | 87.50 % |
| LR | 54.54 % | 96.76 % | 87.08 % | 83.33 % | 65.93 % |
| LDA | 92.72 % | 68.64 % | 74.16 % | 46.79 % | 62.19 % |
| KNN | 90.90 % | 94.40 % | 93.33 % | 81.97 % | 86.20 % |
| EB | 90.90 % | 97.83 % | 96.25 % | 92.59 % | 91.74 % |

Table 2.8 Classification results based on HACO coupling with different classifiers.

| Classifiers | Sensitivity | Specificity | Accuracy | Precision | F-measure |
|--------------------|--------------------|--------------------|-----------------|------------------|------------------|
| SVM | 85.45 % | 95.13 % | 92.92 % | 83.93 % | 84.68 % |
| DT | 80.00 % | 96.21 % | 92.50 % | 86.27 % | 83.02 % |
| LR | 58.18 % | 95.13 % | 86.67 % | 78.05 % | 66.67 % |
| LDA | 90.90 % | 68.65 % | 73.75 % | 46.29 % | 61.35 % |
| KNN | 90.90 % | 94.05 % | 93.33 % | 81.97 % | 86.20 % |
| EB | 90.90 % | 96.75 % | 95.42 % | 89.28 % | 90.90 % |

Table 2.9 AUROC for different pairs of feature selection and classifiers.

| Classifiers | AUROC | | | |
|-------------|---------------|----------------|----------------|----------------|
| | HSA | GA | PSO | HACO |
| DT | 93.40 % | 89.11 % | 92.06 % | 90.57 % |
| SVM | 98.15 % | 95.25 % | 97.91 % | 94.94 % |
| LR | 94.75 % | 89.34 % | 94.07 % | 91.62 % |
| LDA | 87.79 % | 89.29 % | 87.37 % | 87.53 % |
| KNN | 97.87 % | 95.00 % | 97.31 % | 97.86 % |
| EB | 98.34% | 97.31 % | 97.93 % | 97.79 % |

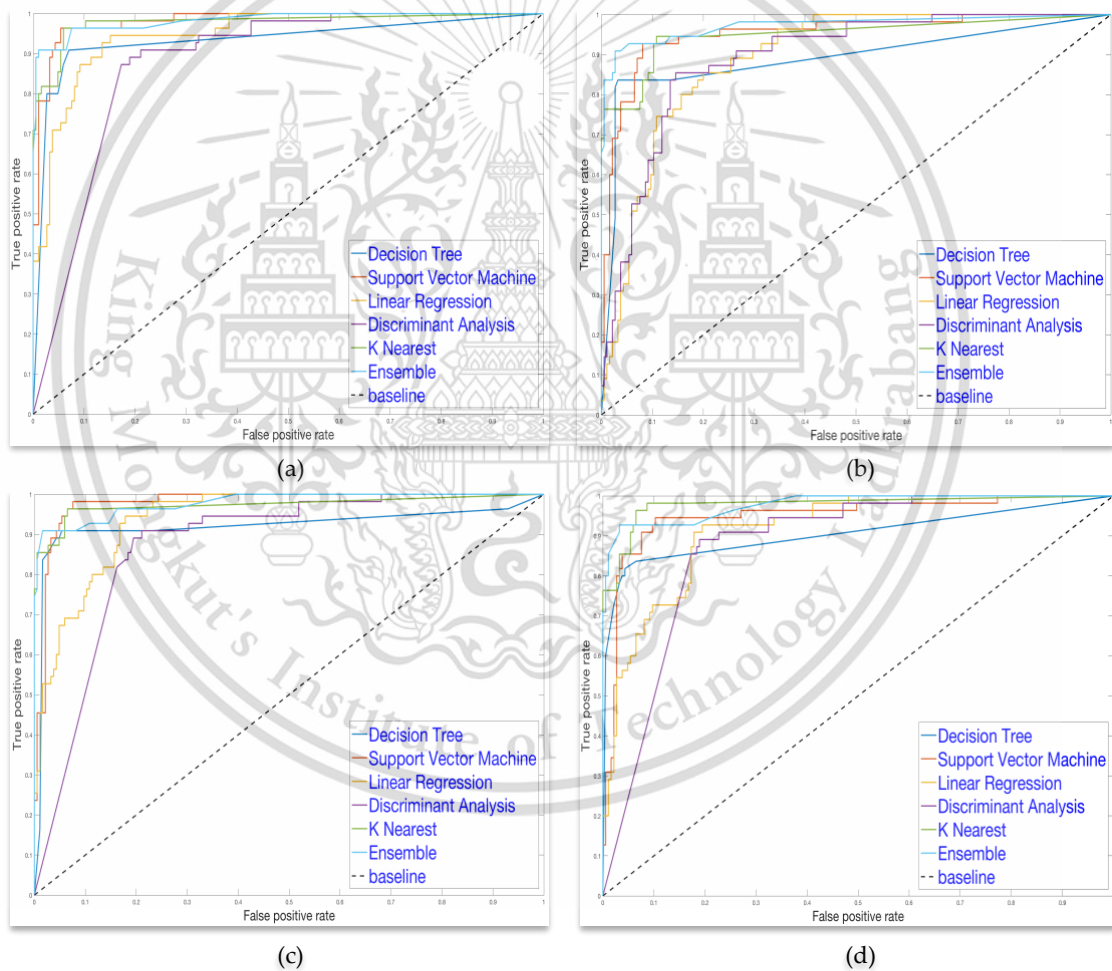


Figure 2.8 ROC curves of each classifiers coupling with (a) HSA, (b) GA, (c) PSO and (d) HACO.

Table 2.10 Comparison of the proposed method with previous works.

| Authors | No. of images | Methods/Input features/Classifiers | Performance |
|--------------------------|----------------------|--|---|
| Goh et al 2009 [21] | 1000 | <ul style="list-style-type: none"> -Features of the sub-images locally -Features extraction using 9 different sets of features -Multiple classifiers | Sen = 92.00 % Sp= 91.00 % |
| Imani et al. 2015 [20] | 930 | <ul style="list-style-type: none"> -Morphological Component Analysis -Features extraction using statistical features -Support vector machine | Acc= 92.82 % Sen = 92.01 % Sp= 95.45 % |
| Kumar et al. 2016 [17] | 1344 | <ul style="list-style-type: none"> -Intensity transformation and multi-level histogram analysis -A waterfall model based classification approach | Sen= 80 % Sp=50 % |
| Acharya et al. 2016 [15] | 800 | <ul style="list-style-type: none"> -Bi-dimensional empirical mode decomposition(BEMD) -Features extraction using 2D Intrinsic Mode Functions and residue -Feature raking -Support vector machine | Acc =88.63 % Sen= 86.25% SP=91% |
| Koh et al. 2017 [16] | 1486 | <ul style="list-style-type: none"> -2-D Continuous Wavelet Transform (2D-CWT) -Features extraction using scalogram images of 2D-CWT -Synthetic data using ADASYN -Particle swarm optimization -Random forest classifier | Sen= 89.37% SP=95.58% Acc =92.48 % |
| Proposed method | 1200 | <ul style="list-style-type: none"> -Kirsch edge detection and morphological operation -Features extraction using eight feature extractors -Hybrid simulated annealing -Ensemble bagging classifier | Sen=90.90% Sp=98.92% Acc=97.08% Pre=96.15% F=93.45% AUC=98.34% |

2.4 Discussion

An automatic screening system of DR is essential and a difficult task for computer-aided diagnosis systems due to the uneven illumination inside the image caused by the process of image acquisition and the main focus of retinal analysis (nasal view or macula view). In this study, we proposed a framework (see Figure 2.3) that differentiate DR and Non-DR automatically using fundus images. The proposed method comprises five processing steps:

Image preprocessing is applied to standardize the image size and improve the retinal image quality. Then DR lesions are segmented using Kirsch edges detection and morphological top hat. Post-processing is further applied to eliminate any remaining noise caused poor image quality. After the DR lesions are segmented, the healthy retinal and DR images are differentiated based on the pixel density of the binary image (see in Figure 2.5(e)) and the information of texture, color, and intensity of the detected regions (see in Figure 2.5(f)), in which 8 feature sets with a total of 208 features are extracted. Directly using all features from feature extraction may include the irrelevant features, which cause heavy computation time, redundancy, and even reduce predictive performance.

To deal with this problem, we studied and compared the performance of four famous feature selection methods namely GA, PSO, HSA and HACO to select the optimal feature set as the input to the classifiers. Since the input data set is unbalance (960 DR images and only 240 non-DR images), an EB based classifier is selected. To evaluate the performance of EB classifier, GA, PSO, HAS and HACO coupling with SVM, DT, LR, LDA, KNN and EB based classifiers are employed as reported in Table 4.5-4.8 and the AUROC as depicted in Table 4.9. To evaluate the performance of the

proposed method, five performance measures are compared using: sensitivity, specificity, accuracy, F-measure, and precision. As presented in Table 4.10, our methods give better results by comparing to the conventional methods because we carefully investigate and experiment throughout each step of the process.

2.5 Summary

This chapter presents an automated DR screening system for quantitative analysis of retinal images. Firstly, during the image segmentation step, all possible candidate lesions of DR are segmented using Kirsch edges detection and morphological top hat. The proposed method uses eight feature extractors to extract a total of 208 features based on the density of the pixels, texture, color, and intensity of the segmented lesions. A hybrid feature selection algorithm based on simulated annealing is utilized to select the optimal feature set as the input to ensemble bagging classifier. The proposed method is evaluated using a dataset containing 1200 images and achieves an accuracy of 97.08%, a sensitivity of 90.90%, a specificity of 98.92%, a precision of 96.15%, an F-measure of 93.45% and an AUROC of 98.34 %. The classification results also reveal that the optimal feature set obtained through a hybrid simulated annealing algorithm can significantly discriminate between healthy and DR retinal images and has better performance compared to previous methods and other metaheuristic based hybrid feature selection algorithms. In future, we will further extend our research to grade the severity of DR.

CHAPTER 3

RED LESIONS DETECTION IN DIABETIC RETINOPATHY USING IMAGE SEGMENTATION

The associated lesions of DR including microaneurysms and hemorrhages known as red lesions, and hard exudates and cotton wool spots known as bright lesions. In the chapter, the detail of microaneurysms and hemorrhages detection using image segmentation level are described in sections 3.1 and 3.2 respectively.

3.1 Microaneurysms Detection Using Image Segmentation

Microaneurysms are the first visible sign of DR pathologies, thus it is essential to detect the lesions in an early state and cue it on time to protect the vision of the patients. In the clinical environment, the poor quality retinal images remain the problem to segment the objects of interest from the background. Recently, there have been many studies proposed methods for detecting the lesions of DR. In the literature, detection of microaneurysms have been reported with different categories. They are including morphological operation base using the size, pixel range, and shape of MAs [43-44]. The color-based segmentation method as defined in [45] was used to filter the MAs using average values of the HSV color model and then the area and eccentricity methods were applied to separate the MAs area with the noise. Eigenvalue base analysis for MAs detect using the Hessian matrix was presented in [46]. In [47], machine learning approaches for MAs candidate classification using supervised learning method was applied to train 21 images based on kernel density estimation. The integration of different morphological operations and support vector machines were applied to

identify MA candidates as reported in [48]. The same support vector machine method was applied in [49] after removing the blood vessels using top-hat transformation and morphological operation. In [50], the proper threshold value was selected first, then the optic disc area and blood vessels were eliminated by applying morphological operation. Finally, the MA candidates were classified by support vector machine algorithm.

The above-proposed methods seem complicated and take time to proceed. In this study, we proposed a simple method to identify MAs using image segmentation techniques as reported in Figure 3.1. Firstly, we enhanced the image quality. Then we applied Canny edges detection and maximum entropy thresholding to segment MA candidates. Based on the appearance of microaneurysms which appear as small red dots and circular shape we applied area and eccentricity methods to discriminate them from the other lesions and the anatomical structures of the fundus image. Finally, the morphological operation was applied to mark out these symptoms.

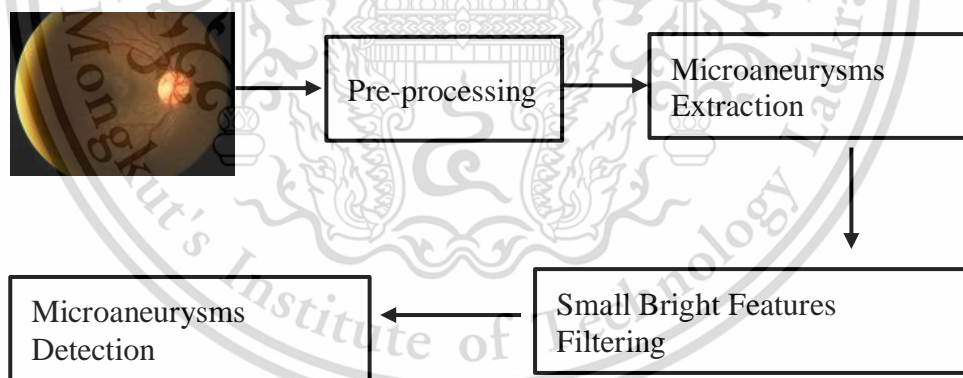


Figure 3.1 Block diagram for microaneurysms detection.

3.1.1 Image Preprocessing

The bad contrast, illumination, and color inside the fundus images are very complicated in the detection of MAs. Preprocessing step is the first and important step

to solve these problems. Firstly, we resized the image to smaller size (576 x 720 pixels) to standardize the image size and reduce time complexity. Then principal component analysis based conversion for gray conversion in the LAB color space was selected (f_{pca} image). After that, f_{pca} image is further complemented to reverse the intensity values for the desired lesions become easier in thresholding step. Finally, the inverse discrete 2D wavelet transforms and medians filter were applied to remove noise and improve the quality of the image. The resulted images in the preprocessing step can be defined as in Eq.1 and illustrated in Figure 3.2.

$$f_B = C_{f_{pca}}(IM) \quad (1)$$

where f_B image is resulted from the conversion of f_{pca} image by using Inverse 2D wavelet transforms (I) and Medians filter (M).

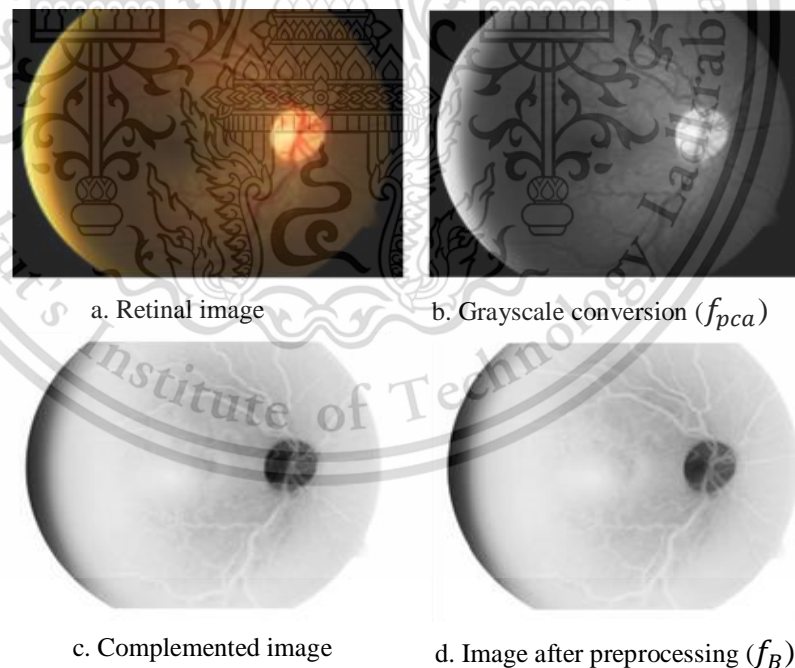


Figure 3.2 The visual results of preprocessing step.

3.1.2 Microaneurysms Extraction

To extract the microaneurysms areas, we proposed a framework as illustrated in Figure 3.3. Firstly, Canny edges detection is applied to f_B image to track all features which appear with edges inside f_B image with fudge factor α_f as below.

$$f_{canny} = T_{f_B}(\alpha_f) \quad (2)$$

where f_{canny} image is the transformation of f_B image after applying Canny edges detection with the fudge factor $\alpha_f=0.5$.

As seen in f_{canny} image (Figure. 3.3 (a)), the microaneurysms areas can be defined as closed curve. So, to identify the lesion areas, we filled all the holes as explicated in Eq. 3 and showed in Figure 3.3 (b).

$$f_H = imfill(f_{canny}, 'hole') \quad (3)$$

where f_H image is the resulted image of filling the holes in the f_{canny} image.

To mark out all MAs areas, the subtraction operation is applied by subtracting the f_{canny} image from the f_H image.

$$f_L = f_H - f_{canny} \quad (4)$$

where f_L image (see in Figure 2.3 (c)) is the resulted image from subtracting the f_{canny} image from the f_H image.

MAs can be defined as red dots with the round shape and a diameter $\lambda < 125\mu\text{m}$ [51]. With this information, the area and shape of MAs are both considered. The area of MAs can be found in the range of pixels from 7 to 15 in an image of 576 x 720 pixels.

After that, the group of pixels with the pixels' range from 7 to 15 are defined by area method.

$$f_A = R_{f_L}(Area) \quad (5)$$

where f_A image is the resulted image from removing all group of pixels which are out of range from 7 to 15 from f_L image.

Finally, the shape of MAs can be found by eccentricity method with the values from 0.8 to 1. The value of eccentricity is range from 0 (line) to 1 (circle).

$$f_{AU} = R_{f_A}(Ecc) \quad (6)$$

where f_{AU} image is the resulted image from removing all group of pixels with the values of eccentricity are out of range from 0.8 to 1 from f_A image.

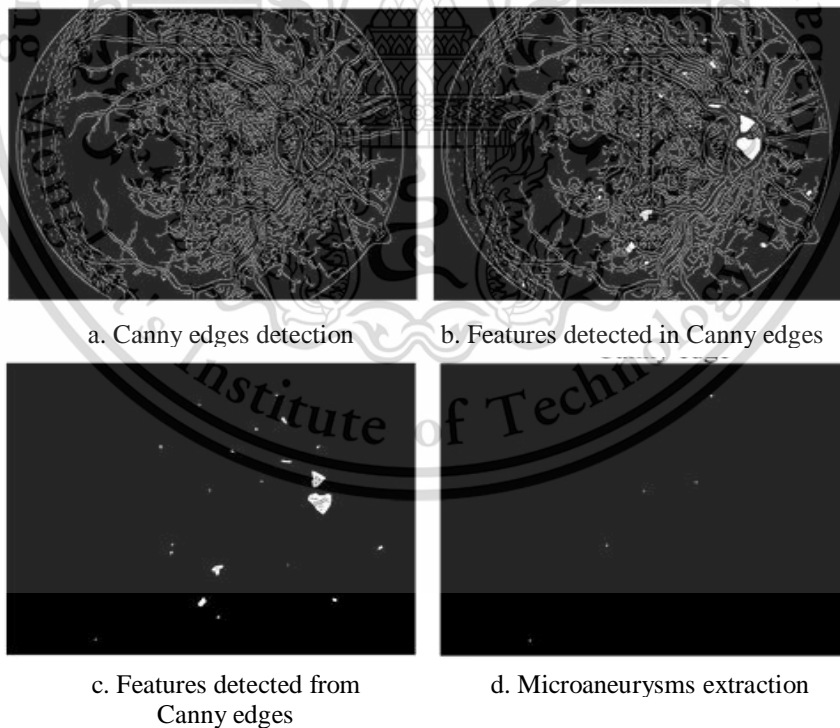


Figure 3.3 Microaneurysms extraction processes.

3.1.3 Small Bright Features Filtering

To detect bright objects, in the preprocessing, the green channel in RGB color model (f_g image) is first selected, and then we apply contrast-limited adaptive histogram equalization to improve the contrast. After that, median filter is used to reduce noise.

$$f_c = C_{f_g}(CM) \quad (7)$$

where f_c image is the conversion of f_g image by using Contrast-limited adaptive histogram equalization (C) and Medians filter (M).

To define both low and high levels of bright features without effecting the background in retinal image, double thresholding of maximum entropy thresholding [52] are applied. The first step is used to define the high level of bright features, and then use this resulted image to eliminate them out from f_c image. The f_{high} image is obtained after this process. Next, the second step of maximum entropy thresholding is applied to f_{high} image to define the low level of bright features again for elimination from the f_{high} image.

$$f_{two} = E_{f_g}(2L) \quad (8)$$

where f_{two} image is obtained after elimination 2 Levels (2L) of bright features from f_{two} image.

After that the resulted image f_{two} is reversed and binaries again to find f_{2L} image which contains both levels of bright lesions and some noises from the background. Finally, the big groups of pixels which are more than 3,000 are removed

out because they are considered as the background of the retinal image. The resulted images for bright features filtering are defined as in Eq. (9) and illustrated in Figure 3.4.

$$f_{bright} = R_{f_{2L}}(BGP) \quad (9)$$

where f_{bright} image is the resulted image from removing all Big Group of Pixels (BGP) from f_{2L} image.

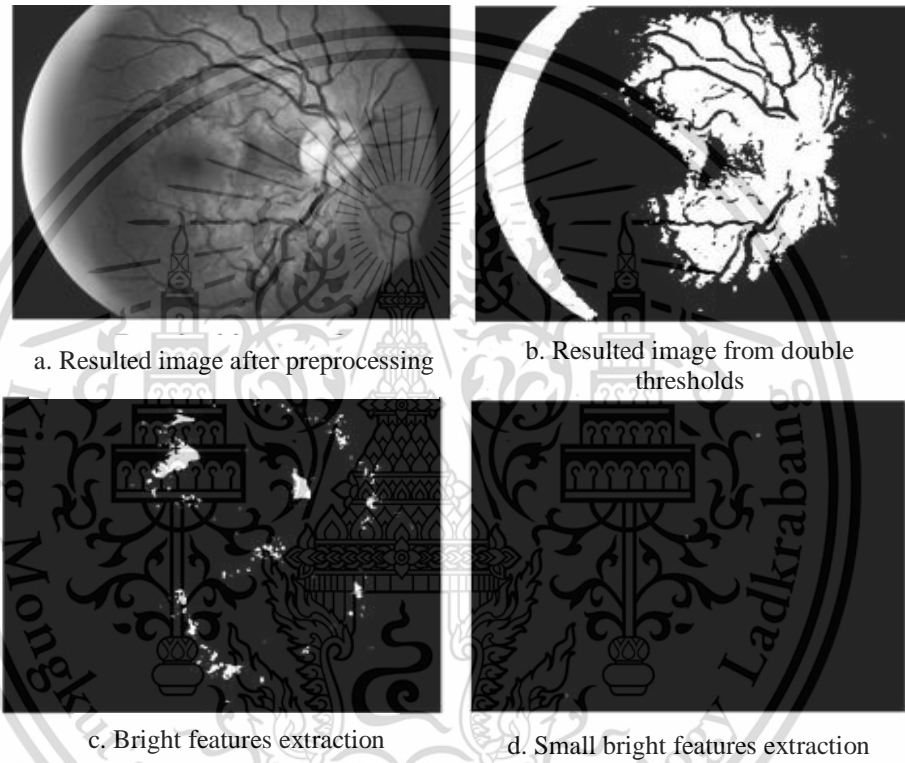


Figure 3.4 Small bright features extraction.

3.1.4 Microaneurysms Detection

After small bright features are detected, we can eliminate these features by subtracting them out from the result of microaneurysms extraction as shown in Eq. (10).

$$f_{MIs-mask} = f_{all} - f_{s-bright} \quad (10)$$

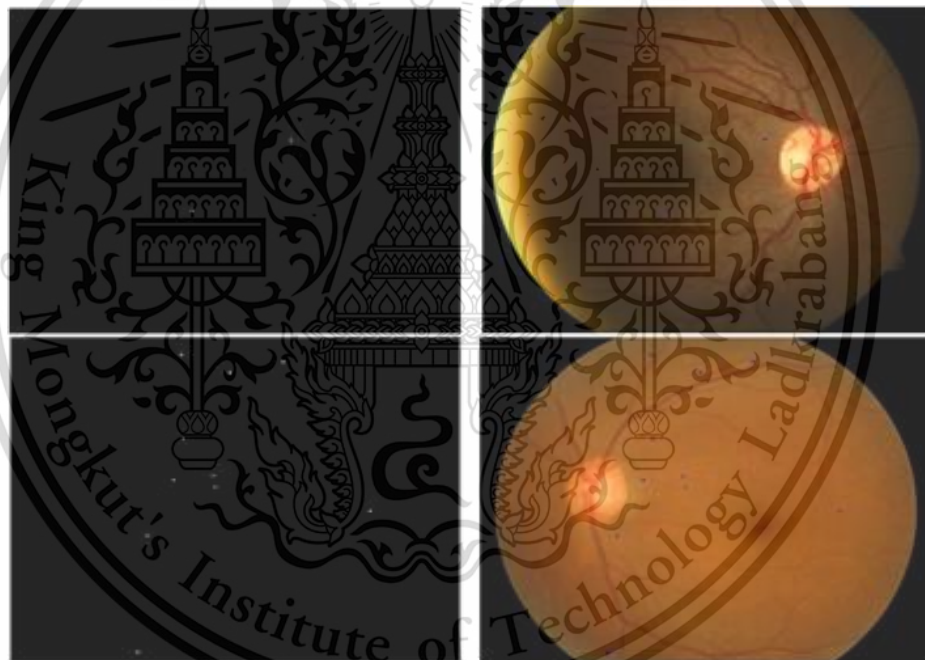
where $f_{MIS-mask}$ image is the resulted image from subtracting the $f_{S-bright}$ image from the f_{all} image.

Finally, we overlaid the resulted $f_{MIS-mask}$ image on the original retinal image to mark out these lesions by using morphological reconstruction.

$$f_{MIs} = R_{f_{Fundus}}(f_{MIS-mask}) \quad (11)$$

where $f_{MIS-mask}$ is the mask image, f_{Fundus} is the original image, and f_{MIs} image is the result of MAs detection.

Figure 3.5 illustrates the result of microaneurysms detection.



a. Microaneurysms mask detection

b. Marking out microaneurysms lesions on color image

Figure 3.5 Microaneurysms detection.

3.1.5 Experimental Result

The experimental result was evaluated using local and DIARETDB1 datasets containing 668 fundus images with image resolution varies from 1500 x 1152 pixels (DIARETDB1) to 3872 x 2592 pixels (local database) in 24 bit PNG and JPEG format. These images contain all lesions related to DR (microaneurysms, hemorrhages, cotton-wool spots, exudate, etc.) and healthy images.

The performance of the result was evaluated by an ophthalmologist for all testing images. The ophthalmologist verifies the detection results for all test image sets based on the values of sensitivity and specificity. The accuracy is the overall correctness of the system and is calculated as the sum of correct classifications divided by the total number of classifications. The evaluated results indicated that 90% of accuracy was successfully obtained for the detection of microaneurysms with the average time complexity 9.53 seconds per image by using a laptop with Intel Dual core CPU and Ram 2 GB.

3.2 Automatic Hemorrhages Detection Based on Fundus Images

The associated pathologies of DR include MAs, HEs, CWSs and EXs. HEs is the developing symptoms from MAs. They appear as red structures of variable shape; dot round, a flame, and blot shapes in the retinal image.

Numerous methods have been developed to assist the experts for primary DR screening system. In the literature, HEs detection algorithms have been roughly divided into different categories using thresholding, image segmentation, morphology operation, classification, clustering, and so on. Nutnaree et al. [53] used morphological top hat and image binarization techniques to filter the hemorrhage areas and then

applied blob analysis and rule-based classification to discriminate them from various lesions and anatomical structure of the retina (blood vessels and fovea). Sharath et al. [54] reported the method to detect red lesions in the retinal image based on two processing phases. Firstly, they modified the method from Spencer et al. [55] to segment all visible red regions. Since the obtained result contains not only the red lesions but also the non-red lesions which were considered as noises, the second phase was applied to remove them out. They are including blood vessels and non-red lesions in the optic disc and somewhere else in the retinal image. Vijay et al. [56] presented an algorithm to detect red lesions in the retinal image using three processing stages. Firstly, modified matched filtering was applied to enhance the blood vessels and then they extracted all candidate lesions using morphological operation. Finally, all red lesions were classified using support vector machine. Maria et al. [57] investigated an algorithm to classify the red lesions use multilayer perceptron neural network to discriminate the areas of red lesions from the background and other noises.

As mentioned in the above-studies in the literature, most researchers did not focus on the time complexity which is essential for the real application in the hospital. In this chapter, we developed an algorithm which focus on the time complexity to detect HEs using its characteristics by step down elimination un-HEs as illustrated in Figure 3.6. Preprocessing step is the first and essential step to enhance the image quality then all visible red objects are extracted using morphological top-hat. They are including HEs, blood vessels, fovea, and microaneurysms. Since our target is to filter only the HEs areas, we apply morphological operation and compactness measurement to remove the blood vessels and fovea respectively. Finally, HEs can be detected after removing the MAs and some small noise.

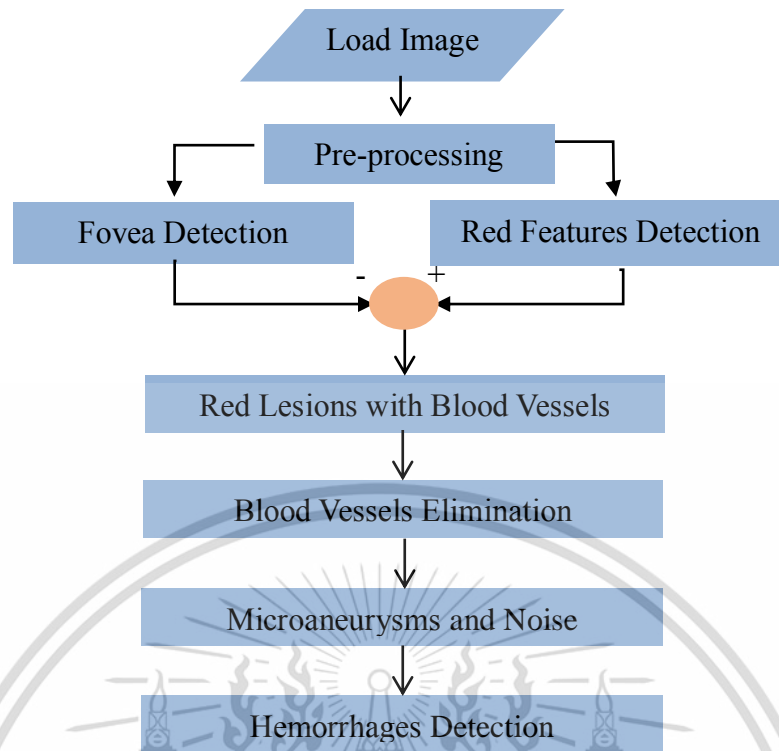


Figure 3.6 Block diagram for hemorrhages detection.

3.2.1 Image Preprocessing

The color, illumination, and contrast inside the retinal images still remain the problem in the research works related to the retinal image analysis especially in the detection of HEs. Preprocessing step is the first and essential step to enhance the image quality so that the image features become easier to be detected by the automated image analysis system. Firstly, we standardize the image size by resizing the image to a smaller size (576 x 720 pixels). By doing so we also can reduce the time complexity. Then median filtering and contrast-limited adaptive histogram equalization are applied respectively on the green channel to remove noise and enhance the image quality. After that, we complement the image to reverse the intensity values for the desired lesions become easier in the binarization step. f_e image is obtained from this preprocessing step which is shown in Figure 3.7.

$$f_e = C_{f_{ori}}(P) \quad (12)$$

where f_e image is the resulted image from the conversion of the original fundus image f_{ori} using preprocessing.

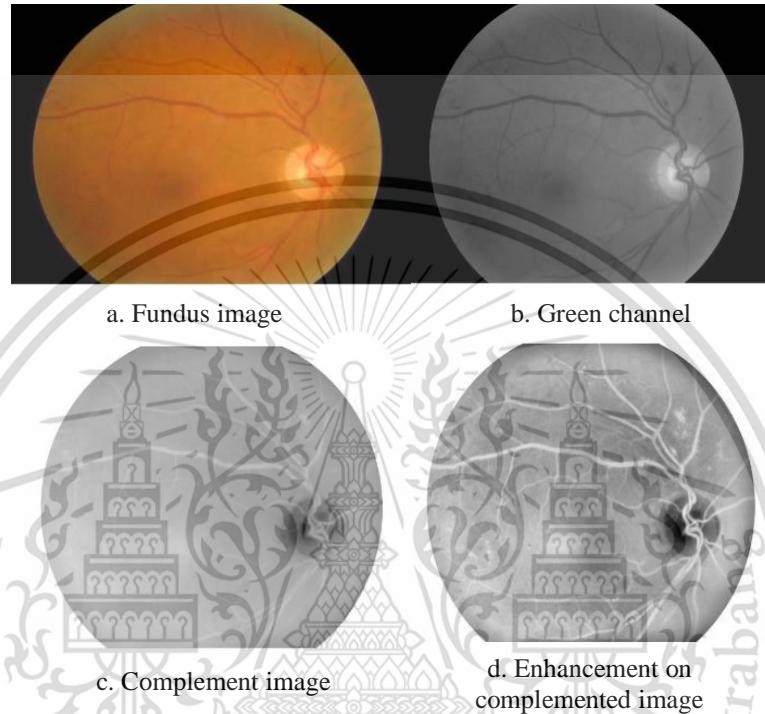


Figure 3.7 Preprocessing step for hemorrhages detection.

3.2.2 Red Feature Detection

After the preprocessing step, the background image needs to be removed to filter out only the interesting points known as red regions. As illustrated in Figure 3.8, firstly we detect the background of the image using morphological opening. The opening operation is applied to remove objects which do not contain the structuring element. The ‘strel’ function in MATLAB is used to create a disk-shaped structuring element with a radius of 15. The radius value is selected as the median value for all fundus

images. Then the background image is removed after subtracting from the enhancement f_e image.

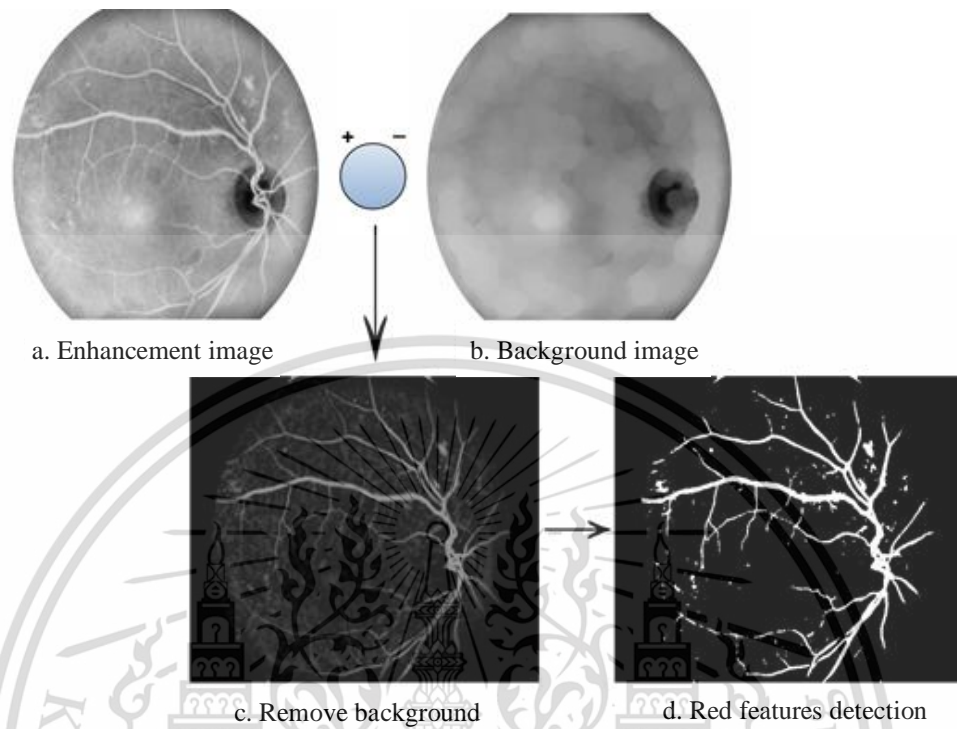


Figure 3.8 Red features detection.

Suppose the background image is f_b , thus the background removal image is defined as:

$$f_r = f_e - f_b \quad (13)$$

where f_r image is the background removal image (see in Figure 2.8 (c)).

Finally, the red features detection image is defined after applying Otsu thresholding [30] to the f_r image.

$$f_{Rf} = C_{f_r}(O) \quad (14)$$

where f_{Rf} image (see in Figure 2.8 (d)) is the resulted image from the conversion of the f_r image by using Otsu's thresholding.

3.2.3 Fovea Detection

The fovea is one of the anatomical structure of the retina whose color is similar to the color of MAs and HEs. To prevent the interferences from the results of HEs detection it is recommended to remove.

To detect the fovea area, we propose three processing stages. The fundus image is first preprocessed to enhance fovea region by applying respectively histogram equalization and contrast-limited adaptive histogram equalization on the green channel of retinal image. f_{Ge} image received from this first step. Then f_{Ge} image is complemented to make desired features become easier in converting to binary image. For the binary conversion step, maximum entropy thresholding method [52] is applied to separate the foreground from its background. After binarization, the resulted f_{binary} image contains not only the region of the fovea so we classify its features based on the size and shape as demonstrated in Figure 3.9. We remove all regions with pixels less than eight hundred because they are not in the size range of fovea. To identify the fovea shape, compactness measure is applied by using the following equation.

$$C(\mathcal{R}) = \frac{4\pi A(\mathcal{R})}{l_p^2(\mathcal{R})} \quad (15)$$

where \mathcal{R} are the regions in f_{binary} image. $A(\mathcal{R})$ and $l_p^2(\mathcal{R})$ are respectively the number of pixels and the length of boundary in each region of \mathcal{R} , and $C(\mathcal{R})$ in Figure 23.9 is the result of fovea detection.

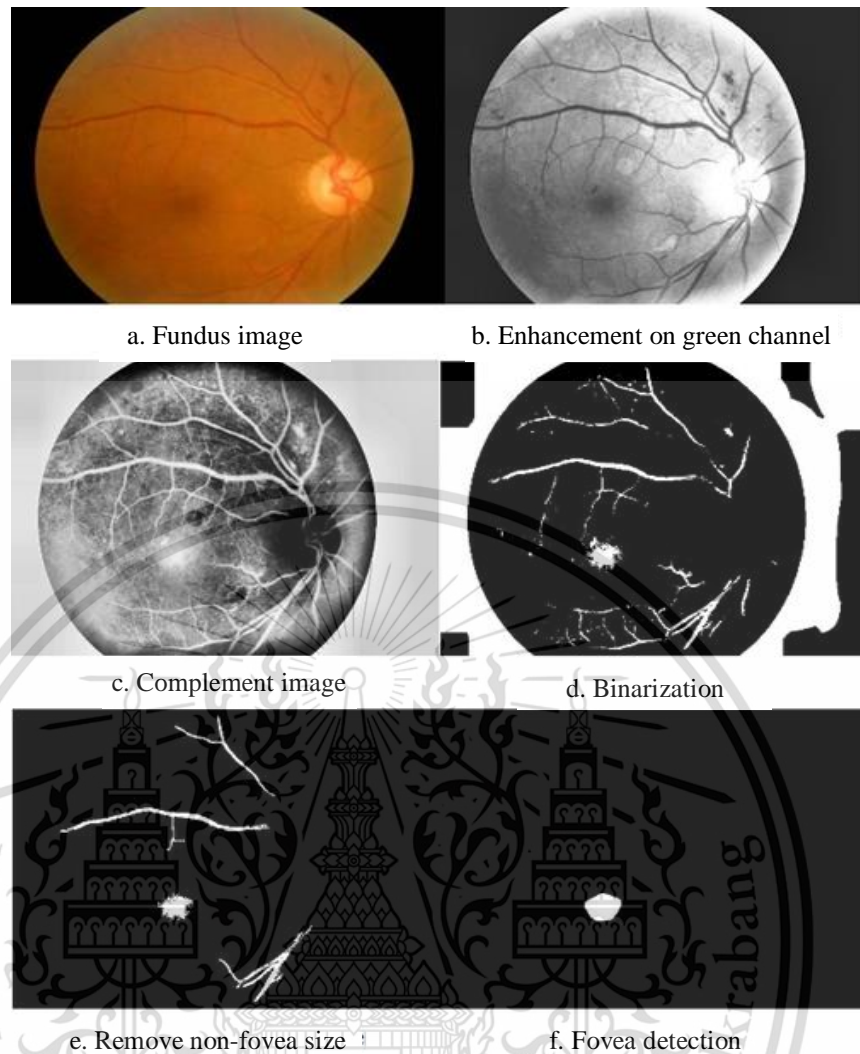


Figure 3.9 The processes of fovea detection.

3.2.4 Blood Vessels Detection

Blood vessels are another anatomical structure of the retina. We need to eliminate them to avoid the interference in the final result of HEs detection. In our study, three processing steps are proposed to detect the blood vessels.

First is the elimination of the fovea region from the result f_{Rf} image. AND-operator between the f_{Rf} image and $f_{C(R)}$ image is applied to find the fovea mask. Then the obtained fovea mask is subtracted from the f_{Rf} image to remove the fovea region.

$$f_{f-mask} = AND(f_{Rf}, f_{C(\mathcal{R})}) \quad (16)$$

$$f_{f-elim} = f_{Rf} - f_{S-mask} \quad (17)$$

where f_{f-mask} image and f_{f-elim} image are respectively the images of fovea mask and fovea elimination. Figure 3.10 shows the process of fovea elimination.

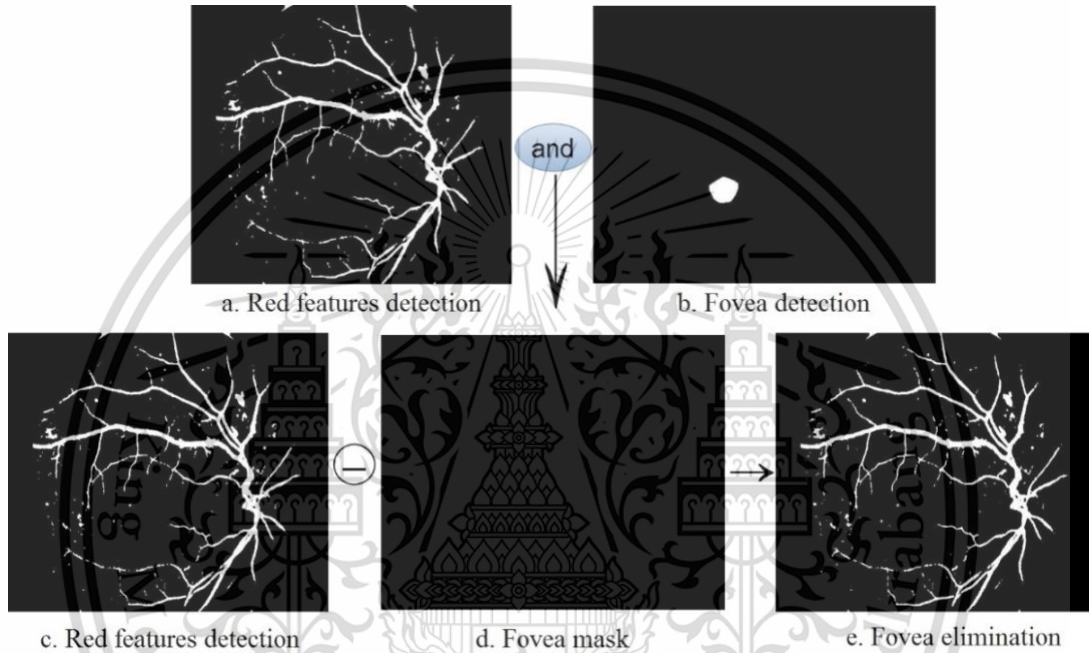


Figure 3.10 The process of fovea elimination.

The next step is short blood vessels (f_{short} image) detection. From the previous process as seen in resulted image f_{f-elim} , some damages cause blood vessels do not connect in one group of pixels so short blood vessels are classified to improve the final result. Since the group of pixels which is more than 500 pixels are identified as long blood vessels (f_{long}), the rest of the group pixels are filtered to identify the shape of short blood vessels. They are in the range of eccentricity value from 0 to 0.8. The value of eccentricity is ranged from 0 (line) to 1 (circle).

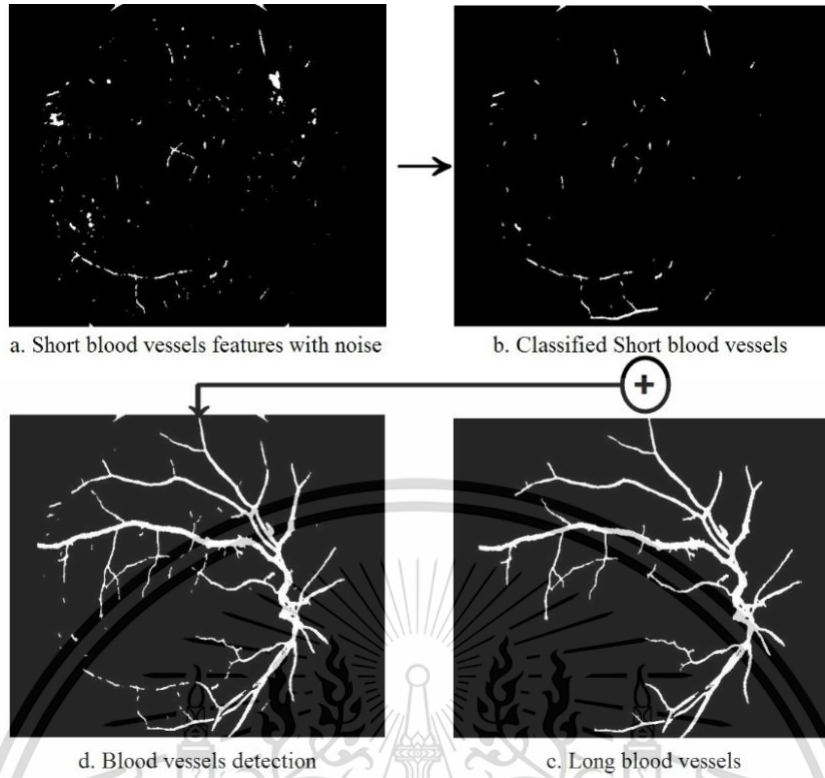


Figure 3.11 Blood vessels detection.

Third is blood vessels detection as shown in Figure 3.11, OR-operator between the f_{short} image and f_{long} images is used.

$$f_{BV} = OR(f_{short}, f_{long}) \quad (18)$$

where f_{BV} image is image of blood vessels detection.

3.2.5 Hemorrhage Detection

After detection f_{BV} image, the subtraction operation is performed between $f_{C(\mathcal{R})}$ image and f_{BV} image to eliminate the blood vessels as shown in the following equation:

$$f_{red} = f_{C(\mathcal{R})} - f_{BV} \quad (19)$$

where f_{red} image is the image of red lesions detection.

Since the f_{red} image contains also MAs and some small noise, therefore the small groups of pixels which are less than 10 pixels are removed because they are considered as the area of MAs and noise. The process of HEs detection is demonstrated in Figure 3.12.

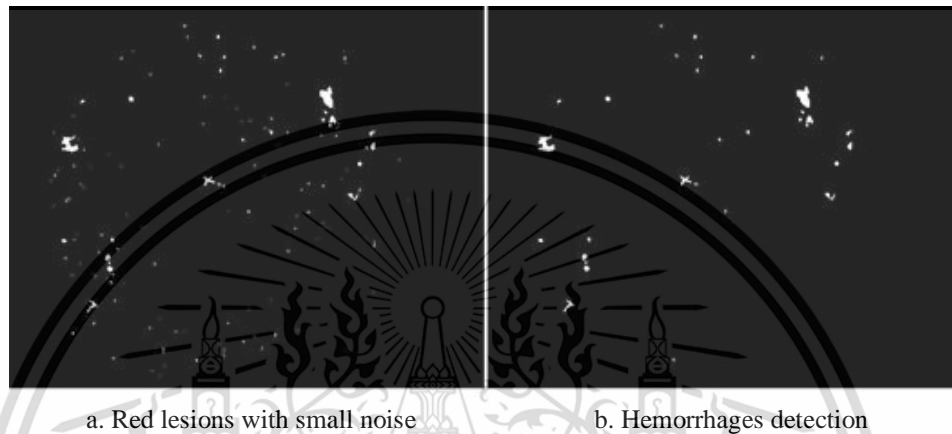


Figure 3.12 Hemorrhages detection

3.2.6 Experimental Result

The experimental result was evaluated using local datasets containing 579 fundus images with image resolution 3872 x 2592 pixels in 24-bit JPEG format from Bhumibol Adulyadej Hospital. These images contain all lesions related to DR (microaneurysms, hemorrhages, cotton-wool spots, exudate, etc.) and healthy images.

In this study, since the ground truth information of lesions is not made, the performance of the result was evaluated by an ophthalmologist for all testing images. The ophthalmologist verifies the detection results for all test image sets based on the values of sensitivity and specificity. Sensitivity is used to measure the proportion of actual positives (HEs) which are correctly identified as HEs. Specificity is used to measure the proportion of negatives (non-HEs) which correctly identified as non-HEs.

The accuracy is the overall correctness of the system and is calculated as the sum of correct classifications divided by the total number of classifications. The evaluated results indicated that 90% of accuracy was successfully obtained for the detection of HEs with the average time complexity of 6.23 seconds per image.

The reason that the proposed method cannot achieve 100% results because of two main points. First, some short blood vessels were not detected in the process of blood vessels detection. Second, the HEs lesions which appear next to the blood vessels were removed with the blood vessels. Thus, the more suitable method should be investigated to be more clearly determined the blood vessels.

3.3 Summary

This chapter proposed a simple method for automated MAs and HEs detection in fundus images. It is a part of DR lesions detection system which is very important to help the ophthalmologists for primary DR screening. To develop the systems for MAs and HEs detections, each lesion was proposed based on their characteristics (MAs and HEs) as mentioned in the above sections. Given a successful rate of 90 % with the average processing time 9.53 seconds and 6.23 seconds per image for MAs and HEs detection respectively, the proposed methods are acceptable for time complexity. However, the proposed methods do not work well with poor quality images. For this reason, we can see that applying only the image segmentation methods is not able to deal with the poor quality retinal images. Therefore, in the future, we need to study more detail about the features of each lesion and extract them as the input for the classification step.

CHAPTER 4

COTTON WOOL SPOTS DETECTION IN DIABETIC RETINOPATHY

As reported in chapter 3, the red lesions including microaneurysms and hemorrhages were described. In this chapter, we will present another lesion known as cotton wool spot using adaptive thresholding and ant colony optimization coupling support vector machine.

4.1 Introduction

Cotton Wool Spots (CWSs) are the critical lesions of diabetic retinopathy, which indicate not only advanced non-proliferative diabetic retinopathy but also pre-proliferative diabetic retinopathy. They are also known as soft exudates which are the result of infarct in the nerve fiber layer and appear as pale white or fluffy patches [58, 59, 60, 61]. CWSs can be discriminated from hard exudates in term of color and sharp edges. Hard exudates are the lipids leakage from the blood vessels or the microaneurysms exuded. By comparing to CWSs, hard exudates appear more yellowish with sharp edges. The present of CWSs in retinal images indicate advancing retinal non-profusion and progressive ischemia. Progressive retinal ischemia is the signal to the development of retinal neovascularization which is one of the most serious cases of PDR and frequently leads to the vision impairment and blindness. Moreover, CWSs are not only associated with DR but also with other diseases, such as hypertensive retinopathy, embolic, ischemic, neoplastic, connective tissue, and infectious diseases. Hence the detection of CWSs is a critical task to grade the severity of DR. By grading

the severity of DR accurately, the eye specialist can make an effective treatment plan to protect the patients' vision against blindness.

In the retinal image, CWSs can appear isolated or with other pathological signs such as hard exudates, microaneurysms or hemorrhages. Optic disc (OD), macula, and blood vessels are normal retinal structures. As shown in Figure 1.5, the color and brightness the OD, hard exudates, and artifacts in surrounding of the OD area easily overwhelm that of CWSs. In addition, in some retinal images; they appear much closer to the background and are not clearly visible. Although various robust and efficient methods have been proposed for the detection of microaneurysms, hemorrhages, and hard exudates, only a few have been proposed for CWSs. CWSs detection and classification remain challenging due to their uneven appearances. Therefore, the efficient CWSs detection system is essential to help the ophthalmologists in accurately grading the severity of DR, and can help to get the efficient treatment plan to protect the patients' vision against blindness. It is a prerequisite to developing a complete computer-aided diagnosis system of detection and grading of DR.

Meindert et al. [62] proposed a system that differentiates CWSs, hard exudates, and drusen using machine learning. 60% of the lesions probability maps were manually selected to extract the bright regions including OD, hard exudates, drusen, and CWSs. Finally, the machine learning algorithm was applied to differentiate three different signs of bright lesions in the retinal image. The results of CWSs detection were reported as 70% for sensitivity and 93% for specificity. Since a fixed thresholding value was used in their proposed system, the failure might happen when dealing with a large number of images.

As with Meindert et al. [62], Clara et al. [63] proposed the classification of three different signs of bright lesions. However, they employed an active learning approach in which Gaussian derivatives are first used to enhance the image, and then 60% of the lesions probability maps are manually selected for segmentation of the CWSs' area after classification of the pixels using a KNN classifier. They obtained the area under ROC curve of 82 %.

Yogesh et al. [64] developed a method to detect CWSs based on multi-resolution analysis using symlet wavelet to extract the lesions of DR. Then, they applied K-means clustering to classify the CWSs. 92 % of accuracy was achieved. However, they did not describe the OD elimination and feature extraction methods clearly.

Toan et al. [65] implemented CWSs detection based on Artificial Neural Network (ANN). Firstly, they removed OD using maximum entropy method from the retinal image. Then the features were extracted from the entire image without OD. Finally, the extracted features were fed as input to ANN to classify. The paper reported 85.54 %, 85.9 % and 84.4% of accuracy, sensitivity, and specificity, respectively. However, their proposed method was analyzed on the entire image instead of on possible CWSs. It might lead to computationally expensive. Segmentation of CWSs areas before main analysis might improve the performance and reduce the computational time.

Samra et al. [66] proposed a system to diagnose CWSs in hypertensive retinopathy in which Gabor filter bank and Gabor thresholding are applied to detect CWSs. In this paper, the classification method was not utilized to reduce the false detected objects. They achieved sensitivity of 82.21% and positive predictive value of

82.38%. Since the detected areas might contain false findings such as exudates or other bright objects, it is essential to discriminate between CWSs and false findings.

Asra et al. [67] proposed a three step-process for extracting CWSs features for malarial retinopathy screening. First, the morphological operation is applied to remove the blood vessels based on the method in [68]. Next, the image is enhanced by Gabor filter bank, and then Otsu's thresholding is applied to extract the CWSs features. Finally, SVM classifier is employed for classification. 82.21 % of sensitivity and 82.38% of positive predictive value were obtained. However, no explanation is given for the features defined as the input for training and testing.

Sohini et al. [69] presented a method to screen DR using machine learning approaches. The best classifiers were studied and selected for bright and red lesions classification. Two hierarchical steps were applied to classifier CWSs and hard exudates. The true bright lesions were discriminated against non-bright lesions in the first step then the true bright lesions were reclassified as hard exudates and CWSs. Adaboost method was applied for feature ranking to select the optimal feature set for classification of hard exudates and CWSs.

Jagatheesh et al. [70] classified DR lesions based on bag of visual words model. The features of DR lesions were first extracted using speeded up robust features then clustered using k-means. After that, the bag of visual words was created based on fisher vector encoding and pooling technique. Finally, SVM was used to classify the normal and lesion regions. The accuracy of 78.23%, sensitivity of 72.15 % and specificity of 79.40% were reported. Besides that, some authors [71-73] attempted to detect the bright lesions, but they have not addressed to differentiate between hard exudates and CWSs.

From the above-mentioned literature, the reliable segmentation of CWSs remains challenging due to the high variability of their appearance. To remedy the aforementioned problems for the segmentation process, we segmented bright regions containing CWSs, OD, and exudates using adaptive thresholding. Numerous approaches of adaptive thresholding segmentation based for retinal images analysis have been proposed for the detection of Blood Vessels (BV), OD, and red lesions in [74-77], [78], and [79] respectively. The BV, both large and thin, in retinal images are unable to segment accurately within a global threshold value [74-77]. Thus, the local thresholding is required. Ghadiri. et al [78] addresses the problem of OD detection based on its location the temporal side and the nasal part. The OD first localized based on the intensity value and the vessel width, then use the information of major vessels originating from OD to separate OD area into two parts. Finally, adaptive thresholding was applied to segment the OD area. Shaunak et al. [79] proposed a method to detect red lesions using the estimating of the upper threshold and the lower threshold based on the local image information individually in the retinal image.

After all possible CWSs regions are segmented, classification is implemented to differentiate between CWSs and non-CWSs. Features and classification algorithms are the most important aspects to obtain the high classification performance. In the literature, most of the extracted features are morphological and texture features. Most classification algorithms employed in the literature revolve around k-mean clustering, fuzzy c-mean, artificial neural network and support vector machine. All related works in the literature mentioned above utilized all extracted features to classify CWSs whether it has the significant difference between CWSs and non-CWSs or not. Directly

using all features for classification may cause time complexity, redundancy, and poor generalization capacity.

In order to handle the above-mentioned problems, we do feature selection prior to the classification. Ant Colony Optimization (ACO) method is proposed to select the optimal feature set. ACO is one of the famous features selection methods, that is inspired by the ant's social behavior in their search for the shortest paths between food sources and their nests [80]. ACO was first applied to solve difficult optimization problems such as travelling salesman problem and quadratic assignment problem. ACO has been attractive for features selection in medical image analysis. In medical image analysis, ACO based feature selection method include lymph node classification [81], hippocampus segmentation [82], and bronchitis diagnosis from CT images [83], etc. In retinal image analysis, ACO was applied in retinal vessel detection [84] and exudates detection [85].

In this thesis, an automatic CWSs detection and classification method is proposed. First, the image is preprocessed to enhance the retinal image. Then adaptive thresholding is applied to segment all possible CWSs regions. In order to remove the noises and artifacts surrounding of the OD, the location of OD is firstly detected based on our previous study [30], the diameter of detected OD is measured to construct the rectangular mask, and then the rectangular mask is used to cover OD area. For the classification of CWSs, 162 features based on morphologies, first order statistics, Gray Level Co-occurrence Matrix (GLCM), Gray Level Run Length Matrix (GLRLM) and lacunarity are extracted. After that, ACO is applied to obtain the optimal features set. Finally, the selected features are used as input to cubic SVM classifier.

The remainder of this chapter is managed as follows. Section 4.2 outlines our proposed methodology. Section 4.3 presents experimental results and discussions. Section 4.4 presents concluding remarks.

4.2 Materials and Methods

4.2.1 Datasets and Ground Truth

Currently, online databases with ground truth are very important in helping researchers compare the performance of different methods in medical imaging. Ensuring that the results of automated extraction of pathological signs correspond to the results obtained by experts is essential. Ground truth annotation is prepared first by computer vision researchers and is used by medical experts to select and annotate pathological signs [86]. This collaboration work creates ground truth images for computer-aided diagnosis systems. As an example, one of the ground truth image for CWSs from DIARETDB1 is shown in Figure 4.1.

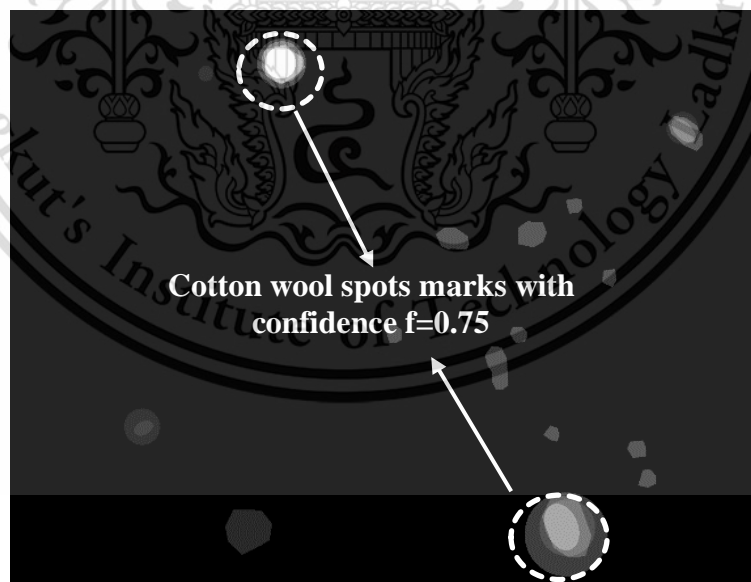


Figure 4.1 Ground truth image for CWSs from DIARETDB1.

Table 4.1 Specifications of datasets used in this study.

| Datasets | No. of Images | Pathological signs of retinal images | | Images with CWSs | No. of CWSs | No. of Non_CWSs |
|----------------|---------------|--------------------------------------|-----|------------------|-------------|-----------------|
| | | Normal | DR | | | |
| DIARETDB 1[87] | 89 | Normal | 5 | 13 | 25 | 487 |
| | | DR | 84 | | | |
| HRF [88] | 30 | Normal | 15 | 1 | 7 | 14 |
| | | DR | 15 | | | |
| Local Dataset | 200 | Normal | 100 | 30 | 198 | 1241 |
| | | DR | 100 | | | |

We evaluated this work based on two available online datasets, DIARETDB1 with the images resolution of 1500 x 1152 pixels in 24 bit PNG format and HRF with the resolution of 3504 x 2336 pixels in 24-bit JPEG format. Besides the online datasets, we build a local dataset contained 200 images with the resolution of 3872 x 2592 pixels in 24-bit JPEG format. Therefore, the study is based on a total of 319 retinal images from three combined datasets. The specifications of the datasets used in the study are described in Table 4.1. Our proposed automated system for detecting CWSs is presented in Figure 4.2.

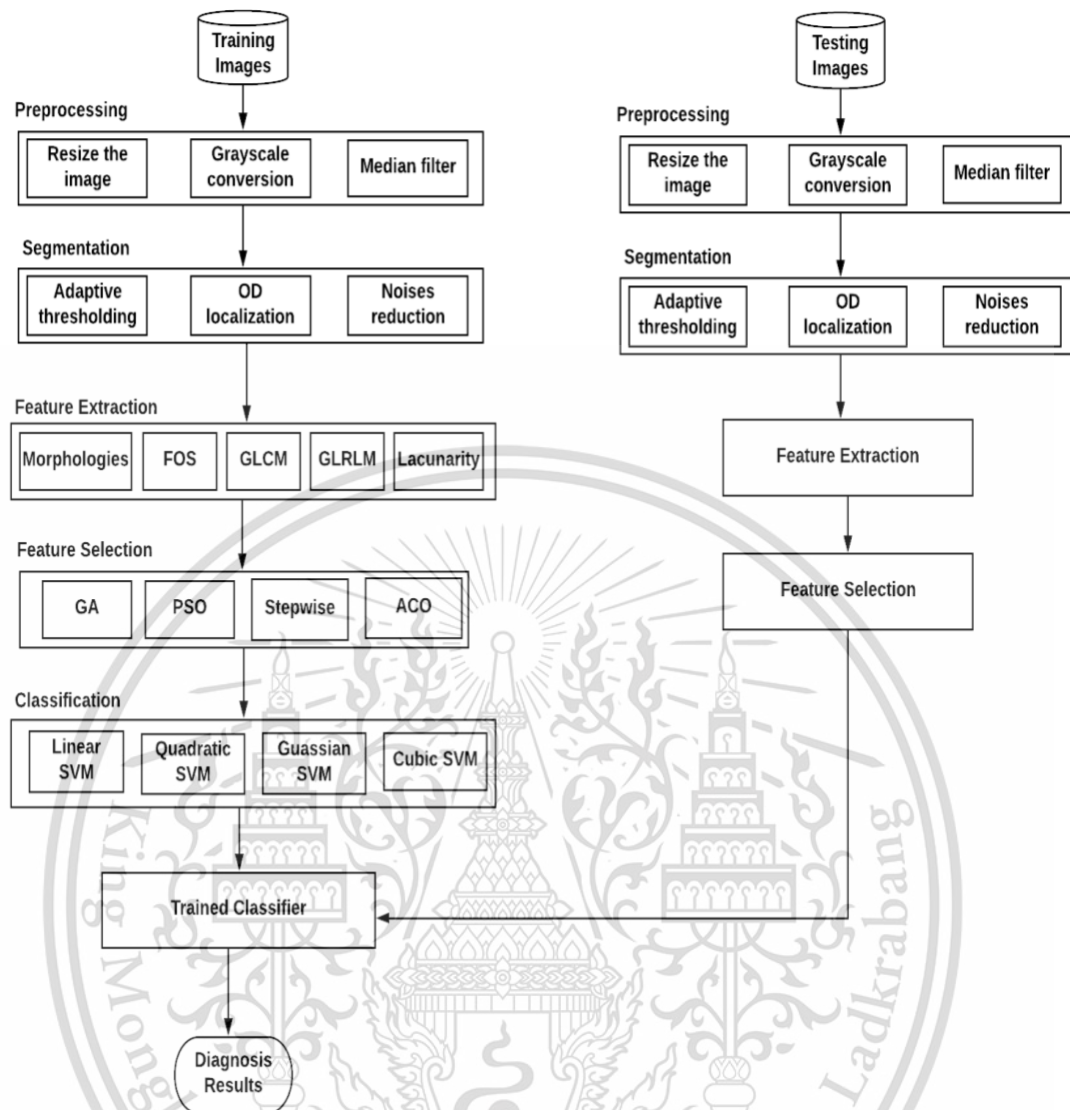


Figure 4.2 Block diagram depicting the proposed system.

4.2.2 Image Preprocessing

Image acquisition in retinal image mainly focuses on the OD area (nasal view) and macular area (macular view) [89]. In DIARETDB1, HRF and local datasets, the captured images mainly focuses on the macular area, which makes the illumination high at the macular area and makes the pixels at the outer ring of the image saturated [90]. There might be the cause of image quality degradation and the presence of artefacts or noises during the process of image acquisition. Image preprocessing step is an essential

step to improve the image quality. Firstly, the image is standardized by resizing the image to 576 x 720 pixels and the green channel of RGB color space is selected due to its good contrast. Then the image enhancement and noises filtering are considered to enhance the contrast of the image and remove the noises, respectively. Since there are various filtering and enhancement methods, the most suitable ones are selected based on the Image Quality Measurement Metrics (IQMM) [91]. The higher IQMM indicates the better quality. For filtering the noises, we employed five famous filters namely Gaussian filter, Laplacian filter, Wiener filter, mean filter and median filter, and computed Peak Signal-to-Noise Ratio (PSNR) which is an IQMM. Median filter is selected to remove the noises because it indicated the highest PSNR value as shown in Figure 4.3 (a). Similarly, the Contrast Improvement Index (CII) of three enhancement methods including intensity adjustment, histogram equalization, and contrast limited adaptive histogram equalization were computed to select the most suitable one. As shown in Figure 4.3 (b), intensity adjustment obtained the highest CII.

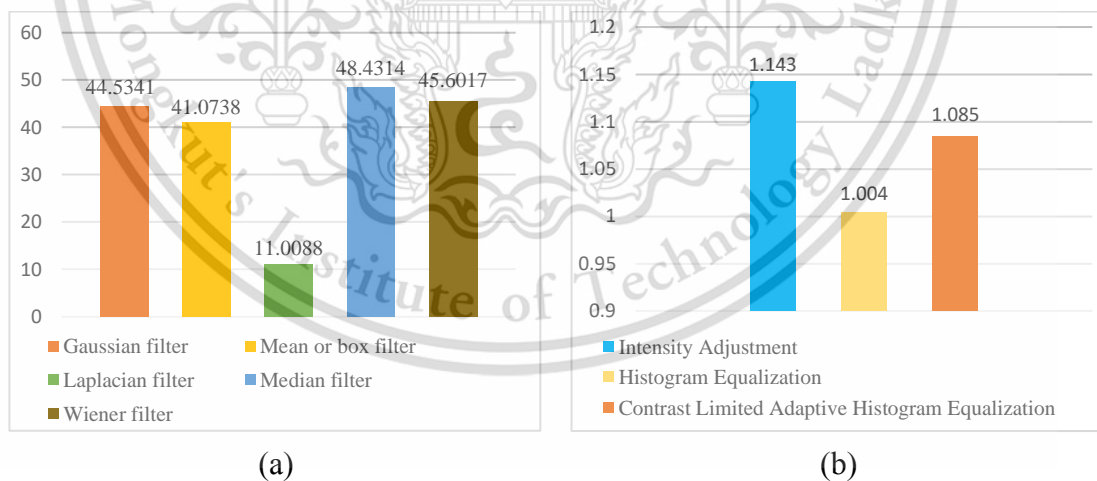


Figure 4.3 IQMM for the image quality improvement: (a) PSNR values of five filtering methods and (b) CII values of image enhancement methods.

4.2.3 Image Segmentation

Image segmentation is one of the main processing steps in image processing techniques [92]. Several methods have been proposed to segment images based on attributes such as intensity, color, and texture. Thresholding is a useful image segmentation method and is frequently employed in medical imaging. It can be further classified into local thresholding and global thresholding. In this study, we experimented with four famous thresholding methods to segment CWSs areas: global thresholding (specifically, Otsu's thresholding, polynomial thresholding, and maximum entropy thresholding) and local adaptive thresholding. Global thresholding can extract some bright objects in the retinal image (exudates and OD). Global thresholding methods fail to detect CWSs areas because global thresholding uses only one optimal value for all pixels in the image, even though CWSs appears very close to the background and is not clearly visible. In contrast, as local thresholding works with sub-images locally and depends on the intensity values and changes dynamically over the image, it can solve this problem. Thus, adaptive thresholding is used to segment all possible CWSs area on the retinal image. Adaptive thresholding is a famous thresholding method for images with uneven illumination. Adaptive thresholding is implemented as follows [93]:

1. Binarize the image with threshold T .
2. Thin the resultant image.
3. Remove all branch points.
4. Place the remaining endpoints in line to use as starting point for tracking.
5. Track the object with T
6. Set the criterion $T=T-1$. If the object has passed testing, return to 5.

When implementing adaptive thresholding, the window size really affects the result of CWSs segmentation. Selecting too large size will result in the violation of the assumption of the unclearly visible CWSs as the background, and choosing too small may not cover sufficient foreground and background pixels, it will result in a poor threshold. Therefore, we adapted different window sizes of adaptive thresholding and evaluated their segmentation performance as illustrated in Figure 4.4. From the experimental results, the window size 90 x 90 yields the best segmentation performance with the average accuracy 98.1%.

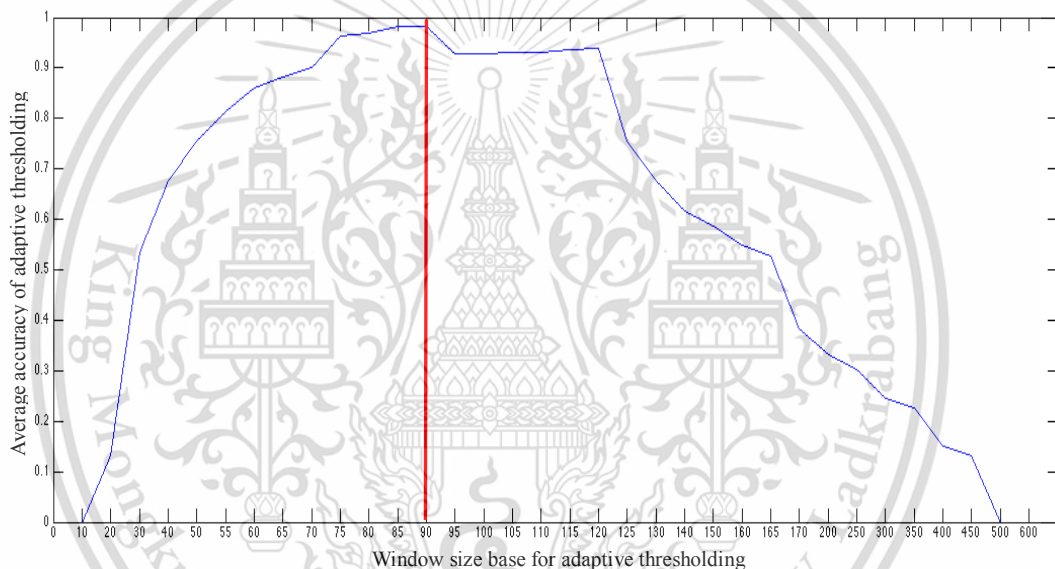


Figure 4.4 Performance of different window sizes of adaptive thresholding.

Nevertheless, the result from adaptive thresholding may contain a lot of noise. The built-in functions in MATLAB [94] “imclearborder” and “bwareaopen” are employed to remove the noises at the retinal image border and small amounts of noise, respectively. As clearly seen in Figure 4.5 (d), the presence of OD region and the noises at its vicinity were also interfering with the segmentation results of CWSs. In order to remove OD and the attached noises to OD, the location of OD is firstly detected using

our previous study [30], and then the rectangular mask is constructed to cover OD area. The size of the rectangular mask is based on the diameter of the localized OD. By combining the rectangular mask with the result of adaptive thresholding, we can remove all noise that is attached to the rectangular mask. The results at each step in the image segmentation is illustrated in Figure 4.5.

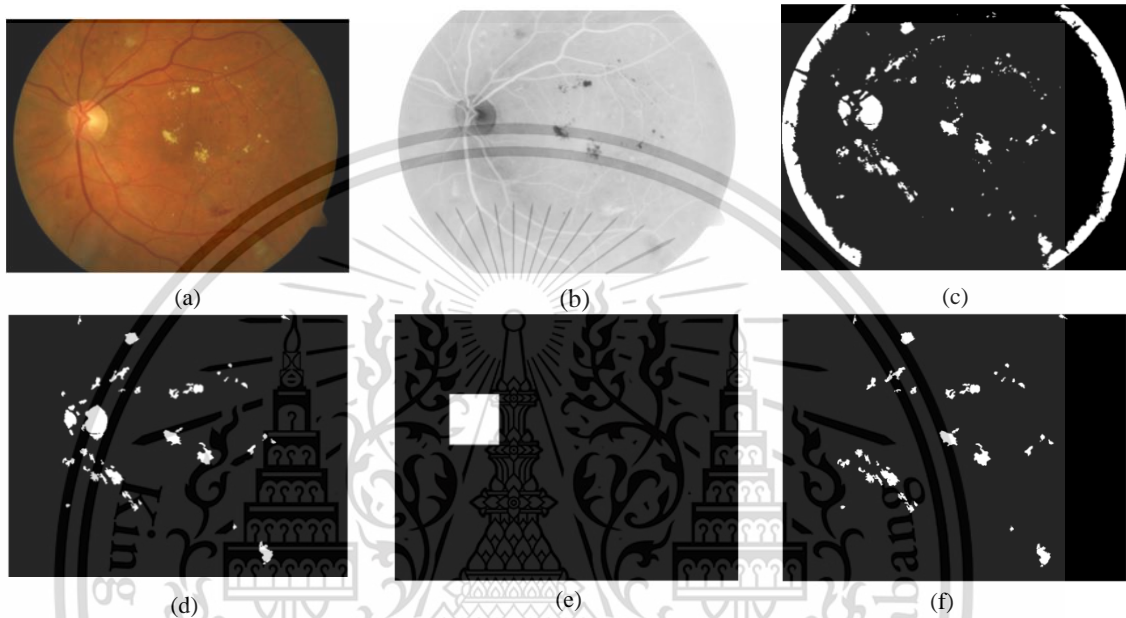


Figure 4.5 Image segmentation results: (a) original image, (b) enhanced image, (c) binarization image, (d) noise removal, (e) rectangular mask, and (f) segmentation result.

4.2.4 Feature Extraction

After image segmentation, the first stage of image analysis is feature extraction [95]. In our proposed method, we extracted the features of each CWSs based on its characteristics. Most CWSs can be differentiated from hard exudates and other noise in terms of texture and color information. Thus, some essential features from morphology, first order statistics, GLCM, GLRLM and lacunarity are extracted as presented in Table 4.2 and detailed in Appendix A.

Table 4.2 Extracted features.

| Features | Description |
|---|--|
| Morphological features | |
| F1 | Area of detected regions |
| F2 | Roundness of detected regions |
| F3 | Ratio between boundary of detected regions with its areas |
| F4 | Eccentricity of detected regions |
| F5 | Sodality of detected regions |
| F6 | Extent of detected regions |
| F7 - F8 | Maximum and minimum of intensity of the detected region |
| First order statistical features | |
| F9-F11 | The standard deviation of intensities in the red, green and blue channel within the detected regions in RGB color space. |
| F12-F14 | The standard deviation of intensities in hue, saturation and value within the detected regions in HSV color space. |
| F15-F17 | The standard deviation of intensities in L, a, and b within the detected regions in Lab color space. |
| F18-F20 | Mean of intensities in the red, green and blue channel within the detected regions in RGB color space. |
| F21-F23 | Mean of intensities in hue, saturation and value within the detected regions in HSV color space. |
| F24-F26 | Mean of intensities in L, a, and b within the detected regions in Lab color space. |
| F27 | Variances of intensity values within detected regions |
| F28 | Skewness of intensity values within detected regions |
| F29 | Kurtosis of intensity values within of detected regions |
| GLCM features | |
| F30-F117 | 22 features of GLCM matrix using four directions within detected regions [96-97] |
| GLRLM features | |
| F118-F161 | 11 features in GLRLM matrix using four directions within detected regions [98] |
| Fractal Analysis | |
| F162 | Lacunarity within detected regions |

4.2.5 Feature Selection

From features extraction, we obtained the initial feature set containing 162 features. All related works in the literature utilized all extracted features to classify CWSs whether it has the significant difference between CWSs and non-CWSs or not. Directly using all features for classification may cause time complexity, redundancy, and poor generalization capacity. In order to deal with the aforementioned issues, we do feature selection prior to the classification. ACO is applied to obtain the optimal feature set for training and testing the classification model and is given the promising accuracy. ACO is an inspired of ant's social behavior in their search for the shortest paths between food sources and their nests. Figure 4.6 illustrated the pseudo code of ACO algorithm.

```

Initialize: problemstate, populationsize, m,  $\rho$ ,  $\beta$ ,  $\sigma$ ,  $q_0$ 
Pbest  $\leftarrow$  CreateHeuristicSolution(Problemstate)
Pbestcost  $\leftarrow$  CostFunction(Sheu)
Pheromoneinit  $\leftarrow$   $\frac{1.0}{\text{problemstate} \times \text{Pbest}_{\text{cost}}}$ 
Pheromone  $\leftarrow$  InitializePheromone (Pheromoneinit)
while( $\neg$ Stopcondition)
  for (i = 1 To m)
    Si  $\leftarrow$  ConstructSolution(Pheromone, problemstate,  $\beta$ ,  $q_0$  )
    Si, cost  $\leftarrow$  CostFunction(Si)
    if Si, cost  $\leq$  Pbestcost
      Pbestcost  $\leftarrow$  Si, cost
      Pbest  $\leftarrow$  Si
    end
    LocalUpdateAndDecayPheromone(Pheromone, Si, Si, cost,  $\sigma$ )
  end
  GlobalUpdateAndDecayPheromone(Pheromone, Pbest, Pbestcost,  $\rho$ )
end
Return (Pbest)

```

Figure 4.6 Pseudo code for ACO

where m is the maximum iteration, ρ is the evaporation rate, β is the Heuristic Exponential Weight, σ is Pheromone Exponential Weight, and q_0 is the probability of doing deterministic choice.

To prove the efficiency of the proposed feature selection method, we also examined three robust feature selection methods as shown in Table 4.3, in which Genetic Algorithm (GA) and Particle Swarm Optimization (PSO) are the population-based nature-inspired optimization methods and stepwise method is the statistical model based selection method.

Table 4.3 Feature selection methods

| Feature selection methods | |
|-----------------------------------|---|
| Genetic Algorithm (GA) | <ul style="list-style-type: none"> - Introduced by John Holland (1960) - Officially in Holland's book (1975) - A search method that emulates the principles of genetic reproduction operations: crossover and mutation |
| Particle Swarm Optimization (PSO) | <ul style="list-style-type: none"> - Developed by Eberhart and Kennedy (1995) - Inspired by social behavior of bird flocking |
| Stepwise methods | <ul style="list-style-type: none"> - First proposed by Efroymson (1960) - An automatic procedure for statistical model selection. |

4.2.6 Classification

The optimal feature set from feature selection is used as input to the classifier. The classification step will differentiate between CWSs and non CWSs. SVM is regarded as one of the best supervised learning classifiers [99, 100]. In our proposed system, four types of SVM based classifiers: Linear SVM, Quadratic SVM, Gaussian SVM, and Cubic SVM are used for the classification and detail in Appendix B.

Suppose data $D = \{(\vec{x}_i, y_i), i = 1 \dots N\}$ and $y_i \in \{-1, +1\}$, the SVM classifier is

formulated as follows:

$$\min_{w,b,\xi} \frac{1}{2}\|\mathbf{w}\|^2 + C\sum_i \xi_i^2 \quad \text{subject to: } y_i(\mathbf{w}^T \mathbf{x}_i + b) \geq 1 - \xi_i, \quad \xi_i \geq 0, \quad \forall i \quad (20)$$

where $C > 0$ is the selected parameter and ξ comprises slack variables.

4.3 Experimental Results and Discussion

In this study, we tested our proposed method using MATLAB R2014a on a laptop with Intel core i3 CPU and 2 GB RAM. The study is based on three datasets containing 319 retinal images. We extracted a total of 1972 regions from 319 retinal images with 230 CWSs and 1742 non-CWSs, the detail was described in Table 4.1.

As mentioned in section 2, we conducted the experiments as outlined below:

1. All possible candidate areas are extracted from the background using adaptive thresholding method complemented by noise filtering methods.
2. Five feature sets: morphologies, first order statistics, GLCM, GLRLM, and lacunarity, are extracted.
3. GA, PSO, ACO, and stepwise based feature selection methods are examined to select the most discriminant features.
4. The selected features are used as input to SVM classifier. Linear, Quadratic, Gaussian and Cubic based SVM classifiers are employed.
5. The performances of GA coupling SVMs, PSO coupling SVMs, ACO coupling SVMs and stepwise method coupling SVMs are evaluated using three performance measures: sensitivity, specificity, and accuracy.

10-fold cross validation is used to evaluate the performance of the algorithms.

Three performance metrics: accuracy, sensitivity, and specificity [101] are measured to validate the effectiveness of the algorithms. Accuracy, defined in Eq. (2), evaluates the

correctness of a diagnostic test. Sensitivity, defined in Eq. (3), measures positive disease detection performance. Specificity, defined by Eq. (4), is the probability of correct non-disease identification. Where True positive (TP), false positive (FP), false negative (FN), and true negative (TN) are their associated parameters.

$$\text{Accuracy} = \frac{TP + TN}{TP + TN + FN + FP} \quad (21)$$

$$\text{Sensitivity} = \frac{TP}{TP + FN} \quad (22)$$

$$\text{Specificity} = \frac{TN}{TN + FP} \quad (23)$$

Where

- TP denotes the number of correctly classified CWSs.
- TN denotes the number of correctly classified non-CWSs.
- FP represents the number of wrongly classified CWSs.
- FN represents the number of wrongly classified non-CWSs.

We examined and compared the performance of GA, PSO, ACO, and stepwise method separately coupling with SVM classifiers using the same experimental setting and environment during the study. The comparative experimental results are described in Table 4.4, Table 4.5, Table 4.6 and Table 4.7 for GA coupling SVMs, PSO coupling SVMs, ACO coupling SVMs and stepwise method coupling SVMs respectively. The classification performance of the examined methods is graphically evaluated using Receiver Operator Characteristics (ROC) curve which is a graphical representation of diagnostic test evaluation. ROC curves are illustrated in Figure 4.7 (a), (b), (c) and (d) for GA coupling SVMs, PSO coupling SVMs, ACO coupling SVMs and stepwise

method coupling SVMs respectively. The Area Under ROC curve (AUROC) is computed and listed in Table 4.8.

Table 4.4 Classification results using GA pairing with four SVM classifiers

| Classifiers | Sensitivity | Specificity | Accuracy |
|--------------------|--------------------|--------------------|-----------------|
| Linear SVM | 49.18 % | 98.61 % | 92.49 % |
| Quadratic SVM | 68.85% | 98.38 % | 94.72 % |
| Gaussian SVM | 50.82 % | 100 % | 93.91 % |
| Cubic SVM | 86.88 % | 96.99 % | 95.74 % |

Table 4.5 Classification results using PSO pairing with four SVM classifiers

| Classifiers | Sensitivity | Specificity | Accuracy |
|--------------------|--------------------|--------------------|-----------------|
| Linear SVM | 47.54 % | 98.84 % | 92.49 % |
| Quadratic SVM | 68.85 % | 98.38 % | 94.72 % |
| Gaussian SVM | 50.82 % | 100 % | 93.91 % |
| Cubic SVM | 81.97 % | 97.22 % | 95.33 % |

Table 4.6 Classification results using ACO pairing with four SVM classifiers

| Classifiers | Sensitivity | Specificity | Accuracy |
|--------------------|--------------------|--------------------|-----------------|
| Linear SVM | 47.54 % | 98.84 % | 92.49 % |
| Quadratic SVM | 70.49 % | 98.84 % | 95.33 % |
| Gaussian SVM | 52.46 % | 100 % | 94.12 % |
| Cubic SVM | 90.16 % | 97.92 % | 96.96 % |

Table 4.7 Classification results using Stepwise method pairing with four SVM classifiers

| Classifiers | Sensitivity | Specificity | Accuracy |
|---------------|-------------|-------------|----------|
| Linear SVM | 50.82 % | 98.38 % | 92.49 % |
| Quadratic SVM | 67.21 % | 98.84 % | 94.93 % |
| Gaussian SVM | 52.46% | 100 % | 94.11 % |
| Cubic SVM | 85.25 % | 97.68 % | 96.15 % |

Table 4.8 AUROC for different pairs of feature selection and SVM classifiers

| Classifiers | AUROC | | | |
|---------------|---------|---------|---------|----------|
| | GA | PSO | ACO | Stepwise |
| Linear SVM | 92.40 % | 92.00 % | 91.54 % | 92.45 % |
| Quadratic SVM | 95.78 % | 95.43 % | 96.08 % | 96.78 % |
| Gaussian SVM | 95.89 % | 95.26 % | 96.16 % | 95.53 % |
| Cubic SVM | 96.86 % | 96.93% | 97.19 % | 95.36 % |

The experimental results show that ACO coupling with Cubic SVM achieved slightly better accuracy compared to GA coupling SVMs and PSO coupling SVMs, and achieved comparable accuracy with stepwise method. There might be no significant improvement between ACO coupling with Cubic SVM and stepwise method paring with Cubic SVM because accuracies of them were 96.96% and 96.15%, respectively. However, the sensitivity of the proposed method i.e., ACO coupling with Cubic SVM, was 4.91 % better than stepwise method coupling with Cubic SVM when specificities of them are similar. Moreover, ACO coupling with Cubic achieved the highest AUROC

by given 97.19%. Thus, our proposed CWSs detection method will be useful for physicians.

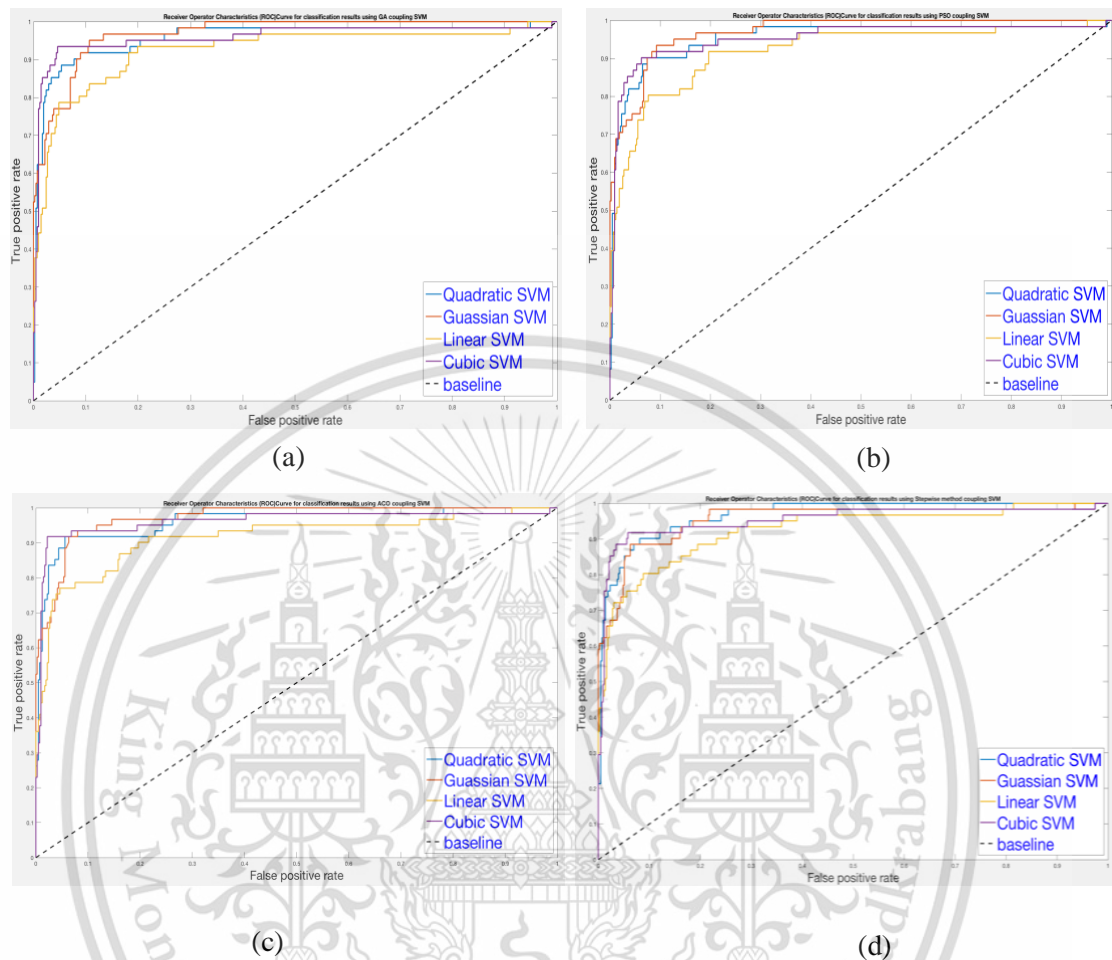


Figure 4.7 ROC curves of (a) GA coupling SVMs, (b) PSO coupling SVMs, (c) ACO coupling SVMs and (d) Stepwise method coupling SVMs.

The experimental results also exhibit that Cubic SVM yields better performance compared to other kernels, and Linear SVM show poor performance compared to other kernels. It is our observation that our data is not linearly separable. Therefore, linear SVM failed to draw the decision boundary to coherently separate between CWSs and non-CWSs data. The visual results of detected cotton wool spots are illustrated in Figure 4.8. As described in Table 4.9, it is hard to make a fair and objective comparison

between the related works and the proposed method because different dataset and experimental setting is used.

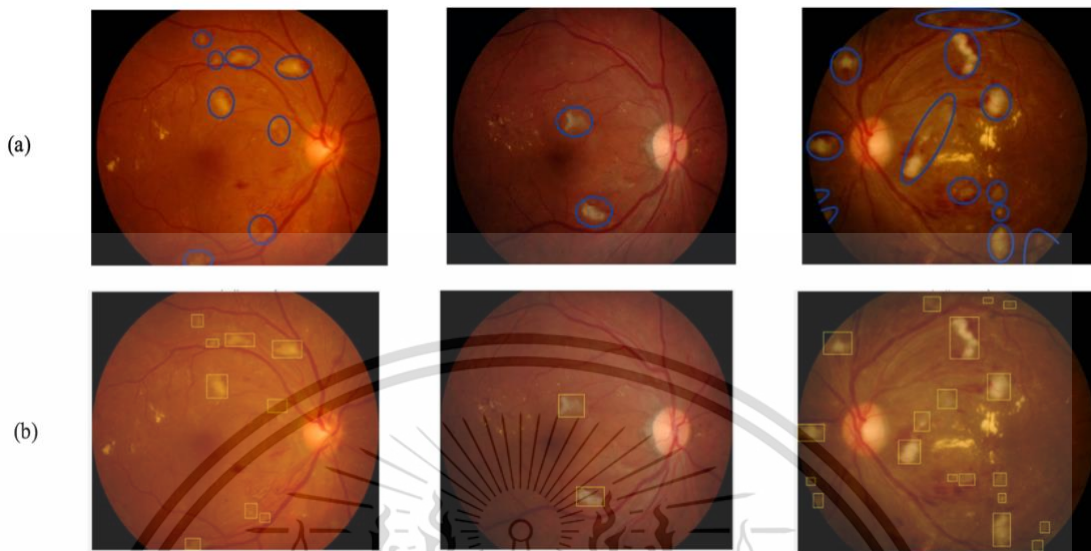


Figure 4.8 The visual results of detected cotton wool spots from images with the presence of CWSs in different degree; (a) ground truth image and (b) detected cotton wool spots by the proposed method.

Table 4.9 The performance of the previous works and our proposed method.

| Authors | Year | No. of images | Segmented methods | Input features/ Classifiers | Performance |
|------------------------|------|---------------|-----------------------------|-----------------------------|--|
| Meindert et al. [62] | 2007 | 300 | – Manual thresholding | – 83 features – KNN | Sen=70% Sp=93% AUC= 85% |
| Clara et al. [63] | 2009 | 13 | – Manual thresholding | – 83 features – KNN | AUC= 82% |
| Samra et al. [66] | 2014 | 30 | – Otsu’s thresholding | | Sen= 82.21% |
| Jagatheesh et al. [70] | 2015 | 250 | – Bag of visual words model | – SVM | Acc= 78.23% Sen= 72.15% Sp= 79.40% |

| | | | | | |
|------------------|------|-----|---|-------------------------------|---|
| Toan et al. [65] | 2017 | 89 | -Analyze on the entire image with no OD | -12 features -ANN | Acc= 85.54 % Sen = 85.9 % Sp= 84.4 % |
| Proposed methods | 2018 | 319 | -Adaptive thresholding | -162 features -ACO -SVM | Acc = 96.96 % Sen= 90.16% SP= 97.92% AUC= 97.19% |

4.4 Summary

Detection of CWS is a challenging and difficult task for computer-aided diagnosis systems in DR lesions classification because CWS appears very close to the background and is not clearly visible. This chapter proposed an effective method for CWS detection based on its appearance. In the proposed method, the image is first enhanced, and then, adaptive thresholding is applied for image segmentation as it performs better than other thresholding methods for CWS area segmentation. Three types of noise are removed to avoid interference in the final results: noise in the vicinity of the OD area, noise at the border of the retinal image, and small noise. ACO coupling Cubic SVM operate as a processor to select the most significant features from morphologies, first order statistics, GLCM, GLRLM and lacunarity based features extraction. The proposed method yielded sensitivity 90.16 %, specificity 97.92 %, accuracy 96.96%, and AUROC 97.19 % and average computation time 17.72s per image. Due to its high accuracy and simplicity, the proposed method can be used as a supportive tool in DR diagnosis and grading.

CHAPTER 5

GRADING OF DR USING DEEP LEARNING

As described in the previous chapter, DR is a crucial eye disease that is currently subjective, and in need the eye specialists to perform the test. Grading the severity of DR is essential for the ophthalmologists to make an effective treatment plan to protect the patients' vision against blindness. However, due to the insufficient number of eye specialists, an automatic DR grading system is proposed in this chapter to grade the severity of DR more objective so that the ophthalmologists can make an effective treatment plan to protect the patients' vision against blindness.

5.1 Introduction

Recently, due to the advance technology in medical devices, there has been more possibility to get data for medical image analysis. Numerous techniques have been proposed to grade the severity of DR using isolate image processing method or integrated with machine learning techniques. Machine learning algorithms have been applied for many applications such as computer vision, bioinformatics, information retrieval, marketing, natural language processing, social networks, online advertising, and so on. Conventional machine learning methods were limited in interpreting the raw data directly into a suitable pattern from which a classifier can learn. As shown in Figure 5.1, this process requires the explicit domain knowledge by experts to design the hand-crafted feature extraction and do experiments based on the specify datasets [103-105]. The obtained results are more generally specialized on a dataset, and new experiments might require with difference dataset. Deep learning as illustrated in Figure 5.2 is a recent and fast-growing field of machine learning. It has turned out to be very good at

discovering intricate structures in high-dimensional data and is therefore applicable to interpreting the raw data directly. The basic ideas of the decision making to choose traditional machine learning and deep learning are also provided in Table 5.1.

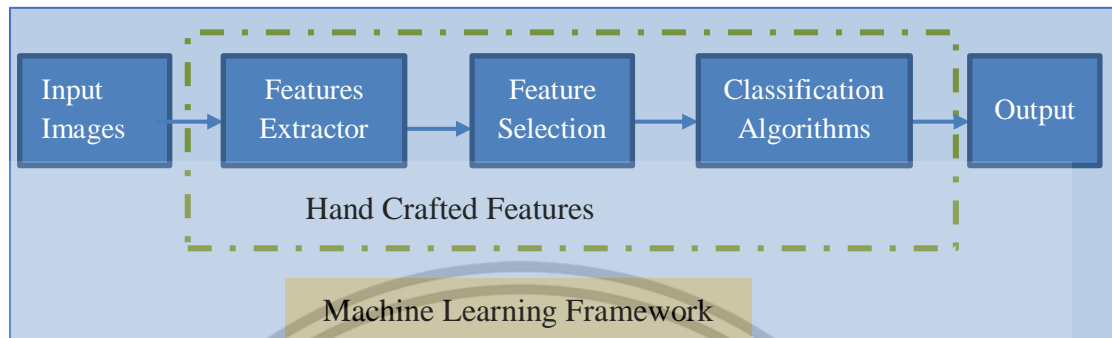


Figure 5.1 Traditional machine learning framework.

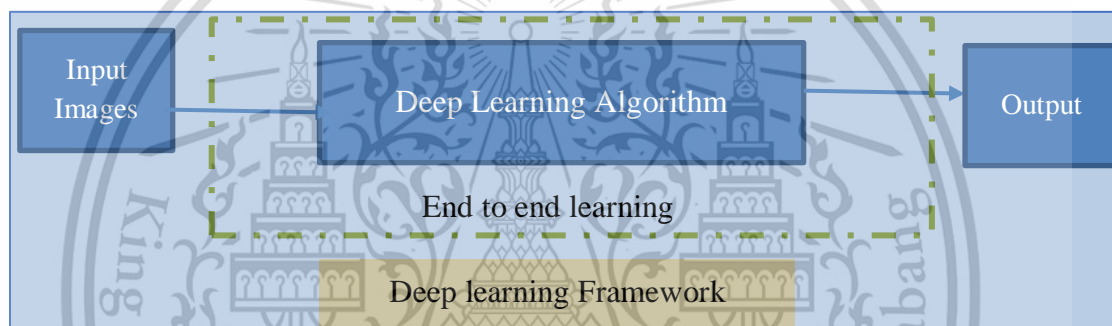


Figure 5.2 Deep learning framework.

In the literature, deep learning was applied in many applications of computer vision, medical image processing, information retrieval, marketing, natural language processing, and online advertising, etc. The recent applications of deep learning in medical image analysis have been applied for remote sensing [106], skin disease detection [107], cancer detection [108, 109] as well as retinal disease detection [110-113].

Masoud et al. [106] reported a complex land cover mapping in Canada using multispectral remote sensing imagery based on 7 deep learning methods, namely VGG16, VGG19, DenseNet121, InceptionV3, InceptionResNetV, Xception, and

ResNet50. The performance evaluation showed that InceptionResNetV2 gives the best accuracy followed by ResNet50 and Xception respectively.

Andre et al. [107] applied deep neural networks in dermatology to classify cancer or normal skin conditions using a Convolutional Neural Network (CNN). The performance evaluation was evaluated with diagnostic tasks: keratinocyte carcinoma classification, melanoma classification and melanoma classification using dermoscopy based on 21 dermatologists. The experimental results showed that the CNN achieves comparable results with experts.

Table 5.1 Traditional machine learning and deep learning

| Methods Differences | Traditional Machine Learning | Deep Learning |
|------------------------|--|---|
| Data Dependencies | Good results for small dataset | Large datasets are required |
| Execution time | Take short time to train (A few minutes - A few hours) | Time intensive (A few days – A few weeks) |
| Feature Engineering | Hand crafted features is need to test different features and classifiers to achieve the best performances. | Automatically learns the features and classifiers |
| Hardware Dependencies | Low-end machines | High-end machines |
| Interpretability | Easy to interpret the reasoning behind it and the accuracy is plateaus | Fail to interpret the results and the accuracy is unlimited |

Philipp et al. [108] studied histopathological images of colorectal cancer to classify the benign and malignant tissue using deep learning. The classification performance was evaluated for benign and malignant tissue on two test sets A and B and achieved an accuracy of 98.33% and 93.75% respectively.

Joon et al. [110] presented a pilot project using a small open retinal dataset (STARE database) to classify 10 different eye diseases. Since the input data is small (279 images), firstly data augmentation techniques were applied to randomly retrieve transformed 1000 fundus images per each eye disease class. Then each class of the eye diseases was identified using four different models in deep learning: transfer learning with random forest based on VGG-19 structure (VGG19-TL-RF), transfer learning with Gaussian kernel SVM based on VGG-19 structure (VGG19-TL-SVM), VGG-19 and AlexNet.

Kele et al. [111] reported an accuracy of 94.5%, a better result comparing to the conventional machine learning, on the study of deep convolutional neural networks for automated classify the DR using local retinal images.

Avishek et al. [112] presented a deep neural ensemble network architecture to segment retinal blood vessel. The performance evaluation of the result was tested on DRIVE dataset using unsupervised hierarchical feature learning based on bootstrap samples and different network architectures. By comparing to other major algorithms, the paper received higher efficacy with the maximum average accuracy of 95.33%.

Yidong et al. [113] combined the medical domain knowledge and deep learning model to diagnose glaucoma. In the first step, the area of optic disc was segmented image processing techniques and then its feature values including cup-to-disc ratio, Retinal nerve fiber layer defects (RNFLD), Peripapillary Atrophy (PPA), optic disc

size and optic cup size were extracted to use as the input for multi-branch neural network model. The paper showed the outfit performance by comparing to the previous research works with the accuracy, sensitivity, and specificity of 91.51%, 92.33 %, and 90.90% respectively.

Despite recent advances of deep Convolutional Neural Networks (CNNs) in various medical image analysis tasks, their potential for DR detection has not been thoroughly explored. In particular, the applications of deep CNNs using fundus images for grading the severity of DR. In this work, we study and compare the result on five well-known deep CNN, AlexNet, GoogleNet, Inception V3, ResNet50, and ResNet 101, to grade the severity of DR into healthy retina, NPDR and PDR.

5.2 Methods

CNN is currently one of the most notable deep learning approaches for the application of image analysis. It was first introduced by Fukushima in 1988 [114] and applied in medical image analysis by Lo et al. [115] in 1995. The first successful application of CNN was reported by LeCun et al. [116] in 1998 for the problem of handwritten digit classification. However, the use of CNN did not gather momentum until the advances were made in high computing system and the deep learning networks were developed. The contribution of Krizhevsky et al [117] called AlexNet was the watershed for the application of CNN to win the ImageNet competition in 2012. Since then deep CNNs have become the technique of choice for the application of images analysis.

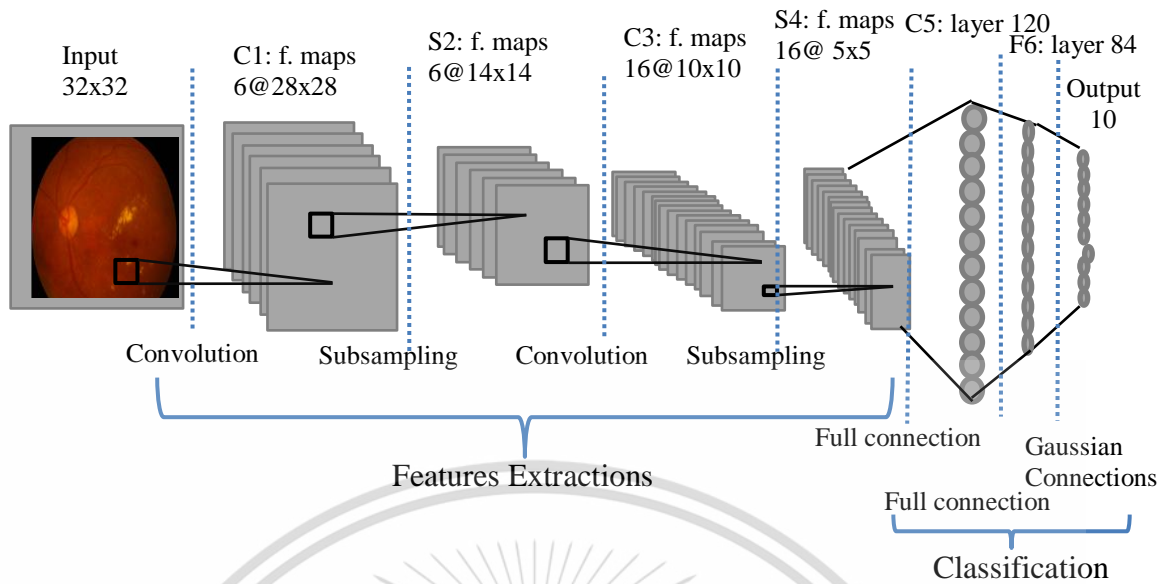
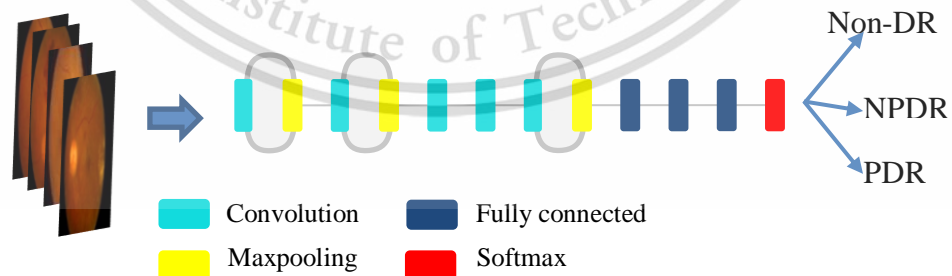


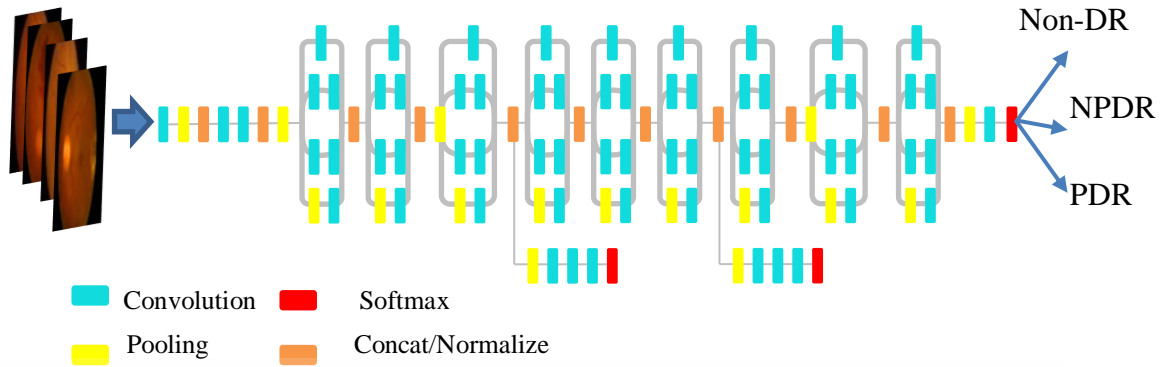
Figure 5.3 The Overview of convolutional neural networks (LeNet5).

Figure 5.3 illustrates the LeNet5 architecture. It consists of a feature extractor part and a classifier part. In feature extraction part, each layer receives its input from the output of the previous layer and passes its output to the next layer as the input. The CNN architecture consists of three layers: convolution layers, pooling layers, and classification layers.

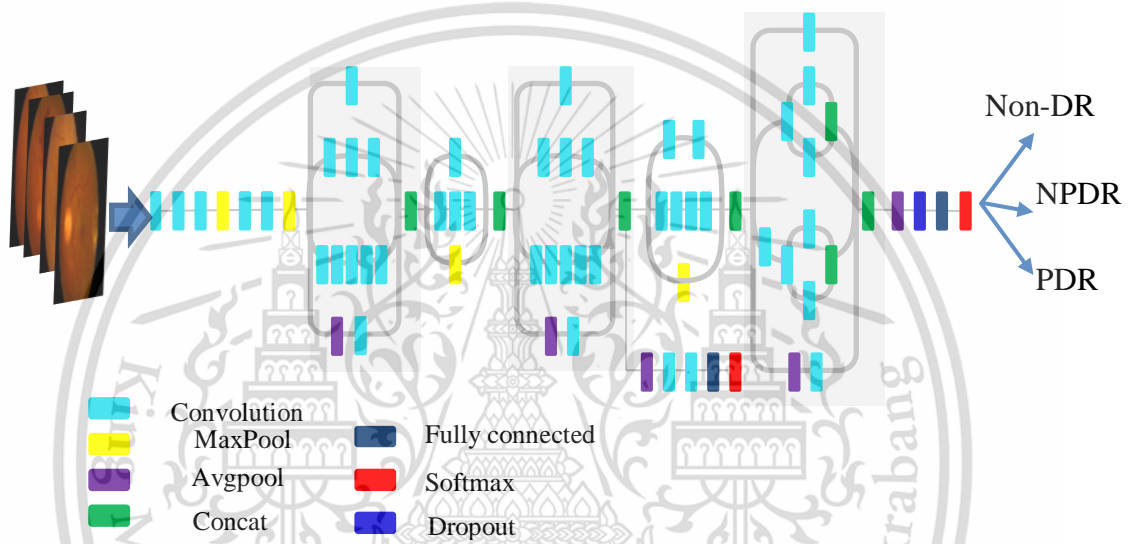
In this chapter, we briefly discuss on the popular deep CNNs which is proposed to grade the severity of DR as presented in Figure 5.4 below:



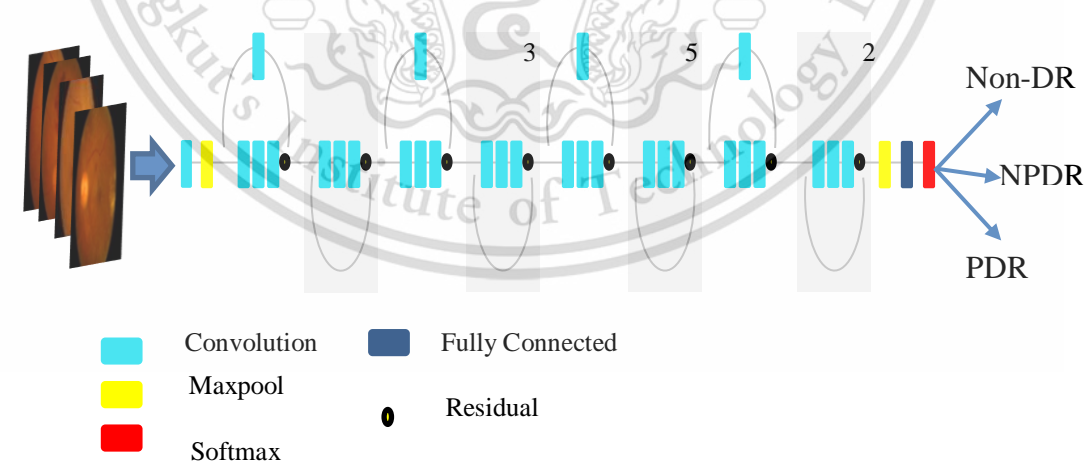
a. AlexNet architectures



b. GoogleNet architectures



c. Inception V3 architectures



d. ResNet50 architectures

Figure 5.4 Different deep CNN architectures

The architecture of AlexNet illustrated in Figure 5.4 (a) consists of 5 convolutional layers, three pooling layers, and three fully connected layers. The input images first automatically resize the images into a fixed size $227 \times 227 \times 3$ in the first layer before they are input to the network, then the network repeatedly convolves and pool the activations to extract the image features before forwarding the results into the fully-connected layers. The network was trained on ImageNet dataset to classify images into 1000 object categories and won the first place in ImageNet competition in 2012.

Similarly, GoogLeNet or Inception V1 shown in Figure 5.4(b) was the winner of ImageNet competition in 2014 was developed by a research group at Google by adding the concept of Inception module. The convolutional filter of different sizes and concatenates their outputs were applied, letting the model decide which filter size does the best job at capturing features. Additionally, it uses average pooling instead of fully connected layers at the final network layers. Inception V3 is a deeper and improved version of Inception V1 and V2 by adding the concept of factorization of convolutions and improved normalization and it is illustrated in Figure 5.4 (c).

Residual Network (ResNet) architecture [118] was the winner of ImageNet competition in 2015 and the first deep CNN network that can beat human level accuracy. It was developed by Kaiming et al with a deeper neural network based on residual network functions. Many different ResNet architectures were studied and compared the results due to the numbers of layers; 34,50,101,152, and 1202. An example of ResNet architecture was presented in Figure 5.4 (d). It is ResNet50 which is one of the popular ResNet architectures containing 49 convolution layers and 1 fully connected layer at the end of the network.

Since our data is small we proposed a framework for grading the severity of DR based on the transfer learning approaches as illustrated in Figure 5.5. Firstly, the data was prepared and built a labeling into three different classes, then based on the transfer learning approaches; load the pre-trained network and use it as a starting point to learn our task in grading the severity of DR by replacing the last three layers which is configured for 1000 classes to 3 classes Non-DR, NPDR and PDR (see in Figure5.6). Finally train the network that consists of the transferred and new layers. Five deep CNNs namely AlexNet, GoogleNet, Inception V3, ResNet50, and ResNet 101 were used and compared the results.

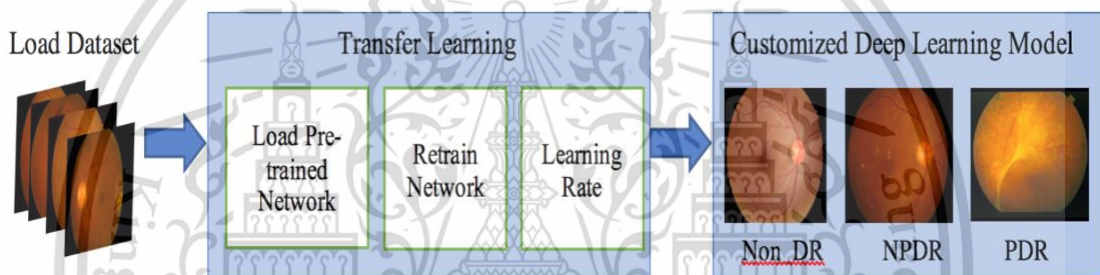


Figure 5.5 Proposed Framework for Grading the Severity of DR

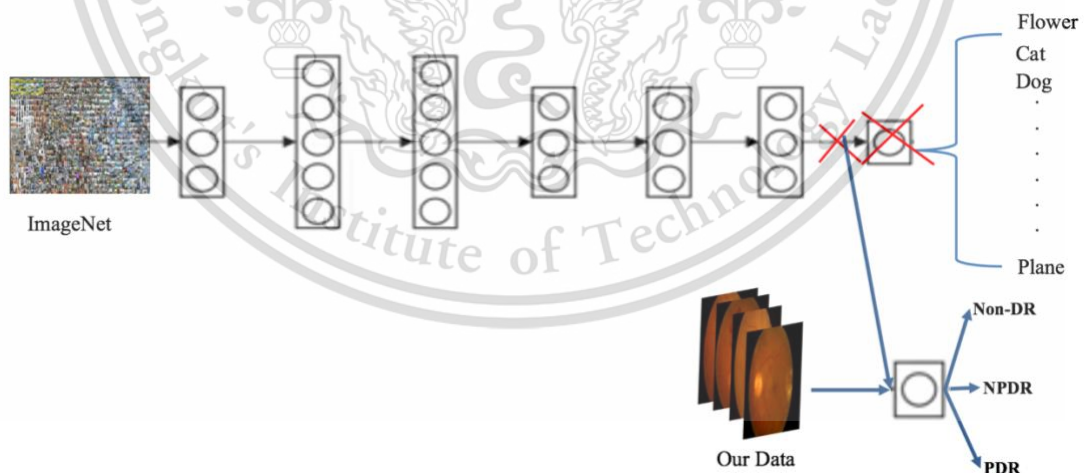


Figure 5.6 The concept of transfer learning for grading the severity of DR

5.3 Results and Discussion

A total of 1342 retinal images as illustrated in Table 5.2 have been used to grade the severity of DR into healthy retinal image (Non-DR), NPDR and PDR using five well-known deep learning models namely AlexNet, GoogleNet, InceptionV3, ResNet50, and ResNet101. The results of those CNN models with original images and by applying image enhancement are detail in Table 5.3 and Table 5.4. ResNet50 give the best performance for original images with the accuracy of 90.57%, sensitivity of 88.24%, specificity 91.04%, F-measure of 75.95% and precision of 66.67% and ResNet101 give the best result enhanced images with the accuracy of 91.32%, sensitivity of 80.88%, specificity 93.43%, F-measure of 75.86% and precision of 71.86% for ResNet101. The confusion matrix for both ResNet50 and ResNet101 are illustrated in Figure 5.7 and Figure 5.8 respectively.

By applying image enhancement, AlexNet and ResNet101 give slightly better accuracy comparing to the result without applying image enhancement (AlexNet: 88.83% to 89.83%, ResNet101: 90.32% to 91.32%), and the accuracy remain the same for Inception V3 (87.1 %). However, the results slightly reduce for both ResNet50 (90.57 % to 89.08 %) and GoogleNet (87.6% to 83.13 %). Thus, we can conclude that there is unnecessary to apply image enhancement for grading the severity of DR using deep CNNs.

Table 5.2 Datasets descriptions

| Dataset | Pathological signs of retinal images | | No of images |
|----------------------------------|--------------------------------------|---------------------------|--------------|
| Local dataset IDRiD* STARE | Non-DR | Healthy retinal images | 226 |
| | NPDR | Mild NPDR | 790 |
| | | Moderate NPDR | |
| | | Severe NPDR | |
| | PDR | New blood vessels growing | 328 |
| | | Neovascularization | |
| Fibrous proliferations | | | |
| Total original images | | | 1342 |

*Indian Diabetic Retinopathy image Dataset (IDRiD)

Table 5.3 Performance evaluation of deep learning methods for original data

| Methods | Sensitivity | Specificity | Precision | F-Measure | Accuracy |
|-----------------|---------------|---------------|---------------|---------------|---------------|
| AlexNet | 76.47% | 91.34% | 64.20% | 69.80% | 88.83% |
| GoogleNet | 91.12% | 86.87% | 58.49% | 71.12% | 87.6 % |
| InceptionV3 | 83.82% | 87.76% | 58.16% | 68.67% | 87.1 % |
| ResNet50 | 88.24% | 91.04% | 66.67% | 75.95% | 90.57% |
| ResNet101 | 80.88% | 92.24% | 67.90% | 73.83% | 90.32% |

Table 5.4 Performance evaluation of deep learning methods with image enhancement

| Methods | Sensitivity | Specificity | Precision | F-Measure | Accuracy |
|------------------|---------------|---------------|---------------|---------------|---------------|
| AlexNet | 92.65% | 89.25% | 63.64% | 75.45% | 89.83% |
| GoogleNet | 79.41% | 83.88% | 50% | 61.36% | 83.13 % |
| InceptionV3 | 79.41% | 88.66% | 58.70% | 67.50% | 87.10% |
| ResNet50 | 69.12% | 93.13% | 67.14% | 68.12% | 89.08% |
| ResNet101 | 80.88% | 93.43% | 71.43% | 75.86% | 91.32% |

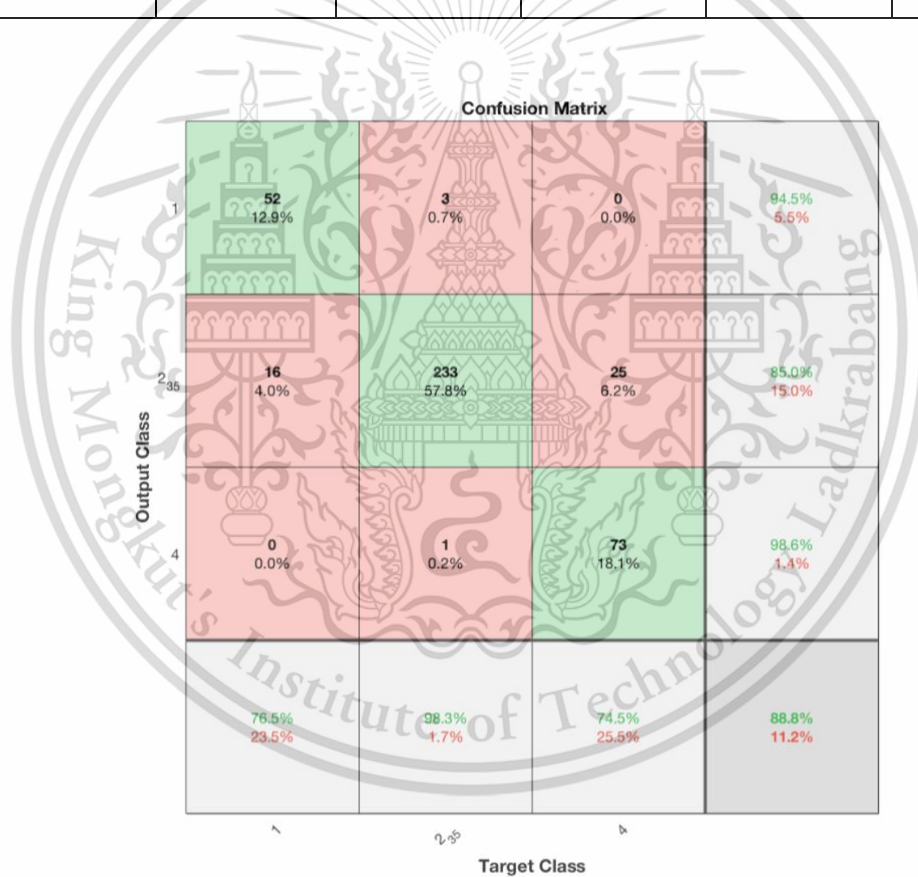


Figure 5.7 The confusion matrix of ResNet50 for original data

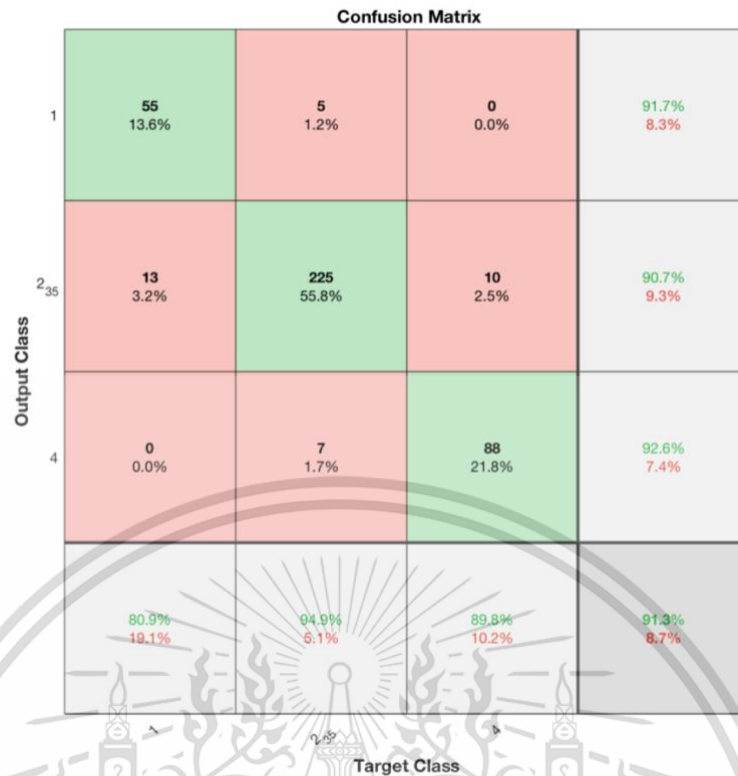


Figure 5.8 The confusion matrix of ResNet101 with enhanced images

5.4 Summary

In this chapter, we have presented the deep learning approach for grading the severity of DR. Instead of building deep learning models from scratch, we employed the transferring learning approach by adapting the pre-trained models into the grading of DR. We thoroughly investigated various pre-trained CNN models namely AlexNet, GoogLeNet, ResNet50, Inception V3 and ResNet101. The experimental results show that the residual networks (i.e., ResNet50 and ResNet101) provided superior grading accuracy than other CNN models with the accuracy of 90.57%. Thus, it is reasonable to conclude that deep learning models are suitable for grading of DR.

CHAPTER 6

CONCLUSIONS AND FUTURE WORKS

This thesis proposed a computer-aided diagnosis system for DR to assist the ophthalmologists in the primary screening process. Development of computer-aided diagnosis system for DR is essential and a challenging task. It requires not only the understanding of computer vision technique but also the expert knowledge related to medical input; DR screening procedure and retinal images. This chapter concludes the thesis and presents the future research directions. Section 6.2 summaries the main contributions of the research work and section 6.3 presents the future research direction.

6.1 Summary of the research works

The thesis presents the detail of the proposed methods into three tasks. Firstly, we attempt to screen the retinal images into DR or non-DR as described in chapter 2. The proposed algorithm stands for extraction of information-features from the segmented region of interests by Kirsch edges detection and morphological top hat. Then the most significant features were selected by developing a hybrid simulated annealing based feature selection algorithm. Finally, EB was used to differentiate healthy retinal images and DR images. The proposed algorithm outperforms the previous studies.

For further analysis, we also studied on each DR lesions detection which were categorized into two groups: red lesions and bright lesions. The algorithm applied to detect Red lesions (MAs and HEs) were described in chapter 3. MAs were detected using the new combination of canny edge and morphology operations. The combination is simple, yet effective. For the detection of HEs, we applied top-hat transform to extract

all possible HEs and blob analysis was subsequently applied to remove the fovea area and blood vessels. For the detection of bright lesions, we introduced a novel algorithm to detect CWSs by combining the image processing and machine learning techniques as reported in chapter 4. Initially, adaptive thresholding is used to segment all possible bright lesions and then OD which is a component of the retina was removed to avoid incorrect detections. After that, a total of 162 features from morphology, texture, and color was extracted, and a novel feature selection algorithm which hybridizes ANN and ant colony optimization algorithm was utilized to select the discriminant features. Using the selected features, SVM was applied as the classifier to classify between CWSs and other bright objects.

Finally, in chapter 5, we reported grading the severity of DR by using deep learning approach. We graded the retinal images as healthy, NPDR and PDR based on five CNN models namely AlexNet, GoogLeNet, ResNet50, Inception V3 and ResNet101. ResNet50 received the highest with the accuracy of 90.57%.

The novelty of this thesis stands for the proposed framework to detect CWSs areas. CWSs can appear isolated or with other pathological signs such as hard exudates, microaneurysms or hemorrhages. Although various robust and efficient methods have been proposed for the detection of microaneurysms, hemorrhages, and hard exudates, only a few have been proposed for CWSs. Detection of CWSs remain challenging due to their uneven appearance, in which some CWSs are not clearly visible and some resemble with hard exudates. In this thesis, we studied and experimented the image segmentation methods to segment the CWSs areas. Global thresholdings can extract some bright objects in the retinal image (exudates and OD). However, Global thresholding methods fail to detect CWSs areas because they use only one optimal value

for all pixels in the image, even though CWSs appears very close to the background and is not clearly visible. In contrast, as adaptive thresholding works with sub-images locally and depends on the intensity values and changes dynamically over the image, it can solve this problem. Thus, adaptive thresholding is applied to segment all appeared CWSs areas on the retinal image. It is the first idea in the literature of CWSs detection using retinal images.

6.2 Future works

As highlighted in the previous chapter, the work presented in this thesis can be extended in a variety of ways.

For red lesions detection: Given a successful rate of 90 % with the average processing time 9.53 seconds and 6.23 seconds per image for MAs and HEs detection respectively, the proposed methods are acceptable for time complexity. However, the proposed methods do not work well with poor quality images. For this reason, we can see that applying only the image segmentation methods is not able to deal with the poor quality retinal images. Therefore, in the future, we need to study more detail about the features of each lesion and extract them as the input for the classification step.

For CWSs detection: more classifiers should be tested to compare the result with four SVMs classifiers proposed in this thesis, and more images should be applied to make the proposed method strong and be able to apply in a real application in hospital.

For grading of the severity of DR using deep learning: more retinal images should be collected from the hospital and test with the proposed method to allow the system learn more from the data since deep learning need a large data to learn to improve the performance and make the result more accurate.

BIBLIOGRAPHY

1. International Diabetes Federation. IDF Diabetes Atlas, 8th ed.; IDF: Brussels, Belgium, 2017; Available online: <http://www.diabetesatlas.org> (accessed on 27 June 2018).
2. World Health Organization. Global Report on Diabetes; WHO: Geneva, Switzerland, 2016.
3. International Diabetes Federation. IDF Diabetes Atlas, 8th ed.; IDF: Brussels, Belgium, 2017; Available online: <http://www.diabetesatlas.org> (accessed on 27 June 2018).
4. Scanlon, P.H.; Aldington, S.; Wilkinson, C.; Matthews, D. Practical Manual of Diabetic Retinopathy Management; John Wiley & Sons: Chichester, UK, 2009; pp. 46–57. ISBN 978-1-405-17035-2.
5. Wade, N. J. (2007). Image, eye, and retina. *Journal of the Optical Society of America A*, 24(5), 1229-1249. <https://doi.org/10.1364/JOSAA.24.001229>.
6. Kolb H. Simple Anatomy of the Retina. 2005 May 1 [Updated 2012 Jan 31]. In: Kolb H, Fernandez E, Nelson R, editors. *Webvision: The Organization of the Retina and Visual System* [Internet]. Salt Lake City (UT): University of Utah Health Sciences Center; 1995-. Available from: <https://www.ncbi.nlm.nih.gov/books/NBK11533/>
7. Simple anatomy of the eye nervous layer of the eye sensory perception anatomy and physiology, www.theanatomybody.com.
8. World Health Organization. Global Report on Diabetes; WHO: Geneva, Switzerland, 2016.

9. “What is Diabetic Retinopathy and what causes it?”, www.rebuildvision.com.
10. “Diabetic Retinopathy”,
[http://www.siskiyoueye.com/sec-medical services/diabetic-retinopathy](http://www.siskiyoueye.com/sec-medical-services/diabetic-retinopathy)
11. Klein, R., Klein, B.E. and Moss, S.E., 1984. Visual impairment in diabetes. *Ophthalmology*, 91(1), pp.1-9.
12. Crick, R.P. and Khaw, P.T., 2003. A textbook of clinical ophthalmology: a practical guide to disorders of the eyes and their management.
13. R.N. Frank, “Diabetic retinopathy”, *Prog. Retin. Eye Res.*, 14 (2) (1995), p. 361.
14. “Diabetic Retinopathy”, <https://www.eyephysicianspc.com/ocular-disease-treatments-columbus/diabetic-retinopathy>
15. Acharya, U.R.; Mookiah, M.R.K.; Koh, J.E.; Tan, J.H.; Bhandary, S.V.; Rao, A.K.; Fujita, H.; Hagiwara, Y.; Chua, C.K.; Laude, A. Automated screening system for retinal health using bi-dimensional empirical mode decomposition and integrated index. *Comput. Biol. Med.* **2016**, 75, 54–62. [CrossRef] [PubMed]
16. Koh, J.E.; Acharya, U.R.; Hagiwara, Y.; Raghavendra, U.; Tan, J.H.; Sree, S.V.; Bhandary, S.V.; Rao, A.K.; Sivaprasad, S.; Chua, K.C.; et al. Diagnosis of retinal health in digital fundus images using continuous wavelet transform (CWT) and entropies. *Comput. Biol. Med.* **2017**, 84, 89–97. [CrossRef] [PubMed]
17. Kumar, P.S.; Deepak, R.U.; Sathar, A.; Sahasranamam, V.; Kumar, R.R. Automated Detection System for Diabetic Retinopathy Using Two Field Fundus Photography. *Procedia Comput. Sci.* **2016**, 93, 486–494. [CrossRef]
18. Kumar, P.S.; Kumar, R.R.; Sathar, A.; Sahasranamam, V. Automatic detection of exudates in retinal images using histogram analysis. In Proceedings of the 2013

IEEE Recent Advances in Intelligent Computational Systems (RAICS), Trivandrum, India, 19–21 December 2013; pp. 277–281.

19. Kumar, P.S.; Kumar, R.R.; Sathar, A.; Sahasranamam, V. Automatic detection of red lesions in digital color retinal images. In Proceedings of the Contemporary Computing and Informatics (IC3I), Mysore, India, 27–29 November 2014; pp. 1148–1153.
20. Imani, E.; Pourreza, H.R.; Banaee, T. Fully automated diabetic retinopathy screening using morphological component analysis. *Comput. Med. Imaging Graph.* **2015**, *43*, 78–88. [CrossRef] [PubMed]
21. Goh, J.; Tang, L.; Saleh, G.; Al Turk, L.; Fu, Y.; Browne, A. Filtering normal retinal images for diabetic retinopathy screening using multiple classifiers. In Proceedings of the 9th International Conference on Information Technology and Applications in Biomedicine, Larnaca, Cyprus, 4–7 November 2009; pp. 1–4.
22. Akram, M.U.; Khalid, S.; Tariq, A.; Khan, S.A.; Azam, F. Detection and classification of retinal lesions for grading of diabetic retinopathy. *Comput. Biol. Med.* **2014**, *45*, 161–171. [CrossRef] [PubMed]
23. Aliahmad, B.; Kumar, D.K.; Jain, R. Automatic analysis of retinal vascular parameters for detection of diabetes in Indian patients with no retinopathy sign. *Int. Sch. Res. Not.* **2016**, *2016*, 8423289. [CrossRef] [PubMed]
24. Siva Sundhara Raja, D.; Vasuki, S. Automatic detection of blood vessels in retinal images for diabetic retinopathy diagnosis. *Comput. Math. Methods Med.* **2015**, *2015*, 419279. [CrossRef] [PubMed]

25. Rajashekar, D.; Srinivasa, G.; Vinekar, A. Comprehensive Retinal Image Analysis for Aggressive Posterior Retinopathy of Prematurity. *PLoS ONE* **2016**, *11*, e0163923. [CrossRef] [PubMed]
26. Li, H.; Liu, K.R.; Lo, S.C. Fractal modeling and segmentation for the enhancement of microcalcifications in digital mammograms. *IEEE Trans. Med. Imaging* **1997**, *16*, 785–798. [CrossRef] [PubMed]
27. Akram, F.; Garcia, M.A.; Puig, D. Active contours driven by local and global fitted image models for image segmentation robust to intensity inhomogeneity. *PLoS ONE* **2017**, *12*, e0174813. [CrossRef] [PubMed]
28. R.A. Kirsch, “Computer determination of the constituent structure of biological images”, *Computers and biomedical research*, 4(3), pp.315-328, 1971.
29. H. Bhadauria, S. Bisht, and A. Singh, “Vessels extraction from retinal images”, *IOSR Journal of Electronics and Communication Engineering (IOSR-JECE)* e-ISSN, pp.2278-2834, 2013.
30. S. Sreng, N. Maneerat, D. Isarakorn, B. Pasaya, J.I. Takada, R. Panjaphongse, and R. Varakulsiripunth : “Automatic exudate extraction for early detection of Diabetic Retinopathy”, In *Information Technology and Electrical Engineering (ICITEE)*, International Conference on IEEE, pp. 31-35 (2013)
31. GLCM texture features. Available online:
<https://www.mathworks.com/matlabcentral/fileexchange/22187-glcm-texture-features> (accessed on 8 June 2018).
32. Tang, X. Texture information in run-length matrices. *IEEE Trans. Image Process.* **1998**, *7*, 1602–1609. [CrossRef] [PubMed]

33. Ojala, T.; Pietikainen, M.; Maenpaa, T. Multiresolution Gray Scale and Rotation Invariant Texture Classification With Local Binary Patterns. *IEEE Trans. Pattern Anal. Mach. Intell.* 2002, 24, 971–987. [CrossRef]
34. Ojala, T.; Pietikainen, M.; Harwood, D. A comparative study of texture measures with classification based on featured distributions. *Pattern Recognit.* 1996, 29, 51–59. [CrossRef]
35. Kirkpatrick, S.; Gelatt, C.D.; Vecchi, M.P. Optimization by simulated annealing. *Science* 1983, 220, 671–680. [CrossRef] [PubMed]
36. Lee, J.S.; Park, C.H.; Ebrahimi, T. Theory and applications of hybrid simulated annealing. In *Handbook of Optimization*; Springer: Berlin, Heidelberg, 2013; pp. 395–422.
37. Anghinolfi, D.; Paolucci, M. Simulated Annealing as an Intensification Component in Hybrid Population-Based Metaheuristics. In *Simulated Annealing*; InTechOpen: Vienna, Austria, 2008.
38. Kalami, S.M. Feature Selection using Metaheuristics and EAs. Available online: www.yarpiz.com (accessed on 7 May 2018).
39. Breiman, L. Bagging predictors. *Machine Learn.* 1996, 24, 123–140. [CrossRef]
40. Sreng, S.; Maneerat, N.; Isarakorn, D.; Hamamoto, K.; Panjaphongse, R. Primary screening of diabetic retinopathy based on integrating morphological operation and support vector machine. In *Proceedings of the International Conference on Intelligent Informatics and Biomedical Sciences (ICIIBMS)*, Okinawa, Japan, 24–26 November 2017; pp. 250–254.
41. Holland, J.H. *Adaptation in Natural and Artificial Systems: An Introductory Analysis with Applications to Biology, Control, and Artificial Intelligence*;

University Michigan Press: Ann Arbor, MI, USA, 1975.

42. Kennedy, J. Particle swarm optimization. In Encyclopedia of Machine Learning; Springer: Boston, MA, USA, 2011; pp. 760–766.
43. American Diabetes Association. 10. Microvascular Complications and Foot Care: Standards of Medical Care in Diabetes-2018. Diabetes Care 2018; 41:S105.
44. O'Hare JP, Hopper A, Madhavan C, et al. Adding retinal photography to screening for diabetic retinopathy: a prospective study in primary care. BMJ 1996; 312:679.
45. A. Sopharak, B. Uyyanonvara, S. Barman, and T. Williamson, Automatic microaneurysm detection from non-dilated diabetic retinopathy retinal images. In Proceedings of the World Congress on Engineering, vol. 2, pp. 6-8. 2011.
46. R. Murugan, R. Korah, S.N. Fathima, and T. V. Haritha, Microaneurysms detection methods in retinal images using mathematical morphology. Ophthalmology, 110 (2003), 1679-80.
47. P. Yunuch, N. Maneerat, D. Isarakorn, B. Pasaya, R. Panjaphongse, and R. Varakulsiripunth. Automatic microaneurysms detection through retinal color image analysis. In Information Technology and Electrical Engineering (ICITEE), 2013 International Conference on pp. 36-40, IEEE, October 2013.
48. T. Inoue, Y. Hatanaka, S. Okumura, C. Muramatsu, and H. Fujita, Automated microaneurysm detection method based on eigenvalue analysis using hessian matrix in retinal fundus images. In Engineering in Medicine and Biology Society (EMBC), 2013 35th Annual International Conference of the IEEE, pp. 5873-5876, July 2013.
49. J. Prakash, and K. Sumathi, Detection and Classification of Microaneurysms for Diabetic Retinopathy. International Journal of Engineering Research and

Applications (IJERA) ISSN: 2248-9622 National, Conference on Advanced communication & Computing Techniques (NCACCT), March 19, 2013.

50. C. Aravind, M. Ponnibala, S. Vijayachitra, Automatic detection of microaneurysms and classification of diabetic retinopathy images using SVM technique. In IJCA Proceedings on international conference on innovations in intelligent instrumentation, optimization and electrical sciences ICIIIOES (11), pp. 18-22, Jul 12, 2013.
51. B. Dupas, T. Walter, A. Erginay et al., "Evaluation of automated fundus photograph analysis algorithms for detecting microaneurysms, haemorrhages and exudates, and of a computer-assisted diagnostic system for grading diabetic retinopathy," *Diabetes & Metabolism* 36(3), 2010, pp. 213-220.
52. S. Sreng, J. I. Takada, N. Maneerat, D. Isarakorn, R. Varakulsiripunth, B. Pasaya, and R. Panjaphongse, Feature extraction from retinal fundus image for early detection of diabetic retinopathy. In Humanitarian Technology Conference (R10-HTC), 2013 IEEE Region 10, pp. 63-66, August 2013.
53. N. Kleawsirikul, S. Gulati, and B. Uyyanonvara, "Automated Retinal Hemorrhage Detection Using Morphological Top Hat and Rule-based Classification," 3rd International Conference on Intelligent Computational Systems (ICICS 2013), pp. 39-43.
54. P. N. Sharath Kumar, R. Rajesh Kumar, A. Sathar, and V. Sahasranamam, "Automatic detection of red lesions in digital color retinal images," In Contemporary Computing and Informatics (IC3I), 2014 International Conference on pp. 1148-1153, IEEE, November 2014.
55. T. Spencer, R. P. Phillips, P. F. Sharp, and J. V. Forrester, "Automated detection and quantification of microaneurysms in fluorescein angiograms", *Graefe's archive*

- for clinical and experimental ophthalmology 230, no. 1, pp. 36-41, 1992.
56. V. M. Mane, R. B. Kawadiwale, and D. V. Jadhav, "Detection of Red lesions in diabetic retinopathy affected fundus images," In Advance Computing Conference (IACC), 2015 IEEE International, pp. 56-60, IEEE, June 2015.
 57. M. García, C. Sánchez, M. López, A. Díez, and R. Hornero, "Automatic detection of red lesions in retinal images using a multilayer perceptron neural network" In Engineering in Medicine and Biology Society, 2008. EMBS 2008. 30th Annual International Conference of the IEEE, pp. 5425-5428, IEEE, August 2008.
 58. N. Otsu, "A Threshold Selection Method from Gray-Level Histograms," IEEE Transactions on Systems, Man, and Cybernetics, Vol. 9, No. 1, pp. 62-66, 1979.
 59. Stewart, W. Michael : "Diabetic Retinopathy: Current Pharmacologic Treatment and Emerging Strategies", Springer, (2017).
 60. A. Ioannides, N.D. Georgakarakos, I. Elaroud, and P. Andreou : "Isolated cotton-wool spots of unknown etiology: management and sequential spectral domain optical coherence tomography documentation", Clinical ophthalmology (Auckland, NZ), Vol.5, pp.1431 (2011)
 61. T.Y. Chui, L.N. Thibos, A. Bradley, and S.A. Burns : "the mechanisms of vision loss associated with a cotton wool spot", Vol. 49, No.23, pp.2826-2834 (2009)
 62. D. Schmidt : "The mystery of cotton-wool spots-a review of recent and historical descriptions", European journal of medical research 13, No. 6, pp.231 (2008)
 63. M. Niemeijer, B. van Ginneken, S.R. Russell, M.S. Suttorp-Schulten, and M.D. Abramoff : "Automated detection and differentiation of drusen, exudates, and cotton-wool spots in digital color fundus photographs for diabetic retinopathy diagnosis", Investigative ophthalmology & visual science, Vol. 48, No.5, pp.2260-

- 2267 (2007).
64. C.I. Sánchez, M. Niemeijer, T. Kockelkorn, M.D. Abràmoff, and B. van Ginneken: “Active learning approach for detection of hard exudates, cotton wool spots, and drusen in retinal images”, In *Medical Imaging: Computer-Aided Diagnosis*, SPIE, Vol. 7260, pp. 72601I (2009).
 65. Y.M. Rajput, R.R Manza, and M.B. Patwari: “Extraction of Cotton Wool Spot using Multi Resolution Analysis and Classification using K-Means Clustering”, In *IJCA Proceedings on National conference on Digital Image and Signal Processing, International Journal of Computer Applications*, pp.0975–8887 (2015)
 66. T. Bui, N. Maneerat, and U. Watchareeruetai : “Detection of cotton wool for diabetic retinopathy analysis using neural network”, In *Computational Intelligence and Applications (IWCIA), 2017 IEEE 10th International Workshop on*, pp. 203-206 (2017)
 67. S. Irshad, M. Salman, M.U. Akram, and U. Yasin : “Automated detection of Cotton Wool Spots for the diagnosis of Hypertensive Retinopathy” In *Biomedical Engineering Conference (CIBEC), Cairo International, IEEE*, pp. 121-124 (2014).
 68. A. Ashraf, M.U. Akram, and S.A. Sheikh : “Detection of retinal whitening, cotton wool spots and retinal Hemorrhages for diagnosis of Malarial Retinopathy”, In *TENCON 2015-2015 IEEE Region 10 Conference*, pp. 1-5 (2015)
 69. A. Usman, S.A. Khitran, M.U. Akram, and Y. Nadeem : “A robust algorithm for optic disc segmentation from colored fundus images”, In *International Conference Image Analysis and Recognition*, October 2014, pp. 303-310, Springer, Cham (2014)
 70. S. Roychowdhury, D.D. Koozekanani and K.K. Parhi: *DREAM: Diabetic*

- Retinopathy Analysis Using Machine Learning, IEEE Journal of Biomedical and Health Informatics, Vol. 18, No. 5, pp. 1717-1728 (2014)
71. C.J. ME and C.J. ME: Automatic detection and classification of diabetic retinopathy lesion using bag of visual words model, International Journal of Scientific and Research Publications (2015)
 72. M. Hire, S. Shinde: Ant Colony Optimization Based Exudates Segmentation of Fundus Images, Journal of VLSI Design and Signal Processing, Vol 3, No 2,3 (2017).
 73. B. Harangi and A. Hajdu: Automatic exudate detection by fusing multiple active contours and regionwise classification, Computers in biology and medicine, Vol. 54, pp.156-171 (2014).
 74. H.A. Nugroho, K.W. Oktoeberza, T.B. Adji, and F. Najamuddin: Detection of Exudates on Color Fundus Images using Texture Based Feature Extraction, International Journal of Technology, Vol.6, No.2, pp.121-129 (2015).
 75. T. Mapayi, S. Viriri, and J.R. Tapamo : “A new adaptive thresholding technique for retinal vessel segmentation based on local homogeneity information”, In International Conference on Image and Signal Processing, pp. 558-567, Springer, Cham (2014)
 76. X. Jiang, and D. Mojon : “Adaptive local thresholding by verification-based multithreshold probing with application to vessel detection in retinal images”, IEEE Transactions on Pattern Analysis and Machine Intelligence, Vol.25, No.1, pp.131-137 (2003)
 77. Q. Li, J. You, L. Zhang and P. Bhattacharya: “Automated retinal vessel segmentation using multiscale analysis and adaptive thresholding”, In Image

- Analysis and Interpretation, 2006 IEEE Southwest Symposium on, pp. 139-143 (2006).
78. T. Mapayi, S. Viriri, and J.R. Tapamo : “Adaptive thresholding technique for retinal vessel segmentation based on GLCM-energy information”, Computational and mathematical methods in medicine (2015)
 79. F. Ghadiri, R. Bergevin, and M. Shafiee : “An adaptive thresholding approach for automatic optic disk segmentation”, arXiv preprint arXiv:1710.05104, (2017)
 80. S. Ganguly, K. Srivastava, M.K. Dutta, M. Parthasarathi, R. Burget, and K. Riha : “An adaptive threshold based algorithm for detection of red lesions of diabetic retinopathy in a fundus image”, In Medical Imaging, m-Health and Emerging Communication Systems (MedCom), 2014 International Conference on pp. 91-94, IEEE (2014)
 81. M. Dorigo, V. Maniezzo, and A. Coloni : “Ant system: optimization by a colony of cooperating agents”, IEEE Transactions on Systems, Man, and Cybernetics, Part B (Cybernetics), Vol. 26, No. 1, pp.29-41,1996.
 82. C.Y. Chang, M.S. Chang, and S.J. Chen : “Application of communication ant colony optimization for lymph node classification”, In Systems, Man, and Cybernetics (SMC), 2012 IEEE International Conference on IEEE, pp. 1954-1959 (2012)
 83. E. Fiorina, R. Bellotti, P. Cerello, A. Chincarini, I. De Mitri, and M.E. Fantacci : “Fully automated hippocampus segmentation with virtual ant colonies” In Computer-Based Medical Systems (CBMS), 2012 25th International Symposium on IEEE, pp. 1-6, (2012)
 84. R.C. Gopalakrishnan, and V. Kuppusamy : “Ant colony optimization approaches

- to clustering of lung nodules from CT images”, Computational and mathematical methods in medicine (2014)
85. S. Hooshyar, and R. Khayati : “Retina vessel detection using fuzzy ant colony algorithm”, In Computer and Robot Vision (CRV), 2010 Canadian Conference on IEEE, pp. 239-244 (2010)
86. C. Pereira, L. Gonçalves, and M. Ferreira : “Exudate segmentation in fundus images using an ant colony optimization approach”, Information Sciences, 296, pp.14-24 (2015)
87. T. Kauppi, J.K Kämäräinen, L. Lensu, V. Kalesnykiene, L. Sorri, H. Uusitalo, and H. Kälviäinen : “Constructing benchmark databases and protocols for medical image analysis: Diabetic retinopathy”, Computational and mathematical methods in medicine (2013).
88. P.H. Scanlon, S. Aldington, C. Wilkinson, and D. Matthews : “ A Practical Manual of Diabetic Retinopathy Management”, John Wiley & Sons (2009).
89. T. Kauppi, V. Kalesnykiene, J.K. Kamarainen, L. Lensu, I. Sorri, A. Raninen, R. Voutilainen, H. Uusitalo, H. Kälviäinen, and J. Pietilä : “The DIARETDB1 Diabetic Retinopathy Database and Evaluation Protocol” (2007)
90. A. Budai, R. Bock, A. Maier, J. Hornegger, and G. Michelson : “Robust vessel segmentation in fundus images”, International journal of biomedical imaging (2013)
91. D. Rajashekar, G. Srinivasa, and A. Vinekar : “Comprehensive Retinal Image Analysis for Aggressive Posterior Retinopathy of Prematurity”, PloS one, Vol. 11, No.10, e0163923 (2016)
92. H. Li, K.R. Liu, and S.C. Lo : “Fractal modeling and segmentation for the

- enhancement of microcalcifications in digital mammograms”, IEEE transactions on medical imaging Vol.16, No.6,pp.785-798 (1997)
93. F. Akram, M.A. Garcia, and D. Puig : “Active contours driven by local and global fitted image models for image segmentation robust to intensity inhomogeneity”, PloS one, Vol.12, No.4, e0174813 (2017)
94. D. Bradley, and G. Roth, “Adaptive thresholding using the integral image”, Journal of Graphics Tools Vol.12, No.2, pp.13-21 (2007)
95. <https://www.mathworks.com/>
96. R. Kumar, R. Srivastava, and S. Srivastava : “Detection and classification of cancer from microscopic biopsy images using clinically significant and biologically interpretable features”, Journal of medical engineering (2015)
97. R.M. Haralick: Statistical and structural approaches to texture, Proc. IEEE, vol. 67, no. 5, pp. 786-804, 1979.
98. D.A. Clausi: “An analysis of co-occurrence texture statistics as a function of grey level quantization”, Can. J. Remote Sensing, vol. 28, no.1, pp. 45-62, (2002).
99. M.M. Galloway, “Texture analysis using grey level run lengths”, NASA STI/Recon Technical Report N, 75 (1974).
- 100.V. Van Belle, B. Van Calster, S. Van Huffel, J.A. Suykens, and P. Lisboa : “Explaining Support Vector Machines: A Color Based Nomogram”, PloS one, Vol.11, No.10, e0164568 (2016)
- 101.C. Cortes and V. Vapnik : “Support-vector networks”, Machine learning, Vol.20, No.3, pp273-297 (1995)
- 102.W. Zhu, N. Zeng, and N. Wang : “Sensitivity, specificity, accuracy, associated confidence interval and ROC analysis with practical SAS implementations”,

NESUG proceedings: health care and life science, pp.67 (2010).

103. Badar, M., Shahzad, M. and Fraz, M.M., 2018, July. Simultaneous segmentation of multiple retinal pathologies using fully convolutional deep neural network. In *Annual Conference on Medical Image Understanding and Analysis* (pp. 313-324). Springer, Cham.
104. Razzak, M.I., Naz, S. and Zaib, A., 2018. Deep Learning for Medical Image Processing: Overview, Challenges and the Future. In *Classification in BioApps* (pp. 323-350). Springer, Cham.
105. LeCun, Y., Bengio, Y. and Hinton, G., 2015. Deep learning. *nature*, 521(7553), p.436.
106. Mahdianpari, M., Salehi, B., Rezaee, M., Mohammadimanesh, F. and Zhang, Y., 2018. Very deep convolutional neural networks for complex land cover mapping using multispectral remote sensing imagery. *Remote Sensing*, 10(7), p.1119.
107. Esteva, A., Kuprel, B., Novoa, R.A., Ko, J., Swetter, S.M., Blau, H.M. and Thrun, S., 2017. Dermatologist-level classification of skin cancer with deep neural networks. *Nature*, 542(7639), p.115.
108. Kainz, P., Pfeiffer, M. and Urschler, M., 2015. Semantic segmentation of colon glands with deep convolutional neural networks and total variation segmentation. *arXiv preprint arXiv:1511.06919*.
109. Zaharchuk, G., Gong, E., Wintermark, M., Rubin, D. and Langlotz, C.P., 2018. Deep learning in neuroradiology. *American Journal of Neuroradiology*, 39(10), pp.1776-1784.

110. Choi, J.Y., Yoo, T.K., Seo, J.G., Kwak, J., Um, T.T. and Rim, T.H., 2017. Multi-categorical deep learning neural network to classify retinal images: A pilot study employing small database. *PloS one*, 12(11), p.e0187336.
111. Xu, K., Feng, D. and Mi, H., 2017. Deep Convolutional Neural Network-Based Early Automated Detection of Diabetic Retinopathy Using Fundus Image. *Molecules*, 22(12), p.2054.
112. Lahiri, A., Roy, A.G., Sheet, D. and Biswas, P.K., 2016, August. Deep neural ensemble for retinal vessel segmentation in fundus images towards achieving label-free angiography. In *Engineering in Medicine and Biology Society (EMBC), 2016 IEEE 38th Annual International Conference of the* (pp. 1340-1343). IEEE.
113. Chai, Y., Liu, H. and Xu, J., 2018. Glaucoma diagnosis based on both hidden features and domain knowledge through deep learning models. *Knowledge-Based Systems*, 161, pp.147-156.
114. Fukushima, K., 1988. Neocognitron: A hierarchical neural network capable of visual pattern recognition. *Neural networks*, 1(2), pp.119-130.
115. LeCun, Y., Bottou, L., Bengio, Y. and Haffner, P., 1998. Gradient-based learning applied to document recognition. *Proceedings of the IEEE*, 86(11), pp.2278-2324.
116. Krizhevsky, A., Sutskever, I. and Hinton, G.E., 2012. Imagenet classification with deep convolutional neural networks. In *Advances in neural information processing systems* (pp. 1097-1105).
117. He, K., Zhang, X., Ren, S. and Sun, J., 2016. Deep residual learning for image recognition. In *Proceedings of the IEEE conference on computer vision and pattern recognition* (pp. 770-778).

APPENDIX A

FEATURE EXTRACTION

After image segmentation, the binary image is reconstructed into a grayscale image using morphological reconstruction, and then the pathological signs of DR can be differentiated based on the pixel density in binary image and the information of texture, color, and intensity of the detected regions. Eight feature extractors namely morphological features, intensity features, color features, first order statistical features, Gray Level Co-occurrence Matrix (GLCM) features, Gray Level Run Length Matrix (GLRLM) features, local binary pattern features and Tamura's texture features are extracted. The basic concepts of each feature extractors are detailed in the following sub-section: 1.1 Morphological features, 1.2 Intensity features, 1.3 Color features, 1.4 First order statistical features, 1.5 Gray Level Co-occurrence Matrix (GLCM) features, 1.6 Gray Level Run Length Matrix (GLRLM) features, 1.7 Local binary pattern features and 1.8 Tamura's texture features.

1.1 Morphological Features

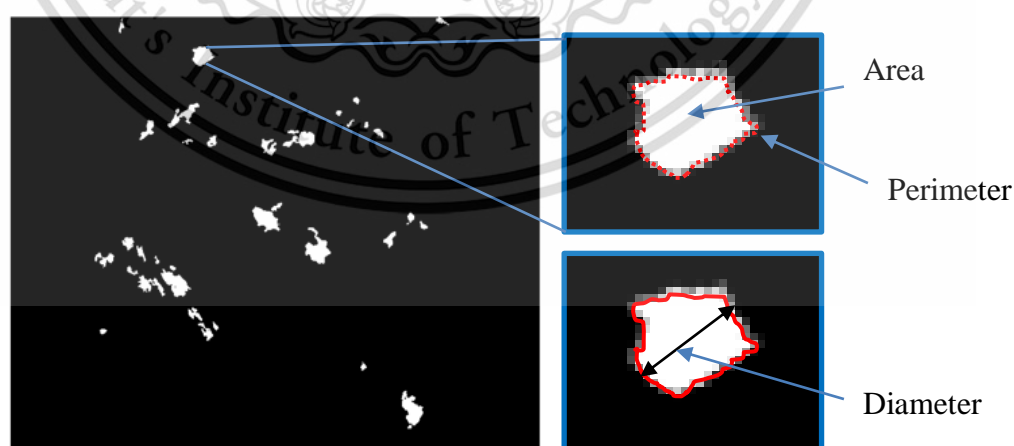


Figure 1. Morphological features for DR pathological signs

Morphological features are used to differentiate the binary objects based on the size and shape irregularity. In this thesis, 8 different morphological features are extracted based on the area, perimeter and diameter of the objects (see Figure 1).

- 1 Area: Total pixels inside the object borders.
- 2 Perimeter: Total pixels of the length of object outline.
- 3 Diameter: Total pixels of the length of the longest line passing through the object centroid that connects two points at the boundaries.
- 4 Roundness: Measure the circularity of the object as defined in equation below

$$\frac{4\pi * Area}{Perimeter^2} \quad (1)$$

- 5 Eccentricity: The ratio of the distance between the foci of the ellipse and its major axis length.

$$2 * \left(\sqrt{\left(\frac{ma}{2}\right)^2 - \left(\frac{mi}{2}\right)^2} \right) / ma \quad (2)$$

- 6 Sodality: The ratio of object area to convex hull area

$$\frac{Area}{ConvexArea} \quad (3)$$

- 7 Extent: Ratio between the area and perimeter

$$\frac{Area}{Perimeter} \quad (4)$$

- 8 Compactness

$$\frac{Perimeter^2}{4\pi * Area} \quad (5)$$

1.2 Intensity Features

Intensity features are used to measure the gray level intensity of the detection object. They are including maximum intensity value, mean intensity value and minimum intensity values and can be denoted as following:

- MaxIntensity: The greatest intensity value in the detected object.

$$\text{MaxIntensity} = \max(\text{IntensityValue})$$

- MeanIntensity: The mean of all intensity value in the detected object.

$$\text{MeanIntensity} = \text{mean}(\text{IntensityValue})$$

- MinIntensity: The lowest intensity value in the detected object.

$$\text{MinIntensity} = \min(\text{IntensityValue})$$

1.3 Color Features

Beside the area and shape of the detected object, the pathological signs of DR vary in Color. The color features use in this thesis are extracted from the mean of three difference color spaces; RGB, HSV and Lab.

- RGB color space

$$\text{MeanIntensity of Red channel} = \text{mean}(\text{Red})$$

$$\text{MeanIntensity of Green channel} = \text{mean}(\text{Green})$$

$$\text{MeanIntensity of Blue channel} = \text{mean}(\text{Blue})$$

- HSV color space

$$\text{MeanIntensity of Hue} = \text{mean}(\text{Hue})$$

$$\text{MeanIntensity of Saturation} = \text{mean}(\text{Saturation})$$

$$\text{MeanIntensity of Value} = \text{mean}(\text{Value})$$

- Lab color space

MeanIntensity of L value = mean(L)

MeanIntensity of a value = mean(a)

MeanIntensity of b value = mean(b)

1.4 First order statistical Features

First Order Statistical features (FOS) describe the information of the frequency of appearance of each gray level histogram in an image. Suppose i is 1D gray level histogram of the detected object so $i = [0, 1 \dots t - 1, t, t + 1 \dots 255]$, and the probability of the pixel being i can be defined as:

$$P[i] = \frac{f_i}{N} \quad (6)$$

where f_i is the number of pixels that have gray level i and N is the total number of pixels in the detected object.

- Mean intensity is the average level of intensity of the detected object:

$$m = \sum_{i=0}^{255} iP[i] \quad (7)$$

- Variance describes the variation of intensity around the mean

$$Var = \sum_{i=0}^{255} (i - m)^2 \cdot P[i] \quad (8)$$

- Standard deviation is the square root of the variance

$$std = \sqrt{\sum_{i=0}^{255} (i - m)^2 \cdot P[i]} \quad (9)$$

- Skewness describes the asymmetry of the data (intensity of a darker or lighter color) around the mean

$$Sk = \sigma^{-3} \sum_{i=0}^{255} (i - m)^3 P[i] \quad (10)$$

- Kurtosis measures the uniformity information of the intensity distribution,

$$Ku = \sigma^{-4} \sum_{i=0}^{L-1} (i - \mu)^4 P[i] - 3 \quad (11)$$

- Smoothness defines the image surface smoothness,

$$S = 1 - \left(\frac{1}{1 + std^2} \right) \quad (12)$$

- Energy describes how much variation on the brightness level

$$\sum_{i=0}^{255} P[i]^2 \quad (13)$$

1.5 Gray Level Co-occurrence Matrix (GLCM)

FOS features provide the information about the appearance of each gray level distribution of the detected object. However, these features ignore the spatial distribution of the various gray levels inside the object. In this sub-section, GLCM is provided to describe more information about the relationship amount the same pair of pixel with its orientation φ (0^0 , 45^0 , 90^0 , 135^0).

Suppose we have an image (see Figure 2(a)) with the gray levels $f = 0, 1, 2, 3$, the gray tones at a distance d (inter-pixel distance) is defined in Figure 2(b). For example, we want to find the pixel pair (2,3). The pair (2,3) appear on the horizontal direction (0^0) 1 time, on the diagonal (45^0) 1 time, on the vertical (90^0) 2 times, and on

anti-diagonal (135°) 2 times. The results for the given example can be found in Figure 2(c).

| | | | |
|---|---|---|---|
| 0 | 0 | 1 | 1 |
| 0 | 0 | 1 | 1 |
| 0 | 2 | 2 | 2 |
| 2 | 2 | 3 | 3 |

(a)

| Gray tones | | | | | |
|------------|---|-------|-------|-------|-------|
| Gray tones | | 0 | 1 | 2 | 3 |
| | 0 | (0,0) | (0,1) | (0,2) | (0,3) |
| | 1 | (1,0) | (1,1) | (1,2) | (1,3) |
| | 2 | (2,0) | (2,1) | (2,2) | (2,3) |
| | 3 | (3,0) | (3,1) | (3,2) | (3,3) |

(b)

| Co-occurrence (0°) | | | | Co-occurrence (45°) | | | | Co-occurrence (90°) | | | | Co-occurrence (135°) | | | |
|-----------------------------|---|---|---|------------------------------|---|---|---|------------------------------|---|---|---|-------------------------------|---|---|---|
| 4 | 2 | 1 | 0 | 4 | 1 | 0 | 0 | 6 | 0 | 2 | 0 | 2 | 1 | 3 | 0 |
| 2 | 4 | 0 | 0 | 1 | 2 | 2 | 0 | 0 | 4 | 2 | 0 | 1 | 2 | 1 | 0 |
| 1 | 0 | 6 | 1 | 0 | 2 | 4 | 1 | 2 | 2 | 2 | 2 | 3 | 1 | 0 | 2 |
| 0 | 0 | 1 | 2 | 0 | 0 | 1 | 0 | 0 | 0 | 2 | 0 | 0 | 0 | 2 | 0 |

(c)

Figure 2. Example of co-occurrence matrix calculation

Suppose I is an image with size $N_x \times N_y$ and gray level M . The GLCM which can be denoted as $P(i, j)$ is the frequency of the pixel intensity value i co-occurs with the pixel intensity value j and the 22 GLCM features [91] can be extracted as follow:

$$Autocorrelation = \sum_i^M \sum_j^M (ij)P(i, j) \quad (14)$$

$$Contrast = \sum_i^M \sum_j^M (i - j)^2 P(i, j) \quad (15)$$

$$Correlation1 = \sum_i^M \sum_j^M \frac{(i - \mu_x)(j - \mu_y)P(i, j)}{\sigma_x \sigma_y} \quad (16)$$

$$\text{Correlation2} = \sum_i^M \sum_j^M \frac{(ij)P(i,j) - \mu_x \mu_y}{\sigma_x \sigma_y} \quad (17)$$

$$\text{Cluster Prominence} = \sum_i^M \sum_j^M (i - \mu_x + j - \mu_y)^4 P(i,j) \quad (18)$$

$$\text{Cluster Shade} = \sum_i^M \sum_j^M (i - \mu_x + j - \mu_y)^3 P(i,j) \quad (19)$$

$$\text{Dissimilarity} = \sum_i^M \sum_j^M |i - j| P(i,j) \quad (20)$$

$$\text{Energy} = \sum_i^M \sum_j^M P(i,j)^2 \quad (21)$$

$$\text{Entropy} = - \sum_i^M \sum_j^M P(i,j) \ln(P(i,j)) \quad (22)$$

$$\text{Homogeneity1} = \sum_i^M \sum_j^M \frac{P(i,j)}{1 + |i - j|} \quad (23)$$

$$\text{Homogeneity2} = \sum_i^M \sum_j^M \frac{P(i,j)}{1 + (i - j)^2} \quad (24)$$

$$\text{Maximum Probability} = \max_{i,j} P(i,j) \quad (25)$$

$$\text{Sum of Squares} = \sum_i^M \sum_j^M (i - \mu)^2 P(i,j) \quad (26)$$

$$\text{Sum Variance} = \sum_{k=2}^{2M} \left(k - \sum_{k=2}^{2M} k \cdot P_{x+y}(k) \right)^2 P_{x+y}(k) \quad (27)$$

$$\text{Sum Entropy} = - \sum_{k=2}^{2M} P_{x+y}(k) \ln(P_{x+y}(k)) \quad (28)$$

$$\text{Difference Variance} = \sum_{k=0}^{M-1} \left(k - \sum_{l=0}^{M-1} l \cdot P_{x-y}(l) \right)^2 P_{x-y}(k) \quad (29)$$

$$\text{Difference Entropy} = - \sum_{k=0}^{M-1} P_{x-y}(k) \ln(P_{x-y}(k)) \quad (30)$$

$$\text{Information Measure of Correlation1} = \frac{HXY - HXY1}{\max(HX, HY)} \quad (31)$$

$$\text{Information Measure of Correlation2} = \sqrt{1 - \exp(-2(HXY2 - HXY))} \quad (32)$$

where HXY, HX, HY are the entropy of $P(i, j)$, $P(i)$, and $P(j)$ respectively.

$$\text{Inverse Difference Normalized} = \sum_{i=1}^M \sum_{j=1}^M \frac{P(i, j)}{1 + \frac{|i-j|^2}{M}} \quad (33)$$

$$\text{Inverse Difference Moment Normalized} = \sum_{i=1}^M \sum_{j=1}^M \frac{P(i, j)}{1 + \frac{(i-j)^2}{M}} \quad (34)$$

1.6 Gray Level Run Length Matrix (GLRLM)

GLRLM describes the frequency of appearance of a set of consecutive pixels having the same gray value with its orientation ϕ (0° , 45° , 90° , 135°). As an example of the image (Figure 2(a)) the run length matrix for the horizontal direction $\phi = 0^\circ$ can be defined as in Figure 3(a).

| Run Length | | | |
|------------|---|---|---|
| Gray level | | 2 | 3 |
| | 0 | 2 | 0 |
| | 1 | 2 | 0 |
| | 2 | 1 | 1 |
| | 3 | 1 | 0 |

(a)

| Co-occurrence (0°) | | Co-occurrence (45°) | | Co-occurrence (90°) | | Co-occurrence (135°) | |
|--------------------|---|---------------------|---|---------------------|---|----------------------|---|
| 2 | 0 | 2 | 0 | 1 | 1 | 1 | 0 |
| 2 | 0 | 1 | 0 | 2 | 0 | 1 | 0 |
| 1 | 1 | 2 | 0 | 1 | 0 | 0 | 0 |
| 1 | 0 | 0 | 0 | 0 | 0 | 0 | 0 |

(b)

Figure 3. Example of run length matrix calculation

The following features can be calculated using the GLRLM [92]:

$$\text{Short Run Emphasis (SRE)} = \frac{1}{n^r} \sum_{i=1}^G \sum_{j=1}^R \frac{P(i, j)}{j^2} \quad (35)$$

$$\text{Long Run Emphasis (LRE)} = \frac{1}{n^r} \sum_{i=1}^G \sum_{j=1}^R P(i, j) j^2 \quad (36)$$

$$\text{Low Gray level Run Emphasis (LGRE)} = \frac{1}{n^r} \sum_{i=1}^G \sum_{j=1}^R \frac{P(i, j)}{i^2} \quad (37)$$

$$\text{High Gray level Run Emphasis (HGRE)} = \frac{1}{n^r} \sum_{i=1}^G \sum_{j=1}^R P(i, j) i^2 \quad (38)$$

(a)

$$\text{Short Run Low Gray level Emphasis (SRLGE)} = \frac{1}{n^r} \sum_{i=1}^G \sum_{j=1}^R \frac{P(i,j)}{i^2 j^2} \quad (39)$$

$$\text{Short Run High Gray level Emphasis (SRHGE)} = \frac{1}{n^r} \sum_{i=1}^G \sum_{j=1}^R \frac{P(i,j) i^2}{j^2} \quad (40)$$

$$\text{Long Run Low Gray level Emphasis (LRLGE)} = \frac{1}{n^r} \sum_{i=1}^G \sum_{j=1}^R \frac{P(i,j) j^2}{i^2} \quad (41)$$

$$\text{Long Run High Gray level Emphasis (LRHGE)} = \frac{1}{n^r} \sum_{i=1}^G \sum_{j=1}^R P(i,j) i^2 j^2 \quad (42)$$

$$\text{Gray level Non Uniformity (GNU)} = \frac{1}{n^r} \sum_{i=1}^G \left[\sum_{j=1}^R P(i,j) \right]^2 \quad (43)$$

$$\text{Run length Non Uniformity (RNU)} = \frac{1}{n^r} \sum_{j=1}^{MG} \left[\sum_{i=1}^R P(i,j) \right]^2 \quad (44)$$

$$\text{Run Percentage (RP)} = \frac{n_r}{n_p} \quad (45)$$

where $P(i,j)$ is the gray level run length matrix, $(i,j)^{th}$ is the number of runs with gray level i and length j occur in the image along angle ϕ . R is the number of different run lengths in the image, n_r is the total number of runs, and n_p is the number of pixels in the image.

1.7 Tamura's texture Features

Tamura features are based on human visual perception and have huge potential in image representation. These are six different texture features given by Tamura [94]: Coarseness, Contrast, Directionality, Line-Likeness, Regularity and Roughness. In this

thesis, Coarseness and Contrast are extracted and used to differentiate DR and Non_DR.

Coarseness basically relates to the distance in gray levels of spatial variations, which is implicitly related to the size of primitive elements forming the texture.

$$A_k(x, y) = \sum_{i=x-2^{k-1}}^{x+2^{k-1}} \sum_{j=y-2^{k-1}}^{y+2^{k-1}} \frac{P(i, j)}{2^{2k}} \quad (46)$$

where, $2^k * 2^k$ size is the average of neighborhood.

$$E_{k,h}(x, y) = |A_k(x + 2^{k-1}, y) - A_k(x - 2^{k-1}, y)| \quad (47)$$

where $E_{k,h}(x, y)$ is the difference between pair of averages corresponding to non-overlapping neighborhoods.

Contrast measures distribution of gray levels that varies in an image and to what extent its distribution is biased to black or white. The second order and normalized fourth-order central moments of the gray levels are used to define the contrast.

$$Contrast = \frac{\sigma}{\alpha_4} \quad (48)$$

$$\alpha_4 = \frac{\mu_4}{\sigma^4} \quad (49)$$

where μ_4 is the fourth moment about the mean and σ^2 is the variance.

APPENDIX B

SUPPORT VECTOR MACHINE

1. Linear support vector machine

Suppose $D = \{(\vec{x}_i, y_i), i = 1 \dots N\}$ is a vector of length n and $y_i \in \{-1, +1\}$

for 2 classes of data 1 or -1. If these data are linearly separable, we can determine the decision function:

$$D(x) = W^T X + b \quad (1)$$

where w is an N -dimensional vector, b is a bias term, and for $i = 1, \dots, N$

$$W^T X_i + b \begin{cases} > 0 \text{ for } y_i = 1, \\ < 0 \text{ for } y_i = -1 \end{cases} \quad (2)$$

Because the training data are linearly separable, no training data satisfy

$$W^T X + b = 0.$$

Thus, the equation (1) can be written as:

$$W^T X_i + b \begin{cases} \geq 1 \text{ for } y_i = 1, \\ \leq -1 \text{ for } y_i = -1 \end{cases} \quad (3)$$

And it is equivalent to

$$y_i (W^T X_i + b) \geq 1 \quad \forall i \quad (4)$$

As illustrated in Fig.1, there are many possible lines (hyperplanes) to separate the training data. But which one is the best?

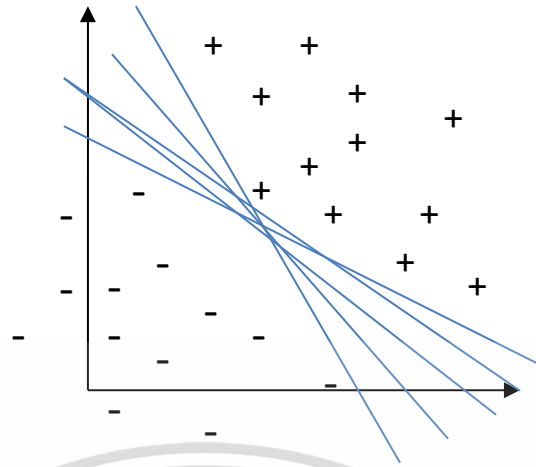


Figure 1. Linearly separable lines

Based on SVM classifier the best line is the hyperplane that maximize the margin. This means that we need to increase the gap (margin) between the 2 classes as much as possible. The best line is the hyperplane in the middle of the gap as shown in Figure 2.

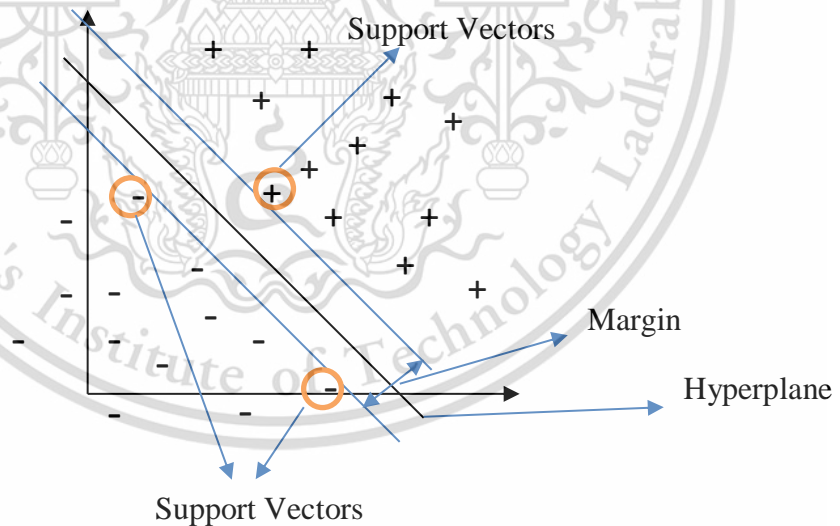


Figure 2. SVM parameters

At the support vectors, equation (2) can be defined as:

$$W^T x^+ + b = 1 \text{ for } y_i = 1 \quad (5)$$

$$W^T x^- + b = -1 \text{ for } y_i = -1 \quad (6)$$

Subtracting equation (5) from equation (4):

$$W^T(x^+ - x^-) = 2 \quad (7)$$

The margin

$$M = \frac{D(x^+)}{\|W\|} - \frac{D(x^-)}{\|W\|} = \frac{W^T(x^+ - x^-)}{\|W\|} \quad (8)$$

Replacing equation (6) in (7):

$$M = \frac{2}{\|W\|} \quad (9)$$

By maximizing margin M is equivalent to minimizing $\|W\|$ (the constant 2 above can be ignored).

Based on equation (3) and (8), the SVM classifier is formulated as follows:

$$\begin{aligned} \text{Find } W \text{ and } b \text{ that minimize: } & \frac{1}{2} \|W\|^2 \\ \text{Subject to constraints: } & y_i(W^T X_i + b) \geq 1 \quad \forall i \end{aligned} \quad (10)$$

2. Linearly non-separable case

In the real application, the training data set is usually linearly non-separable as illustrated in Figure 3. To deal with this case, slack variables ξ_i are introduced where $i = 1, 2, \dots, N$. The equation (10) can be rewritten as:

$$\begin{aligned} \text{Find } W \text{ and } b \text{ that minimize: } & \frac{1}{2} \|W\|^2 + C \sum_i \xi_i^2 \\ \text{Subject to constraints: } & y_i(W^T X_i + b) \geq 1 - \xi_i, \quad \xi_i \geq 0, \forall i \end{aligned} \quad (11)$$

where $C > 0$ is an appropriately selected parameter. The additional term $C \sum_i \xi_i^2$ enforces all slack variable to be as close to zero as possible.

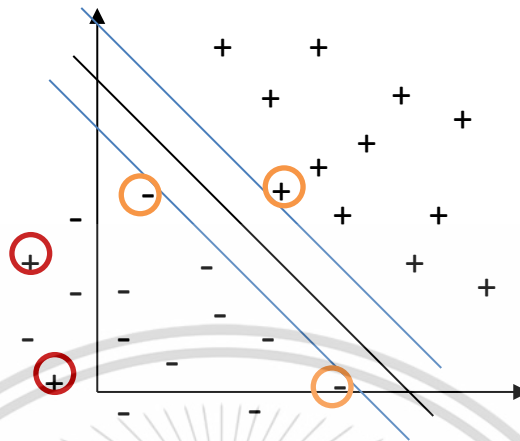


Figure 2. Linearly non-separable case

3. Nonlinear case

In case the training data are not linearly separable, the obtained classifier may not have high generalization ability although the hyperplanes are determined optimally. Thus, the original input space is mapped into a high-dimensional dot-product space called the feature space, in which data can be linearly separable as shown in Figure 4 and the decision function can be defined as equation (10).

$$D(x) = W^T \Phi(x) + b \quad (12)$$

where $\Phi: X \rightarrow F$ is a mapping from the original input space to another feature space F .

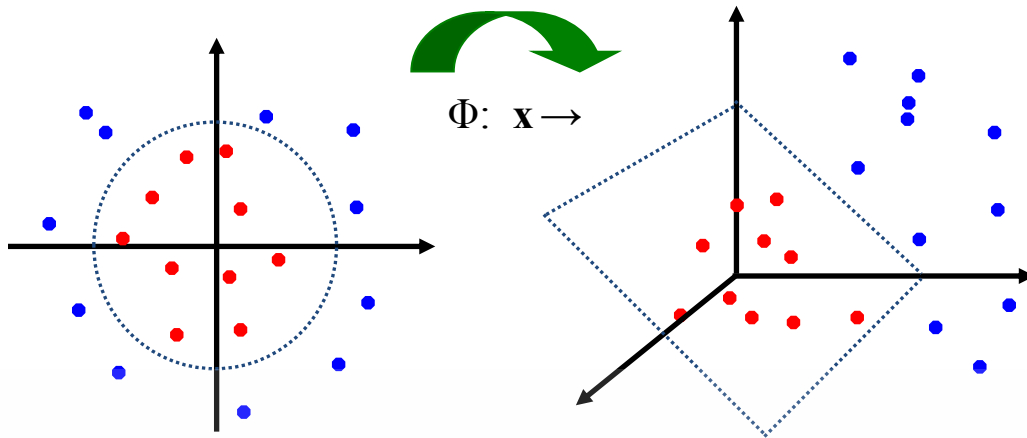


Figure 4. A transfer mapping from the original input space to another feature space.

There are 2 steps: first, a non-linear mapping transforms the data into a feature space then a linear classifier classifies the data in that feature space using kernel function.

$$\Phi(x)^T \Phi(y) = K(x, y) \quad (13)$$

where K is a corresponding kernel function

The typical kernel functions are:

- Linear Kernels: $K(x, y) = x^T y$
- Polynomial Kernels: $K(x, y) = (x^T y + 1)^d$,
Quadratic kernel for $d=2$, Cubic kernel for $d=3$
- Gaussian Kernel: $K(x, y) = e^{-\frac{\|x-y\|^2}{A}}$, A is a constant

PRESENTATIONS AND PUBLICATIONS

Conference Papers

1. S. Sreng, N. Maneerat, D. Isarakorn K. Hamamoto, and R. Panjaphongse, “Automatic hemorrhages detection based on fundus images,” In Information Technology and Electrical Engineering (ICITEE 2015), 7th International Conference on pp. 253-257, IEEE, October, 2015.
2. S. Sreng, N. Maneerat, and K. Hamamoto, “Automated microaneurysms detection in fundus images using image segmentation” In Digital Arts, Media and Technology (ICDAMT), International Conference on pp. 19-23, IEEE, March, 2017.
3. S. Sreng, N. Maneerat, D. Isarakorn K. Hamamoto, and R. Panjaphongse, “Primary screening of diabetic retinopathy based on integrating morphological operation and support vector machine,” In 2017 International Conference on Intelligent Informatics and Biomedical Sciences (ICIIBMS) , pp. 250-254, IEEE, November, 2017.
4. S. Sreng, N. Maneerat, D. Isarakorn, K. Hamamoto, and R. Panjaphongse, K.Y. Win, “Classification of Cotton Wool Spots Using Principal Components Analysis and Support Vector Machine,” BMEiCON 2018, Nov 21-24, Chaing Mai, Thailand.
5. K.Y. Win, N. Maneerat, S. Choomchuay, K. Hamamoto, and R. Panjaphongse, **S. Sreng**, “Suitable Supervised Machine Learning Techniques For Malignant Mesothelioma Diagnosis”, BMEiCON 2018, Nov 21-24, Chaing Mai, Thailand.

Journal Papers

1. S. Sreng, N. Maneerat, and K. Hamamoto, “Automatic Diabetic Retinopathy Screening Based on Morphological Operation and Support Vector Machine Integration,” Applied Science and Computer Science Publications, (ASCSP), Vol.3, Issue 3, pp. 85-90, December 2017.
2. S. Sreng, N. Maneerat, K. Hamamoto, and R. Panjaphongse, “Automated Diabetic Retinopathy Screening System Using Hybrid Simulated Annealing and Ensemble Bagging Classifier,” Advanced, Intelligent Systems, Appl. Sc., Vol. 8, No. 7, pp. 1198, July, 2018. <https://doi.org/10.3390/app8071198>
3. S. Sreng, N. Maneerat, K. Hamamoto, and R. Panjaphongse, “Cotton Wool Spots Detection in Diabetic Retinopathy Based on Adaptive Thresholding and Ant Colony Optimization Coupling Support Vector Machine”, IEEJ Trans. TEEE C, Vol. 14, No. 6, 2019.

AUTHOR BIOGRAPHY

Personal Information

Author: Mr. Syna Sreng
Degree: Doctor of Engineering
Date: 18th February 2019
Date of Birth: 10th March 1988
Place of Birth: Prey Veng, Cambodia

Education

Doctor of Engineering in Electrical Engineering,
King Mongkut's Institute of Technology Ladkrabang, Thailand, 2019

Master of Engineering in Computer Engineering,
King Mongkut's Institute of Technology Ladkrabang, Thailand, 2013

Bachelor degree in Electronics, Automation and Telecommunication,
Institute of Technology of Cambodia, Phnom Penh, Cambodia, 2011

Research Interests

My current research interests are computer vision, medical image processing and machine learning.